Characterisation of rag properties and their transport in wastewater pumps

Calibration of a discrete element rag model to simulate clogging effects

Jensen, Anna Lyhne

DOI (link to publication from Publisher):
10.5278/vbn.phd.eng.00049

Publication date:
2018

Document Version
Publisher's PDF, also known as Version of record

Citation for published version (APA):
Jensen, A. L. (2018). *Characterisation of rag properties and their transport in wastewater pumps: Calibration of a discrete element rag model to simulate clogging effects*. Aalborg Universitetsforlag. https://doi.org/10.5278/vbn.phd.eng.00049

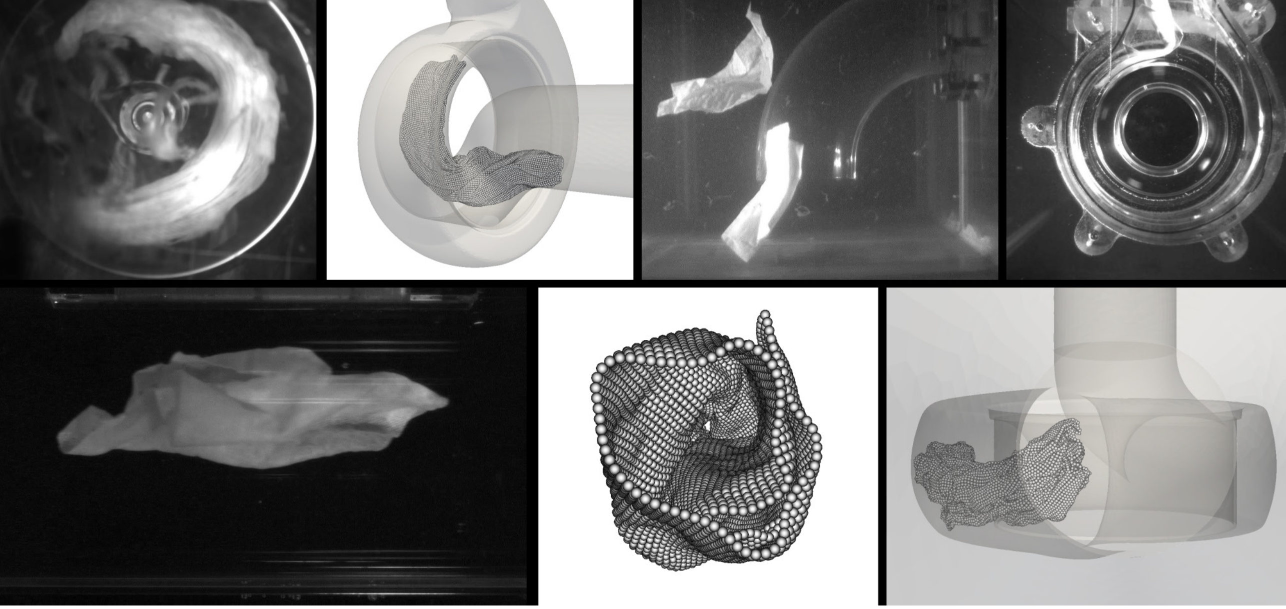

CHARACTERISATION OF RAG PROPERTIES AND THEIR TRANSPORT IN WASTEWATER PUMPS

CALIBRATION OF A DISCRETE ELEMENT RAG MODEL TO SIMULATE CLOGGING EFFECTS

BY
ANNA LYHNE JENSEN

DISSERTATION SUBMITTED 2018

AALBORG UNIVERSITY
DENMARK

Characterisation of rag properties and their transport in wastewater pumps

Calibration of a discrete element rag model to simulate clogging effects

Ph.D. Dissertation

Anna Lyhne Jensen

Dissertation submitted June 2018

Dissertation submitted: June, 2018

PhD supervisor: Prof. Lasse Rosendahl
Aalborg University

Assistant PhD supervisors: Assoc. Prof. Henrik Sørensen
Aalborg University

Prof. Dr.-Ing. Paul Uwe Thamsen
Technische Universität Berlin

PhD committee: Professor Erik Lund (Chairman)
Aalborg University

Professor Francois Henri Léon Raymond Clemens
Delft University of Technology

Docent Ronnie Anderson
Chalmers University

PhD Series: Faculty of Engineering and Science, Aalborg Universit

Department: Department of Energy Technology

ISSN (online): 2446-1636
ISBN (online): 978-87-7210-211-5

Published by:
Aalborg University Press
Langagervej 2
DK – 9220 Aalborg Ø
Phone: +45 99407140
aauf@forlag.aau.dk
forlag.aau.dk

Printed in Denmark by Rosendahls, 2018

Abstract

Accumulation of sanitary refuse, such as wet wipes, in wastewater pumps deteriorates the pump performance, ultimately leading to break-down with need of manual cleaning. To prevent this, the ability of wastewater pumps to handle wet wipes, rags and similar materials in the wastewater is a key feature which must be taken into account as the pumps are designed. Today, simulations are widely used in the design of pumps and other turbomachines. However, the complexity of simulating a flexible material such as a rag in a pump has so far prompted experimental investigation of resistance to clogging rather than simulations.

Using the Discrete Element Method, a model of a rag formed by bonded particles is developed. The model is calibrated based on experimentally obtained quantitative parameters describing the elongation-, bending- and drape properties of the rag. By implementing separate parameters for the normal bond stiffness and out of plane bending stiffness of the bonds connecting the particles which form the rag, the model successfully reproduces elongation, bending and drape obtained from experiments. By coupling the discrete element rag model to Computational Fluid Dynamics using a standard drag model for fluid-particle interaction, a preliminary simulation of the transport of a rag through a wastewater pump with a single channel impeller is achieved.

Furthermore, this study experimentally characterises motion of textile material immediately upstream of a wastewater pump and inside a pump using artificial wastewater containing rags. Clear differences in the tendency of the rags to get stuck on the tongue, stay in the volute flow or exit the pump depending on the operating point have been identified and the flow conditions inside the pump rather than at the inlet have been observed to lead to different types of clogging at different pump operating points.

The result of the preliminary simulation of rag transport through a wastewater pump resembles the motion of the rags through a pump which was observed experimentally.

Resumé

Akkumulering af hygiejneprodukter, som vådservietter, i spildevandspumper forringer pumpens virkningsgrad og kan ultimativt føre til nedbrud som kræver manuel udbedring. Spildevandspumpers evne til at håndtere vådservietter, klude og lignende materialer i spildevandet er vigtig for at undgå dette, og skal derfor tages i betragtning når pumperne designes. I dag bliver simuleringer brugt i vid udstrækning under design af pumper og andre turbomaskiner. Imidlertid har kompleksiteten af at simulere fleksible materialer som en klud i en pumpe indtil nu medført at pumpers evne til at modstå tilstopning er blevet undersøgt eksperimentelt frem for gennem simuleringer.

En model af en klud er udviklet ved at bruge discrete element metoden. Modellen forbinder partikler med bindinger for at repræsentere kluden. Modellen kalibreres baseret på kvantitative eksperimentelle data som beskriver kludens forlængelse, udbøjning og draperingsegenskaber. Efter implementering af seperate værdier for stivheden af bindingerne i normalretningen og udbøjningsstivheden af bindingerne mellem partiklerne som danner kluden kan modellen genskabe forlængelsen, udbøjningen og draperingen fundet eksperimentelt. Ved at koble discrete element metoden til computational fluid dynamics med en standard drag model til fluid-partikel interaktion, kan en foreløbig simulering af transporten af en klud gennem en pumpe med en 1-kanals løber gennemføres.

Dette studie karakteriserer desuden bevægelsen af tekstilmateriale umiddelbart opstrøms for en spildevandspumpe og inden i pumpen ved at bruge kunstigt spildevand som indeholder klude. Klare forskelle i tendensen af kludene til at sætte sig på tungen, blive i strømingen i spiralhuset eller forlade pumpen afhængigt af operationspunktet blev identificeret og det blev observeret at strømingen inden i pumpen frem for ved indløbet fører til forskellige typer af tilstopning ved forskellige operationspunkter.

Resultaterne af den foreløbige simulering af transporten af en klud gennem en spildevandspumpe viser god overensstemmelse med bevægelsen af klude der blev observeret eksperimentelt.

Preface

This dissertation is submitted to the Doctoral School of Engineering and Science at Aalborg University in partial fulfilment of the requirements for the Danish Ph.D. degree. It covers research work in the Department of Energy Technology at Aalborg University from the period September 2014 to March 2018, including a four month exchange in the Department of Fluid System Dynamics at Technical University of Berlin supported by the Nordic Water Network. The work has been under supervision of professor Lasse Rosendahl and associate professor Henrik Sørensen from Aalborg University and Prof. Dr.-Ing. Paul Uwe Thamsen from Technical University of Berlin. The work is co-funded by Grundfos and the Department of Energy Technology at Aalborg University.

Thesis Structure

The topic of this dissertation is experimental and numerical investigation of transport of rags in wastewater pumps. This is motivated by a large amount of clogging events in wastewater pumps caused by rags and similar materials, leading to down time of the pumps in wastewater pumping systems. A specific rag is used to represent the materials causing clogging. The properties of the rag are determined through a series of standard textile tests. The results of these tests are implemented in a rag model developed using the Discrete Element Method (DEM) with particle bonds. The DEM rag model is coupled to a URANS simulation of the flow inside a wastewater pump and a preliminary simulation of the motion of the rag through the pump is presented. Using test rigs with major parts constructed in acrylic glass the motion of the rag at the inlet to a wastewater pump and through the pump is characterised experimentally. These results can be used to determine initial conditions of the rag for coupled simulations, and to validate the simulated motion of the rag through the pump.

The thesis organised in a paper based structure, meaning that it consists of three parts. Part I is a summary report giving an overview of the work. This is followed by Part II, which contains appendices. Finally, Part III consists of a selection of the papers published during the PhD. These papers are listed under Thesis Details on the following page.

Acknowledgements

I would like to express my sincere gratitude to my supervisors from Aalborg University, Department of Energy Technology, Assoc. Prof. Henrik Sørensen and Prof. Lasse Rosendahl for discussions and their guidance throughout the project.

I would also like to thank my supervisor from TU Berlin Prof. Dr.-Ing. Paul Uwe Thamsen for welcoming me to the Chair of Fluid System Dynamics, where I had the pleasure to stay for 4 months during my study. Additionally, I would like to thank Nordic Water Network for funding my stay. During my time in Berlin, I was lucky to be met with open arms by my new colleagues. I would like to thank everyone in the Chair of Fluid System Dynamics for giving me a great experience, and Raja Abou Ackl and Stefan Gerlach for their help in preparing my experiments.

I would also like to express my gratitude to Katharina Ellmer from HTW Berlin for her help and advice on the textile tests conducted in HTW Berlin and for proofreading of the chapter documenting these experiments.

Moreover, I would like to thank Flemming Lykholt-Ustrup, Per Adamsen, Poul Johannes Henning, Nicholas Pedersen and Christian Brix Jacobsen from Grundfos for discussions on status meetings and for the pump geometry and CFD mesh they provided.

A big thank you is also extended to my colleagues in Department of Energy Technology with special thanks to my office mates Jakob Hærvig, Marie Cecilie Pedersen and Anders Schou Simonsen.

Finally I would like to thank my family and friends for their support throughout my studies, especially my boyfriend Uğur, who has been a great support despite much time apart.

Anna Lyhne Jensen
Aalborg University, June 8, 2018

Thesis Details

Thesis Title: Characterisation of rag properties and their transport in wastewater pumps - Calibration of a discrete element rag model to simulate clogging effects
Ph.D. Student: Anna Lyhne Jensen
Supervisors: Prof. Lasse Rosendahl, Aalborg University
Assoc. Prof. Henrik Sørensen, Aalborg University
Prof. Dr.-Ing. Paul Uwe Thamsen, Technische Universität Berlin

The main body of this thesis is based on the following selected papers, which have been completed during the PhD period. The papers are found in Part III of this dissertation.

Journal Papers

[A] Anna Lyhne Jensen, Henrik Sørensen, Lasse Rosendahl and Paul Uwe Thamsen, "Analysis of Textile Morphology and Position Upstream of a Wastewater Pump", *Urban Water Journal*, vol. 15, no. 2 , pp. 132–137, 2018. https://doi.org/10.1080/1573062X.2017.1414274.

[B] Anna Lyhne Jensen, Henrik Sørensen, Lasse Rosendahl, "Analysis of Textile Motion inside a Submersible Wastewater Pump", the paper is under review.

Conference Papers

[C] Anna Lyhne Jensen, Raja Abou Ackl, Stefan Gerlach, Henrik Sørensen, Lasse Rosendahl and Paul Uwe Thamsen, "Experimental Investigation of the Motion and Shape of Flexible Objects near a Pump Inlet", *20th Australasian Fluid Mechanics Conference*, Perth, Australia, December 5-8, 2016. https://people.eng.unimelb.edu.au/imarusic/proceedings/20/597%20Paper.pdf

[D] Anna Lyhne Jensen, Henrik Sørensen and Lasse Rosendahl, "Towards Simulation of Clogging Effects in Wastewater Pumps: Modelling of Fluid Forces on a Fiber of Bonded Particles using a Coupled CFD-DEM Approach", *International Symposium on Transport Phenomena and Dynamics of Rotating Machinery,* Honolulu, Hawaii, April 10-15, 2016.

[E] Anna Lyhne Jensen, Lasse Rosendahl, Henrik Sørensen and Flemming Lykholt-Ustrup "Towards simulation of clogging effects in wastewater pumps: A review of the state-of-the-art in cloth modelling and challenges in the simulation of clogging effects", *ASME-JSME-KSME Joint Fluids Engineering Conference 2015*, vol. 1: Symposia, pp. 2543–2549, Seoul, South Korea, July 26-31, 2015.
https://doi.org/10.1115/AJKFluids2015-33214

In addition the included papers, the following publications were completed during the PhD period.

Journal Papers

[1] Henrik Sørensen and Anna Lyhne Jensen, "Visualization of the motion of textiles through a waste water pump at different operating points", *Journal of Flow Control, Measurements & Visualization*, vol. 6, no. 1, pp. 39–47, 2018. https://doi.org/10.4236/jfcmv.2018.61004.

[2] Jakob Hærvig, Ulrich Kleinhaus, Christoph Wieland, Hartmut Spliethoff, Anna Lyhne Jensen, Kim Sørensen, Thomas Condra, "On the adhesive JKR contact and rolling models for reduced particle stiffness discrete element simulations", *Powder Technology*, vol. 319, pp. 472–482, 2017. https://doi.org/10.1016/j.powtec.2017.07.006.

Conference Papers

[3] Jakob Hærvig, Anna Lyhne Jensen, Henrik Sørensen, "Numerical and Experimental Study of the Rotational Behaviour of Flat Plates Falling Freely with Periodic Oscillating Motion", *Fluids Engineering Division Summer Meeting*, Waikoloa, Hawaii, July 30 - August 3, 2017.
https://doi.org/10.1115/FEDSM2017-69503

[4] Anna Lyhne Jensen, Stefan Gerlach, Flemming Lykholt-Ustrup, Henrik Sørensen, Lasse Rosendahl and Paul Uwe Thamsen, "Investigation of the Influence of Operating Point on the Shape and Position of Textile Material in the Inlet Pipe to a Dry-installed Wastewater Pump", *Fluids Engineering Division Summer Meeting*, Waikoloa, Hawaii, July 30 - August 3, 2017. https://doi.org/10.1115/FEDSM2017-69298

[5] Henrik Sørensen, Anna Lyhne Jensen, Jakob Hærvig, "Flow structures generated by elongated plates settling in a water column", *20th Australasian Fluid Mechanics Conference,* Perth, Australia, December 5-8, 2016. http://people.eng.unimelb.edu.au/imarusic/proceedings/20/586%20Paper.pdf.

[6] Anna Lyhne Jensen, Henrik Sørensen, Lasse Rosendahl, Per Adamsen and Flemming Lykholt-Ustrup "Investigation of Drag Force on Fibres of Bonded Spherical Elements using a Coupled CFD-DEM Approach", *International Conference on Multiphase Flow*, Florence, Italy, May 22-27, 2016.

[7] Jakob Hærvig, Anna Lyhne Jensen, Henrik Sørensen and Marie Cecilie Pedersen "General Observations of the Time-Dependent Flow Field Around Flat Plates in Free Fall", *ASME-JSME-KSME Joint Fluids Engineering Conference*, vol. 1: Symposia, pp. 978–983, Seoul, South Korea, July 26-31, 2015. https://doi.org/10.1115/AJKFluids2015-12708

Contents

Terminology

Acronym	Description
ALE	Arbitrary Eulerian Lagrangian
BEP	Best Efficiency Point
BW	Baby Wipes
CFD	Computational Fluid Dynamics
CoW	Cosmetic Wipes
CW	Crosswise (short side) of rag surface
DEM	Discrete Element Method
FEM	Finite Element Method
IBM	Immersed Boundary Method
LW	Lengthwise (long side) of rag surface
SPH	Smoothed Particle Hydrodynamics
TW	Toilet Wipes
URANS	Unsteady Reynolds-Averaged Navier-Stokes

Word	Description
Dust cloth / rag	Textile material used in the present work to create artificial wastewater
Artificial wastewater	Clean water containing objects such as rags to imitate real wastewater
EDEM	Commercial DEM software
ANSYS Fluent	Commercial CFD software

Latin Variables	Description	Unit
a	Slope of applied force in elongation test	N/m
A	Area	m^2
BI	Blockage index	-
B_i	Number of samples	-
B_p	Number of samples passing the pump	-
D	Drape coefficient	-
D_C	Degree of contamination	-
D_F	Functional performance degree	-
D_LTF	Long term functional performance degree	-
E	Youngs modulus	Pa
E^*	Equivalent Young's modulus	Pa
F	Force	N
FEI	Functional Efficiency Index	-
g	Gravitational acceleration	-
G	Shear modulus	Pa
G^*	Equivalent shear modulus	Pa
H	Head	m
I	Area moment of inertia	m^4
J	Polar moment of inertia	m^4
l	Length	m
L	Length	m
k	Stiffness constant	N/m
m	Mass	kg
m^*	Equivalent mass	kg
M	Moment	m
r	Radius	m
R^*	Equivalent particle radius	m
RI	Rag incidence	-
P	Power	J/s
Q	Volume flow	m^3/s
S	Bond stiffness per unit area	N/m^3
S_p	Particle stiffness	N/m
t	Time	s
v	Velocity	m/s
w	Weight per area	kg/m^2
x	Position	m

Greek Variables	Description	Unit
α	Weighting factor	-
β	Weighting factor	-
β	Coefficient accounting for kinetic energy dissipation	-
γ	Weighting factor	-
δ	Particle overlap	m
ϵ	Strain	-
θ	Angle	degree
ν	Poisson's ratio	-
ρ	Density	kg/m^3
σ	Stress	Pa
ω	Rotational velocity of impeller	RPM

Subscripts	Description
avg	mean
b	bending
b	bond
c	collision
c	contact
c	critical
d	disk
d	damping
exp	experiment
dyn	dyn
f	fluid
g	gravity
m	model
max	maximum
n	normal
rel	relative
p	particle
s	surface
t	tangential
x	x-direction
y	y-direction
z	z-direction
i	i$^{\text{th}}$ entry
0	initial

Part I

Summary

Chapter 1

Introduction

The introduction firstly establishes an overview of the solid content in wastewater and the cause of clogging in wastewater pumps. This is followed by a description of previous and on-going experimental work in the field. Furthermore, based on the review of simulation approaches used in similar contexts presented in Paper E, the CFD-DEM approach is chosen for simulation of clogging effects. The chapter is concluded with a definition of project objectives, methodology and an outline of the dissertation and the enclosed papers.

1.1 Sanitary Wipes Clogging Wastewater Pumps

Wastewater is water transporting waste away from the origin in populated areas with households and factories. In industrial countries the wastewater is transported to wastewater treatment plants through a complex wastewater system of channels, pressure pipes and wastewater pumping stations. In the city of Berlin around 150 pumping stations ensure that sewage is transported to 6 purification plants. These wastewater pumping stations are connected with around 9300 km of channels and a pressure pipeline network of 1100 km, transporting around $230 \cdot 10^6$ m^3 of wastewater annually (Berliner Wasserbetriebe, 2016; Thamsen, 2009). On a European scale, there were an estimated 16 million wastewater pumps in 2011, accounting for an annual energy consumption of 273 PJ (Bio by Deloitte, 2014). This vast amount of pumps and the high energy consumption underlines the importance of keeping the efficiency of the pumps as high as possible, but also the need for reliable operation of each component in the system.

Excluding surface runoff, domestic wastewater consists of water from dishwashers, washing machines, sinks and showers as well as human waste and toilet paper from toilets, along with substantial amounts of hygiene products such as sanitary wipes, sanitary towels, diapers and similar materials.

Fig. 1.1: From left to right: Materials from wastewater obtained from the mechanical cleaning stage in wastewater treatment plants, clogged impeller, and example of wet wipes found in wastewater samples (TU Berlin, Chair of Fluid System Dynamics).

These hygiene products, with common properties of high flexibility and high tensile strength, cause problems in the wastewater pumping system as they are not easily degradable (Davies et al., 1998). The content of these solids in wastewater has been investigated by several authors over the last 50 years using questionnaires or samples of wastewater (Niessen and Chansky, 1970; Friedler et al., 1996). Recently, Spence et al. (2016) and Mitchell et al. (2016) analysed the solids content in various wastewater samples. Spence et al. (2016) investigated the wastewater in three catchment areas with different economic, age and ethnic population profiles and found that wet wipes was the most common pollutant in each of these areas. Mitchell et al. (2016) analysed samples from two catchment areas in Berlin. The distribution of content in a total 13 samples varied significantly. However, paper constituted the biggest amount of solids in the wastewater, followed by textile of which around 65 % were wet wipes. Interestingly, Mitchell et al. (2016) also analysed the material found in clogged pumps and reached the conclusion that 94 % of this material was textiles. Furthermore, synthetic non-woven wet wipes constituted 47 % of these textiles. This identifies wet wipes as a main cause of clogging in wastewater pumps. Figure 1.1 gives an example of solid materials found in wastewater and Table 1.1 summarises the mentioned investigations of the solids content in wastewater.

Two overall types of pumping stations are used to transport wastewater. These are wet pit pumping stations as sketched in Figure 1.2 to the left and pumping stations with dry installed pumps as sketched in Figure 1.2 to the right. As wet wipes and similar objects accumulate in the wastewater pumps, the pump efficiency is reduced, leading to increased operational costs and ultimately pump breakdown. This phenomenon is also known as blockage or clogging. Clogging results in expensive downtime and need for manual cleaning as well as a risk of overflow of wastewater. This is a recurring issue in the wastewater pumping system, as exemplified in Figure 1.3. The figure illustrates the number of failure events which occurred in 44 of the pumping

Composition of Solids in Wastewater				
Ref.	Method	Measure	Textiles / Wipes	Categories
A	analysis of samples	mass "as-fired"	2.7% / -	Glass, metal, paper, plastics, leather, rubber, textile, wood, food wastes
B	questionnaires	occurence	15% / 14.4%	Objects flushed in toilets: e.g. Tampons, wet wipes, tissue paper, cat faeces, dental floss, panty liners
C	analysis of samples	mass	- / $\sim$ 5%	Faeces, toilet tissue, wipes, tampons, panty liners, cotton buds, sanitary towels, sanitary towel shells
D	analysis of samples from catchment area	dry weight	33% / 14%	plastics, textiles, papers, wood and leaves, rest
D	analysis of samples from clogged pump	dry weight	94% / 47%	plastics, textiles, papers, wood and leaves, rest

Table 1.1: Percentage of textile material and wet wipes among solids found in wastewater. A) Niessen and Chansky (1970), B) Friedler et al. (1996), C) Spence et al. (2016), D) Mitchell et al. (2016).

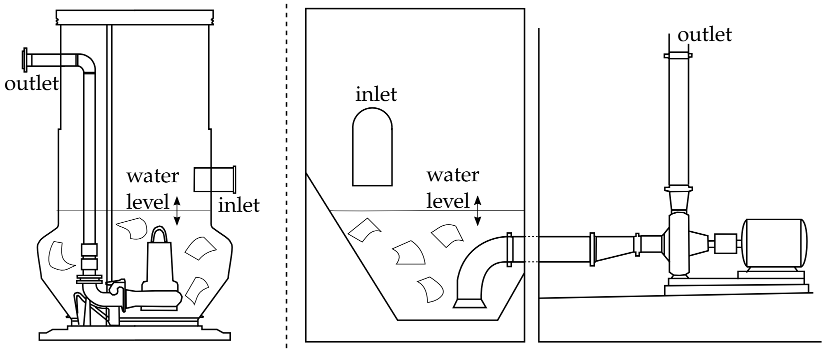

Fig. 1.2: Left: Sketch of a wet pit with a wastewater pump submersed in the wastewater (Paper C). Right: Sketch of pumping station with a dry installed pump placed in a room separated from the wastewater. Clogging occurs when the objects sketched in the wastewater accumulate in the pump.

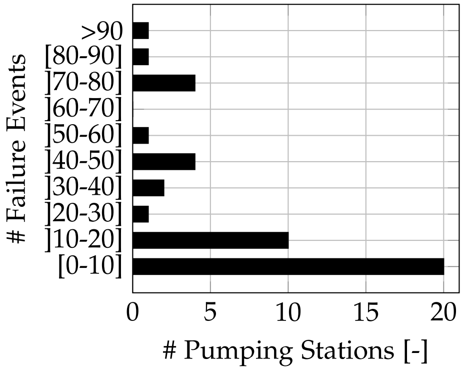

Fig. 1.3: Failure events in pumping stations in North-East Berlin (January 2010 - June 2011) (Höchel et al., 2012).

stations in North-East Berlin between January 2010 and June 2011. It is based on a total of 1112 failure events, corresponding to around two failure events per week in the period (Höchel et al., 2012). Similarly, Korving et al. (2006) investigated the number of wastewater pump failures in Rotterdam and Amsterdam and found that the average number of failure events per pump in Amsterdam in the period 1998-2002 was 4.3 yearly with an average duration of 13.5 hours. For the same period the average number of failure events per pump in Rotterdam was 13 yearly with an average duration of 10 hours. The amount of failure events documented for these cities leads to major expenses for the pump operators. Depending on the severity of the problem, a manual cleaning of a clogged wastewater pump is estimated to cost from 310 € and up (Gerlach et al., 2016), and maintenance is estimated to constitute around 10-20 % of the life cycle costs of wastewater pumps (Flygt, 2012; Andersen, 2012). Consequently, the ability of a wastewater pump to pump without clogging is of major importance.

Due to poor possibilities of visual access to wastewater pumps and the complexity of simulating clogging phenomena, the present understanding of clogging effects is limited. Current work on decreasing the risk of clogging includes continued work to classify and characterize wastewater (Mitchell et al., 2017), and to define a functional performance of wastewater pumps which includes both the efficiency and a measure of how well a pump performs as it pumps highly contaminated wastewater (Pöhler et al., 2015). Moreover, it includes increased use of cleaning sequences with counter rotation of the impeller and development of a method to measure if a pump is beginning to clog (Gerlach et al., 2016). The majority of experimental investigations use artificial wastewater consisting of clean water and objects to represent the solids found in real wastewater.

1.2 Clogging Tests and Artificial Wastewater

Wastewater is an inhomogeneous multiphase fluid containing sand, fat and different types of sanitary refuse as characterised by (Niessen and Chansky, 1970; Friedler et al., 1996; Spence et al., 2016; Mitchell et al., 2016). Due to the nature of wastewater, and the clear hygiene problems this entails, using real wastewater in clogging experiments gives rise to several challenges. Instead, present experimental work uses artificial wastewater, which is clean water with objects added to represent the solids content of real wastewater. Objects such as diapers, plastic bags, rags of different kinds, rubber gloves, sponges, rope and similar materials have been used to create artificial wastewater for clogging tests. Due to large variations in the solids content in wastewater, a clear scientific description with classification of different types of wastewater depending on the solids content is yet to be defined, and there is no standardised method to investigate and compare the ability of different pumps to resist clogging.

In the absence of a standardised method to create artificial wastewater, experimental investigations of clogging effects have been presented using different objects to create the artificial wastewater. Among these are Isono et al. (2014), who used three types of rope with diameters of 4 mm, 9 mm and 12 mm respectively and with lengths of 1, 2 and 5 times the diameter of the pump outlet in three different pumps. They concluded among other things that especially the length of the ropes affects the risk of clogging. Apart from this, different studies have used rags, more similar to the wet wipes which are often the cause of clogging (Mitchell et al., 2017).

McEvoy (2011) used household j-cloths as test material, and recorded these j-cloths one at the time as they entered a pump impeller. Based on these experiments the ability of different pump geometries to pump the j-cloth without clogging was assessed using design of experiments and evaluating the anti-clogging performance with a blockage index as defined in Equation (1.1).

$$BI = \frac{B_\mathrm{p}}{B_\mathrm{i}} \cdot 100 \tag{1.1}$$

Here B_p is the number of samples that passes the pump and B_i is the total number of samples introduced. Additionally, based on the recordings of one j-cloth at the time, different types of hydraulic blockages were identified. These were impeller leading edge, impeller eye, impeller tip gap and volute recirculation and tongue blockage.

Connolly (2017) initially used heavy duty sanitary towels to create artificial wastewater, but due to rapid degradation of the towels affecting the visibility, they were replaced with macrotek wipes (222 mm × 222 mm). Connolly (2017) used the blockage index as defined in Equation (1.1) to evaluate the ability of pumps to handle the makrotek wipes, and additionally defined a non-dimensional rag incidence, shown in Equation 1.2, and investigated how the blockage index depends on the rag incidence.

$$RI = \frac{Al\omega}{Q} \tag{1.2}$$

In the equation above, A is the area of the gap between the impeller leading edge and the impeller trailing edge, l is the length of the rag, ω is the rotational speed of the impeller and Q is the volume flow rate of water through the pump.

Thamsen (2009) used synthetic non-woven Aro super dust cloths (220 mm × 300 mm) in a series of experiments to determine how the type of clogging depends on the operating point of the pump. Subsequently, this type of dust cloths have been used in the work by Pöhler et al. (2015) to develop a standardised method to evaluate wastewater pumps not only based on their efficiency but also on the ability to handle highly contaminated wastewater. Pöhler et al. (2015) defined a functional performance degree (D_F) similar to the blockage index presented by McEvoy (2011). However, Pöhler et al. (2015) tested the long term operation using hundreds of dust cloth samples. This meant that many of the samples had been torn apart at the end of the test and therefore the functional performance degree was measured by dividing the dry weight of the pumped material with the dry weight of the total amount of samples used in a test. Using this functional performance degree, Pöhler et al. (2015) defined a functional efficiency index (FEI) as presented in Equation (1.3).

$$RI = (\alpha \cdot D_\mathrm{c} + \beta \cdot D_\mathrm{F} + \gamma \cdot D_\mathrm{LTF}) \frac{\rho \cdot g \cdot H \cdot Q}{P} \tag{1.3}$$

Where D_C is the degree of contamination and D_LTF is a long term functional performance degree, which is determined by comparing the pump efficiency at the beginning of the test (0-10 min) with the pump efficiency after 50-60 min. Finally, α, β and γ are weighting factors. Subsequently, Gerlach et al. (2017) also used the dust cloths to investigate the ability of different vortex impeller designs to handle textile material in wastewater.

It is common for the described experimental studies using artificial wastewater to choose test objects which are not easily degradable and which will have a relatively long lifetime during experiments and ensure good visibility. Based on the work by Thamsen (2009), Pöhler et al. (2015) and Gerlach et al. (2017), and on the aim by Pöhler et al. (2015) to create a test standard, the synthetic non-woven Aro super dust cloth is currently the closest one can get to a standard textile for evaluating the ability of wastewater pumps to handle textile, and this will be used to represent the objects in wastewater throughout the present work.

The experimental studies on clogging in wastewater pumps have increased the understanding of clogging phenomena and identified different types of clogging at different operating points. However experimental investigations are expensive, including experimental investigations on prototypes in the design process. Therefore, simulation of clogging phenomena is a key step in further investigations of clogging in wastewater pumps.

1.3 Potential Impact of Simulation of Clogging Effects

Simulations are widely used in the design of pumps and other turbomachines. Basing new product designs on computational results rather than practical experience and experiments on prototypes significantly facilitates the design process. Applications of Computational Fluid Dynamics (CFD) simulations in the design process of pumps already include prediction of pump performance at different operating points, cavitation analysis, investigation of erosion, and optimization of pump design. However, in spite of a very rapid development of computational methods along with increasing computational power, simulation of clogging effects is not yet a part of the design process of wastewater pumps. A general investigation from 2006 on the use of simulation tools in the design phase showed that all the best in class manufacturers used simulation in the product design phase, and recommended that simulation of product performance in the early design phase is performed. Furthermore, the investigation showed that the best in class manufacturers on average produced 1.6 fewer prototypes than other companies, thereby reducing the length of the development cycle (Aberdeen Group, 2006). This motivates the development of a methodology for simulating clogging effects to reduce the need for testing of prototypes to determine if pump designs are resistant to clogging. Furthermore, due to the difficulty of enabling visual access to pumping systems for detailed experimental investigations, simulation has potential to improve the overall understanding of clogging effects and thereby help to identify design features which can reduce the risk of clogging.

1.4 Choice of Simulation Approach

Simulation of clogging phenomena in wastewater pumps requires simulation of 1) the flexible textile materials causing clogging, 2) a 3D transient pump simulation and 3) a coupling between the textile model and the simulated flow through the pump. Since only a very limited amount of work has previously been published on simulation of clogging effects, the first step towards achieving this is the choice of an appropriate simulation method. In order for a method to be appropriate it should be accurate, the computational requirements should be affordable and ideally the method should have been used in similar cases. This is the topic of Paper E: *"Towards simulation of clogging effects in wastewater pumps: A review of the state-of-the-art in cloth modelling and challenges in the simulation of clogging effects"*, where advantages and disadvantages of different methods are discussed.

As discussed in Paper E, several approaches to modelling of textile materials in fluid have been presented in literature. The approaches reviewed in Paper E are the Arbitrary Eulerian Lagrangian method, the Immersed Boundary method, Smoothed Particle Hydrodynamics simulating the fluid coupled with a finite element model of the textile and finally, Computational Fluid Dynamics simulating the fluid coupled to a discrete element model of the textile (CFD-DEM). Following the conclusion of Paper E, the present work uses the CFD-DEM approach because of advantages in computational speed and the ease of handling interactions between the textile material and pump impeller as well as interactions as the textile material crumbles and self-collides. Choosing DEM to model textile material requires development of a bond model and development of a calibration method to include the properties of textile in the model.

Simulation of the fluid flow in pump geometries is commonly achieved using Computational Fluid Dynamics (CFD) with a finite volume based solver and an unsteady Reynolds-averaged Navier-Stokes (URANS) approach to turbulence modelling. Even though the URANS turbulence modelling is not resolving the turbulent behaviour of the flow, it has been used for industrial flow simulations such as the flow in pumps for decades and must now be considered a mature approach for this application. Therefore the choice of this approach enables the textile model to become a plug-in model that can be an addition to simulations already made in the design process of wastewater pumps. As discussed in Paper E, using CFD with URANS for turbulence modelling for the flow simulation and DEM for the textile simulation, the textile material is not resolved by the fluid mesh and the interaction between the textile and the fluid is based on fluid force models. By not resolving the textile material, computationally expensive mesh update is avoided, which is a clear advantage for the computational feasibility of the simulation.

Note that Specklin et al. (2017) recently used a Lattice-Boltzmann solver for the flow equations and a finite difference method to model the textile using the Immersed Boundary Method to couple the fluid and the textile with good results. Similar to the present work, the work by Specklin et al. (2017) is part of a project to develop a method to simulate clogging effects in wastewater pumps.

With the choice of CFD-DEM as the simulation approach in the present work, the project objectives are presented in the following.

1.5 Project Objectives

The ability of wastewater pumps to handle sanitary refuse in wastewater without clogging is essential. To facilitate the design process of wastewater pumps, the present work moves towards a long term aim of including clogging simulations in the design process of wastewater pumps to reduce the need of prototypes. Considering CFD simulation of the flow in pump geometries a mature approach using a finite volume based solver and URANS for turbulence modelling, the main challenge in reaching this aim is the development of a reliable textile model using the Discrete Element Method with bonded particles and the coupling between the textile and the fluid. Experimental work in pumping systems with visual access to key positions close to the pump inlet and in the pump house will enable validation of coupled simulations. The described synthetic non-woven dust cloths are used in all simulations and experiments to ensure coherence with the ongoing experimental work (Thamsen, 2009; Pöhler et al., 2015; Gerlach et al., 2017). The dust cloths will also be referred to as rags.

The project objectives are elaborated with the following objectives:

1. Development of textile model
    a. Identify appropriate material to create artificial wastewater
    b. Determine the properties of the textile material
    c. Identify appropriate method to model textile using DEM
    d. Calibrate textile model based on experiments
    e. Perform validation based on experiments

2. Experimental investigation of the motion of textiles in pumping systems
    a. Identify cases for experimental investigation
    b. Characterise the motion of textile materials in pumping systems

3. Preliminary simulation of a clogging effects
    a. Investigation of appropriate coupling forces
    b. Simulation of the motion of a piece of textile through a pump

Model	Method	Software
Textile	DEM with bonds	EDEM 2017
Fluid	FVM, URANS	ANSYS Fluent 18.1
Coupling	Fluid force models	EDEM-Fluent Coupling 2.2

Table 1.2: Simulation approach used in the present work.

1.6 Methodology

The methods used to reach the three main objectives are described in the following.

Development of Textile Model

The initial focus is on the development of a discrete element model of a rag. The incremental DEM bond model presented by Potyondy and Cundall (2004) and used to model flexible fibres by Guo et al. (2013b) forms a basis for the rag model. The arrangement of the DEM particles to form a flexible rag surface is determined based on a literature study. The tensile, bending and drape properties of the rag are determined through experiments and are used to calibrate and validate the model. The commercial DEM software EDEM is used for the rag model.

Experimental Investigation of the Motion of Textiles in Pumping Systems

Artificial wastewater with rags is used in all experiments. The motion of the rags in three test rigs with major parts constructed in perspex are captured using a fast digital camera. The test rigs enable capturing the motion of the rags in 1) the suction pipe to a dry-installed pump, 2) in the inlet to the impeller of a submersible pump and 3) inside the house of a submersible pump. The experiments are conducted at various pump operating points and the captured images are processed and analysed to describe the transport of rags in each of these locations and the influence of the operating point. The results of the experiments are used to determine appropriate initial conditions of rags in clogging simulations and for validation purposes.

Preliminary simulation of a clogging effects

Computational Fluid Dynamics to simulate the fluid flow through a pump is coupled with the model of a rag developed in this work. Using this coupling the transport of rags through wastewater pumps can be simulated. To simplify the simulation case, the simulation will not take the full complexity of wastewater with the content of fat, sand and textile derivatives into account.

Instead, the aim is to simulate the clogging tests conducted with artificial wastewater as described in Section 1.2.

Until around 2008, simulations coupling CFD and DEM were primarily done using custom in-house codes. Hobbs (2009) described his use of the, at the time, recently available commercial EDEM-CFD Coupling for Fluent. This coupling has later been developed further and version 2.2 of this coupling interface is used for the coupled simulations in the present work. This version of the coupling was introduced in January 2017.

Using this coupling, a CFD simulation of the flow through a wastewater pump geometry is done in ANSYS Fluent and coupled to the rag model developed in EDEM. The rag will not be resolved by the CFD mesh, and the fluid forces on the textile will therefore be determined based on fluid force models. Initial considerations on the modelling of fluid forces on the particles forming the rag are presented along with results of a preliminary simulations of the modelled rag passing through a wastewater pump. Table 1.2 summarises the method and software used for each part of the simulation.

1.7 Outline of Summary Report

The dissertation consists of Papers A-E and a summary report partly based on these papers, which describes the topic in more detail. Figure 1.4 presents an overview of the content of the summary report and indicates the papers which have contributed to each topic. An outline of the content of each chapter in the summary report is given in the following.

Chapter 1: Presents the background and context of the dissertation and introduces the objectives, limitations and the potential impact of simulation of clogging effects. It includes important points from Paper E on the choice of simulation approach. The chapter is concluded with an outline of the project content.

Chapter 2: Briefly describes different types of textile structures, and presents experiments to determine the properties of the rag used to represent textile materials in wastewater. The results of the experiments are presented, and will be used to calibrate and validate the bond model described in Chapter 3.

Chapter 3: Covers the implementation of the rag properties determined in Chapter 2 through DEM particle and bond properties. This is followed by a time step and particle size independence study. The chapter is concluded with an overview of the steps required to model textile using the present approach.

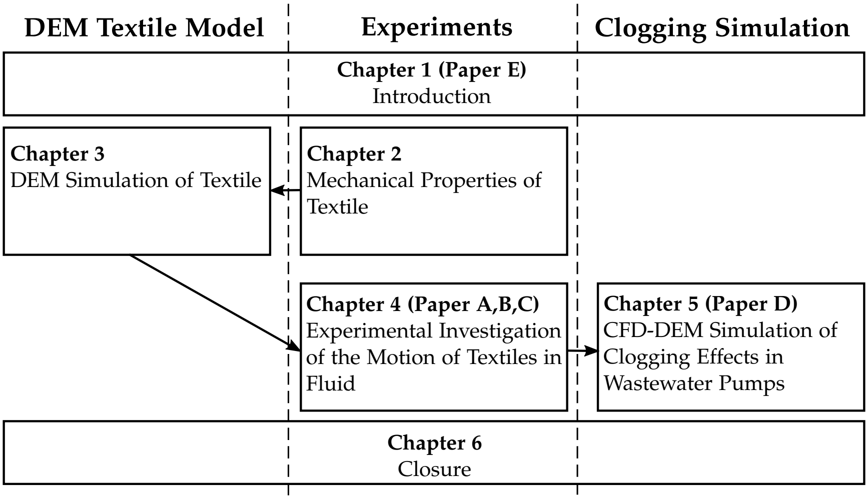

Fig. 1.4: Block diagram of the structure of the summary report.

Chapter 4: Describes experiments conducted in a full scale wet pit, scaled wet pit and a scaled pumping station for dry installed pumps. Images with a fast digital camera during the experiments are processed and analysed to characterise the motion of flexible material near a pump inlet and inside the pump casing. The chapter includes results described in Paper A, B and C.

Chapter 5: Describes the CFD-DEM coupling between ANSYS Fluent and EDEM and discusses fluid forces on fibres and rags. Paper D is included in the discussion. Subsequently, preliminary CFD-DEM simulations of rag transport through a wastewater pump are presented. Firstly, the rag transport is simulated for a pump operating at the best efficiency point and finally the simulation is done for a pump operating in heavy part load.

Chapter 6: Concludes the summary report with conclusions and perspectives for future work.

1.8 Outline of Papers

As described, some of the chapters in the summary report are based on papers completed during the PhD period. The following gives an outline of the content of each paper.

Paper A: Characterisation of Textile Shape and Position Upstream of a Wastewater Pump under Different Part Load Conditions
The shape and position of rags in the suction pipe to a dry-installed wastewater pump is investigated at nine different operating points using image analysis. The results show that the rag properties of elongation ratio, orientation and position are independent of the operating point, while the rag area decreases with an increasing volume flow. Furthermore, the connection between the position of the rags at the inlet to the suction pipe and inside the suction pipe is investigated and can later be used for validation purposes.

Paper B: Case study on the motion of textiles in a waste water pump in part load
A test rig with a single channel centrifugal pump with a transparent pump house is build to characterise the motion of textiles as they move through the pump house and identify differences from operating point to operating point. Three types of textile motion are observed; 1) textiles getting stuck on the tongue; 2) staying in the volute flow; and 3) exiting the pump. Clear differences were observed from operating point to operating point. A tendency of the rag to recirculate in the volute or get stuck on the tongue was observed under part load conditions while the rags passed easily through the pump closer to the best efficiency point.

Paper C: Experimental Investigation of the Motion and Shape of Flexible Objects near a Pump Inlet
The motion of the rags at the impeller inlet to a submersible pump is investigated for a pump operating at 60% of Q_{BEP}, 100% of Q_{BEP} and 120% of Q_{BEP} with highly contaminated artificial wastewater. When operating the pump at the best efficiency point and in overload the rags build up at the inlet to the impeller leading to a significant decrease in the pump efficiency. At heavy part load conditions at 60% of Q_{BEP} the rags do not accumulate at the impeller inlet but cause clogging in the housing at the tongue. This underlines that different types of clogging occur at different operating points and motivates a study of rag transport in a pump with a transparent housing.

Paper D: Towards Simulation of Clogging Effects in Wastewater Pumps: Modelling of Fluid Forces on a Fiber of Bonded Particles using a Coupled CFD-DEM Approach
A fiber model consisting of a string of bonded DEM particles is developed in the software EDEM and coupled to the CFD software ANSYS Fluent. The stiffness of the bonds connecting the particles and the particle density is varied to identify how these properties influence the fibre motion in shear flow. While the change in the stiffness of the bonds had limited influence on the fibre motion, it was clear that a change in particle density affected the results.

Paper E: Towards Simulation of Clogging Effects in Wastewater Pumps: A Review of the State-of-the-Art in Cloth Modelling and Challenges in the Simulation of Clogging Effects
First step towards achieving simulation of clogging effects is to determine an appropriate simulation approach. This paper considers the Arbitrary Lagrangian-Eulerian Method, the Immersed Boundary Method, Smoothed Particle Hydrodynamics coupled to the Finite Element Method and Computational Fluid Dynamics coupled to the Discrete Element Method and discusses advantages and disadvantages of each method in connection with simulation of clogging effects.

Chapter 2

Mechanical Properties of Textile

A description of the structure of textile is followed by a presentation of the experimental approach used to determine the properties of the Aro super synthetic non-woven dust cloth (referred to as 'rag' in the present work), which will be used to create artificial wastewater. The results of the experiments establishes data to calibrate the rag model as described in Chapter 3 and thereby predict the behaviour of the rag in the simulations presented in Chapter 5.

2.1 Micro- and Mesoscale Structure of Textile

A piece of textile consists of fibres ($\sim 10^{-5}$ m), which in woven and knitted textiles form yarns ($\sim 10^{-3}$ m). Textiles are commonly classified based on the structure of these fibres and yarns. Figure 2.1 illustrates examples of A) woven, B) knitted and C) non-woven structures of textile. Within each category several subcategories of weave-, knitting and non-woven structures are found. The structure, interaction and properties of the fibres and yarns in the textile determine the overall properties of the textile, which are normally flexible and porous materials with inhomogeneneous, anisotropic, hysteretic

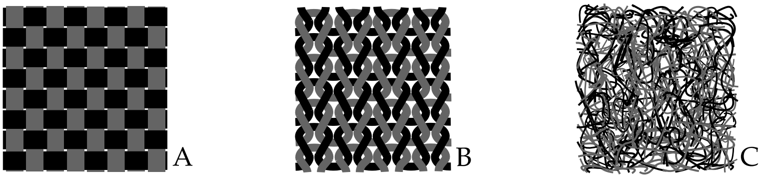

Fig. 2.1: A: Woven textile, B: Knitted textile, C: Non-woven textile.

Dust Cloth (Rag) Properties	
Area	220 × 300 mm (± 10%)
Thickness	0.77 mm
Material	90% polyester, 10% polypropylene
Density (dry)	60 g/m^2 (± 10%)

Table 2.1: Properties of the Aro super synthetic non-woven dust cloth (rag) (Katscher, 2016).

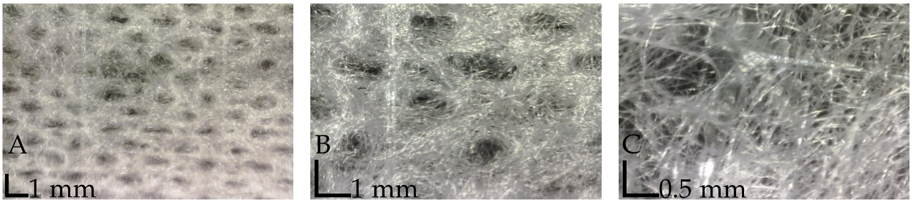

Fig. 2.2: Images of the rag under three levels of zoom.

and viscoelastic properties (House and Breen, 2000; Vassiliadis et al., 2011). Due to these properties, originating from the complex microstructure, accurate modelling of textile is challenging since realism is required but simplicity enabling a fast computational time is also necessary for many applications.

The synthetic non-woven Aro super dust cloths (rags) presented in Section 1.2, which are used to create artificial wastewater in the present work, consist of synthetic non-woven polyester fibres attached to a net of polypropylene. The overall properties of size and density of the rags are listed in Table 2.1. Figure 2.2 illustrates the non-woven rag structure in three levels of zoom. Figure 2.2A illustrates the overall structure of the rag, where small, evenly distributed holes can be seen on the surface and the net of polypropylene is vaguely visible. In Figure 2.2B the individual fibres can be seen and the structure of areas with holes and areas with fibres is more clear. In Figure 2.2C the fibres and the entanglement of the fibres are more clearly visible and a cross in the polypropylene net is seen among the fibres. This structure is clearly in a larger size scale than the fibres in the rag.

Three different scales are used when modelling textile. These are the microscale which focuses on the scale of the fibers, the mesoscale which is assuming the constituent yarns of e.g. woven textiles to be homogeneous and focuses on a unit cell of the yarn structure, and the macroscale which includes prediction of the mechanical properties and deformation such as draping. The present work centres on the macroscale behavior of rags making simplifying assumptions. The properties of the rags are accordingly determined on the macroscale, through tests of bending deformation and drape as well as elongation and breaking strength.

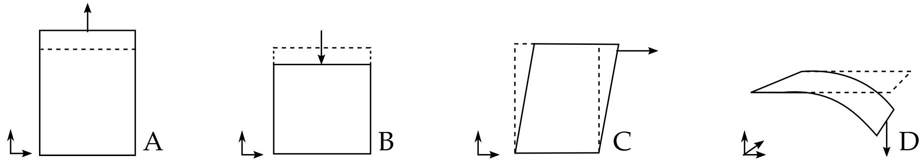

Fig. 2.3: A piece of textile resists deformation in 4 directions. A) Tension, B) Compression, C) Shearing, D) Bending.

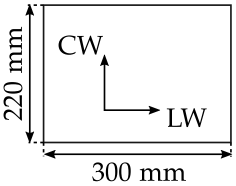

Fig. 2.4: Definition of the lengthwise (LW) direction and crosswise (CW) direction on the rag surface. All tests will be made on samples of the rag representing the LW and CW direction seperately.

2.2 Determination of the Properties of the Rag

A piece of textile resists motion in four directions as sketched in Figure 2.3. Different types of tests to evaluate textiles as they deform in each of these directions have been developed through the last century. In the 1930's, Peirce (1930) proposed the cantilever bending test, which is still commonly used to evaluate the bending properties of textile. During the 1970s, the Kawabata Evaluation System (KES) was developed and has been widely used in the textile engineering community since then. Another widely used approach to textile testing is the Fabric Assurance by Simple Testing (FAST) system. Furthermore, several standards of textile tests have been developed based on the similar principles. However, since the standards do not describe tests of wet textile samples, deviations from the standards were necessary.

The properties of the rag are tested for both the lengthwise (LW) and crosswise (CW) direction as defined in Figure 2.4. The following subsections describe the tests used to determine the properties of the rag. These are a uni-axial breaking strength and elongation test, a cantilever bending test and a drape test. Since the textile materials found in wastewater are wet, the experiments aim to determine the properties of wet rags. The rags were placed in water in a room with standard climate conditions for 24 hours before the tests. The climate conditions were in correspondence with the ISO 139:2005 (2011) standard with a temperature of $20°C \pm 2°C$ and a relative humidity of $65\%^{rH} \pm 2\%^{rH}$. All tests were carried out in cooperation with HTW Berlin using the standard climate facilities available in the Institute of Clothing Technology.

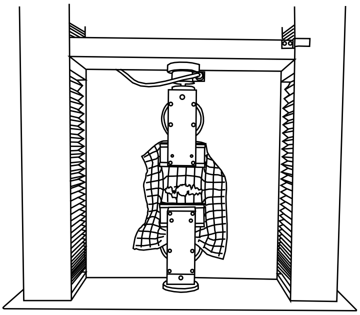

Elongation Test Details	
Sample size	220 × 300 mm (± 10%)
Clamp width	100 mm
Init. clamp dist.	50 mm
Clamp velocity	100 mm/min
Mean density	966 kg/m^3
Repetitions	5×LW, 5×CW

Fig. 2.5: Left: Sketch of the test used to evaluate breaking strength and elongation properties of the rag. A grid is marked on the rag to help identify and characterise the deformation and tearing of the rag. Right: Tabel presenting details on the breaking strength and elongation test.

2.2.1 Breaking Strength and Elongation Test

The breaking strength and elongation test evaluates the force required to elongate and tear a piece of textile as sketched in Figure 2.3A. Different approaches to this type of test include constant rate of extension and constant rate of load. The constant rate of extension is the most common and is also used here. Additionally, there are different approaches to the size of the textile sample compared to the clamps holding the sample during the test. The present experiment uses a grab test where the width of the clamps is smaller than the width of the rag as sketched in Figure 2.5. Another approach uses a strip of textile with the same width as the clamps, so the whole width of the specimen is gripped. The grab test presented in the following, can only give the breaking strength, while the strip test would also give information on the and elongation properties of the specimen (Wang et al., 2008). The described approaches evaluate the uni-axial tensile properties as opposed to bi-axial tensile properties. Uni-axial tests only takes the extension in one direction into account, while the tensile properties in one direction may correlate with the state of the other direction (Bassett et al., 1999). Even though a strip test may give more accurate results on the elongation properties, the output of the present uni-axial grab test is used to estimate and model elongation as a function of the force on the rag.

Figure 2.5 shows a sketch of the test setup. As illustrated in the sketch, a whole rag is fixed between two clamps. A grid is drawn on the rag before the test to mark the polypropylene net inside the rag, which is seen in Figure 2.2C. Every second line of the net in each direction is marked. The grid enables investigation of the deformation of the rag in different areas. The width of the clamps holding the rag is 100 mm, and the initial distance between the clamps is 50 mm. The rag is placed so the net inside the rag marked with

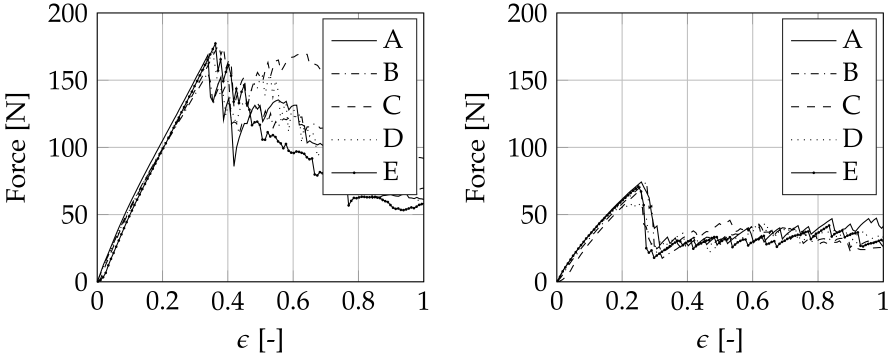

Fig. 2.6: Resulting force as a function of the strain, $\epsilon = \Delta L/L_0$. Left: Lengthwise direction. Right: Crosswise direction.

black is normal and parallel to the clamps. The rag samples were placed in water for 24 hours before the test.

To start the test, a rag was removed from the water, weighed and placed in the setup sketched in Figure 2.5. When the test was initiated, the upper clamp moved upwards with a velocity of 100 mm/min, while the applied force was logged. As the rag was elongated and began to tear, the force required to move the clamp with a fixed velocity decreased. The test was repeated five times for the lengthwise direction and five times for the crosswise direction. The lengthwise and crosswise directions were defined in Figure 2.4.

The results for the lengthwise direction are presented in Figure 2.6 to the left. As seen in the figure, the results of the five tests for the lengthwise direction of the rag have a linear increase with a similar gradient in the first part of the test. The rag begins to tear at around a strain of 0.36, where there is a sharp break in the curve. At this point the force decreases and becomes uneven as the polypropylene net begins to break and the fibres are torn apart. The average value of the maximum force applied in the lengthwise direction is 172 N, with a maximum of 179 N and a minimum of 158 N among the 5 tested rags. The results of the five tests in the crosswise direction are presented in Figure 2.6 to the right. These results are also similar, with similar slopes until the maximum value is reached. The average of the maximum force applied in the crosswise direction is 70.1 N with a maximum of 75.6 N and a minimum of 59.1 N among the five tested rags. These results are significantly lower than the 172 N applied in the lengthwise direction. Furthermore the rags begin to tear at a strain of around 0.26 compared to 0.36 measured for the lengthwise direction.

The results of the breaking strenght and elongation test are summarised in Table 2.2. Factors such as the gauge length and the rate of extension may

Parameter	Unit	Lengthwise	Crosswise
Maximum force, $F_{\text{max,exp}}$	N	172	70.1
Maximum strain, $\epsilon_{\text{max,exp}}$	N	0.358	0.264
Elongation, $\Delta L_{\text{max,exp}}$	m	0.0179	0.0132
Maximum strain, $L_{0,\text{exp}}$	m	0.05	0.05

Table 2.2: Results of the breaking strength and elongation test.

affect the results but these uncertainties have not been considered, and the results summarised in Table 2.2 are implemented in the DEM textile model. The details of the implementation are described in Section 3.3.1.

2.2.2 Bending Test

For continuous material there is a direct relation between tension and bending rigidity. However, due to the discrete micro-structure this does not apply to textiles, where the bending rigidity is very small compared to the tensile rigidity (Teng et al., 1999; Vidal-Salle and Boisse, 2010). Therefore, the bending rigidity is evaluated in a separate test. Ghosh and Zhou (2003) reviewed the measurement principles used in textile bending tests. There are two overall measurement methods. One method measures forces, moments or energy directly as the piece of textile is subject to a specific deformation. This measurement principle is used in the Kawabata Evaluation System. The other approach was introduced by Peirce (1930), who used a cantilever test where a textile sample was bending under its own weight. The textile was assumed to be linear elastic and beam theory was used to determine the bending rigidity. Different tests as the folded loop, heart loop, pear loop, hanging wrinkle, hanging ring and standing ring methods are also commonly used to determine bending rigidity of textiles under their own weight (Plaut, 2015). The cantilever test of bending rigidity is used commercially in the Fabric Assurance through Simple Testing (FAST) system and is also used in the present work. Ghosh and Zhou (2003) notes that bending test results from the FAST system correlates well with results from KES.

The measurements of bending properties using a cantilever test were made based on the DIN 53362:2003-10 (2003) standard. The setup is sketched in Figure 2.7. A sample of the rag of size 25×215 mm was placed on the top of the setup with the front edge aligned to the edge on the setup. A ruler was placed on top of the rag sample with the front edge aligned to the edge of the setup and the rag. The ruler on top of the rag sample was pushed over the edge, and the rag sample was pulled along with the ruler and started bending as illustrated in Figure 2.7. The top plate was pushed until the front of the rag sample was touching a plane between the two lines marked on

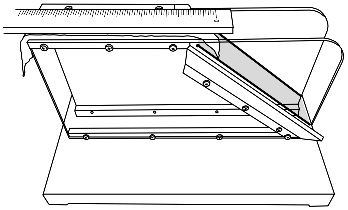

Bending Test Details	
Size of rag sample	25 × 215 mm
Mean density	570 kg/m^3
Repetitions	10 × LW, 10 × CW

Fig. 2.7: Left: Sketch of the setup for the bending test. Right: Table presenting details on the bending test.

the test stand, which is marked with grey in Figure 2.7. The plane has a decline of 41.3 degrees. In total 20 samples were tested, 10 representing the lengthwise direction of the rag and 10 representing the crosswise direction.

Similar to the breaking strength and elongation test, the properties of wet rags are of interest. Therefore the rags were placed in water in a room with standard climate conditions for 24 hours before the test. However, the test approach hindered the use of rags directly from water, since the wet rag sample would stick to the ruler used to push the sample over the edge and measure the bending. To overcome this, the rags were shortly placed in a piece of paper with light pressure applied. This removed some of the water and enabled the bending test to be carried out. This approach changed the density of the wet rag from 800-960 kg/m^3 in the other tests to 570 kg/m^3, and thereby also the bending behaviour. The changed density will be taken into account in when the results of the bending test are implemented in the textile model in Chapter 3.

The results of the bending test for the ten samples representing the lengthwise direction are presented in Figure 2.8 to the left. As seen in the figure the ten repetitions gave similar results with a mean strip length of 33.5 mm. The minimum measured bending length was 31 mm and the maximum was 36 mm. For the crosswise direction of the rag the bending behaviour was different than the lengthwise direction with a mean strip length of 21.5 mm. The maximum measured strip length for the crosswise direction was 24 mm while the minimum measured strip length was 20 mm. Similar to the breaking strength and elongation test, the deviation between the result for the lengthwise and crosswise direction underlines the anisotropic properties of the rag, which will be included in the DEM model.

Table 2.3 summarises the results of the bending test. The mean length of the bending rag sample will be used in simulations of a similar case in Chapter 3 to calibrate the model of the rag.

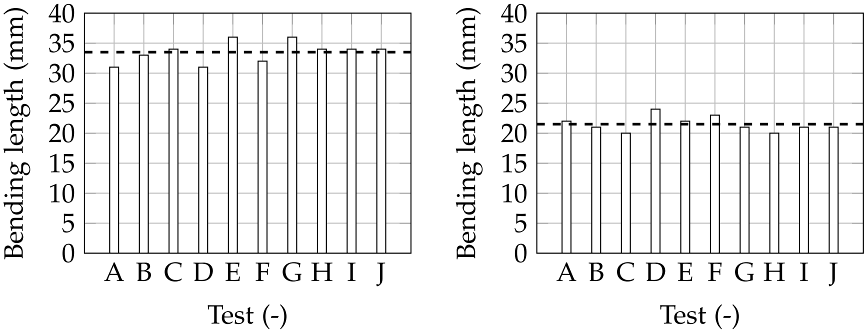

Fig. 2.8: Results of the bending test. Left: Bending length LW direction. Right: Bending length CW direction. The mean bending length is marked with the dashed line in both cases.

Paramenter	Unit	Lengthwise	Crosswise
Mean strip length, l_{avg}	m	0.034	0.021
Weight pr area, w	kg/m^2	0.42	0.38

Table 2.3: Results of the bending test.

2.2.3 Drape Test

While the bending test determined the bending properties of a small strip of the rag in one direction, the drape test evaluates draping of a larger circular rag sample over a circular disc. The drape tests are performed to obtain additional results, which contribute with more possibilities of calibration and validation of the discrete element textile model presented in Chapter 3.

The draping of a circular piece of textile over a circular disc is a very common case for both experiments and simulation of textiles, and the correlation between textile draping and the mechanical properties of textiles has been investigated by several authors (Kenkare and Plumlee, 2005; Sanad et al., 2012). The original drapemeters, commonly used in drape tests, were developed by Chu et al. (1950) and Cusick (1968). The drapemeters are used to test three-dimensional textile drape and identify the drape area and drape coefficient of textile materials. This is sketched in Figure 2.9, where the full line is the outline of a draping rag sample.

In previous studies, the drape characteristics of textile has been estimated using the classical drapemeters by cutting the drape shape out of a circular piece of paper and comparing the weight before and after (Cusick, 1968). But also by observing the amount of light absorbed by photovoltaic cells (Collier et al., 1988) and by image analysis. Vangheluwe and Kiekens (1993) used image analysis and stated that the image analysis approach leads to

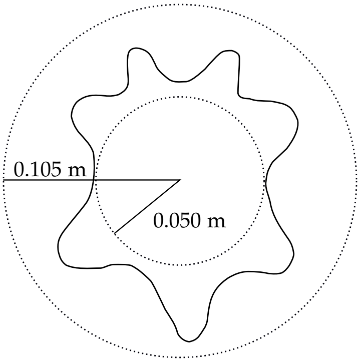

Fig. 2.9: Sketch of the drape area identified in drape tests. The dotted lines show the size of the draping rag sample and the size of the cylinder the rag is draping over. The full line is the outline of the draping rag sample.

more accurate and more rapid results than the conventional method. Image analysis was also used by Jeong (1998) and Jeong and Phillips (1998) among others to analyse fabric drape.

The present test procedure was based on the ISO 9073-9:2009 (2008) standard. However, since the rag was too small to test using the conventional approach with drapemeters (Chu et al., 1950; Cusick, 1968), an alternative test setup with a smaller disc for the rag to drape over was used. The rag drape was captured by a camera as done by Vangheluwe and Kiekens (1993) and Jeong and Phillips (1998). The test setup is sketched in Figure 2.10. As seen in the Figure, the camera was placed directly above the draping rag. The diameter of the disc was 100 mm while the diameter of the circular rag samples was 210 mm. A total of 50 rags were used. The rags were left in water for 24 hours under normal climate conditions to ensure that they were saturated with water before the tests. A wet rag was carefully placed on top of the disc. The centre of the circular rag sample was marked with a hole fitting a small pin in the middle of the disc on which the rag was placed. This ensured that the centre of the rags was indeed place very close to centre of the disc. Each rag was used for six draping test. Three for each side of the rag, resulting in 300 images of draping.

The acquired images were processed in MATLAB to isolate the draping rag in a binary image. The four image processing steps are illustrated in Figure 2.11. The resulting binary image (Figure 2.11E) was used to determine the drape area. Furthermore, the distance from the centre of the draping rag to the outer edge of the rag was determined to identify the size of the drape waves and the number of drape waves on each image. Figure 2.12 illustrates an example of how the number of drape waves and the size of the waves were determined. The distance from the centre of the cylinder to

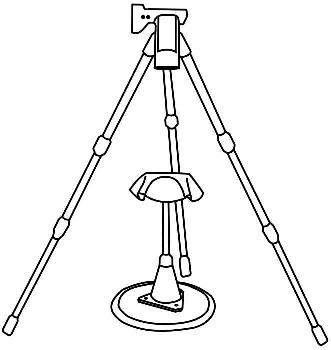

Drape Test Details	
Textile diameter	210 mm
Drape cylinder diameter	100 mm
Mean density	730 kg/m^3
Repetitions	50 (×6)

Fig. 2.10: Test stand for the drape test. The camera is placed directly over the rag and a hole in the centre of the rag and a pin in the centre of the cylinder helps placing the rag at the centre of the cylinder.

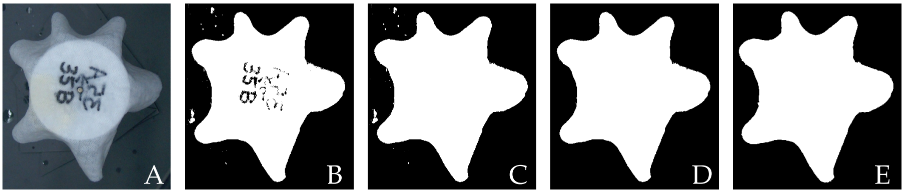

Fig. 2.11: Steps in the image processing. A) original grey scale image, B) grey scale image converted to binary image using a pixel intensity threshold, C) holes in the blobs in the binary image filled, D) blobs smaller than 2500 pixels removed, E) edge smoothed.

the edge of the rag as function of the angle presented in Figure 2.12 to the right, was determined by moving counter-clockwise 360 deg from the dashed line marked in Figure 2.12 to the left. The peaks in the plot were identified and used to determine the average number of peaks occurring when the rags were draping over the cylinder as well as the average size of the peaks.

The use of quantitative parameters to describe textile drape such as number of drape waves and their dimensions and the drape area has been reviewed by Kenkare and Plumlee (2005). This quantitative approach is opposed to investigations basing the comparison based on qualitative impressions of the drape (Breen et al., 1994; Ascough et al., 1996; Wu et al., 2002). Table 2.4 summarises the results of the drape test including parameters as drape area, drape wave size and number of drape waves. The quantitative description of the test results enables comparison with the corresponding simulation case for validation. The determined properties of area, thickness, breaking strength and elongation properties, lengths of bending rag samples and quantitative drape parameters such as drape area, mean size of the drape

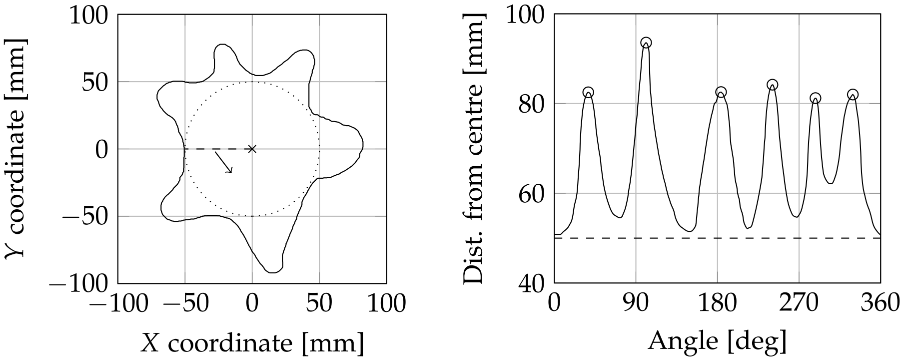

Fig. 2.12: Left: The border of the rag identified through image proscessing. Starting with the point marked in the figure to the left and moving counter-clockwise the distance from the centre of the disc to the border is determined. Right: Example of the distance from the centre of the disc as a function of the angle around the disc. Note that the peaks are identified.

Paramenter	Unit	Result
Mean drape area (A_s)	m^2	0.0148
Mean size of wave	m	0.0846
Maximum size of wave	m	0.102
Minimum size of wave	m	0.0663
Number of waves	-	6.40

Table 2.4: Results of the drape test.

Category	Material	Size [cm^2]
Dust cloth (rag)	PES	650.5
Baby wipes (BW)	Viskose, Poly-vinylchlorid, -acryl	308.6
	Viskose, Poly-ester, -acryl	294.0
	Viskose, Poly-propylen, -ethylen	277.2
	Viskose, Poly-propylen, -ethylen, -urethane	361.9
Toilet wipes (TW)	Cotton	207.8
	Cotton	221.6
	Viskose, Polyester	294.9
Cosmetic wipes (CoW)	Viskose, Poly-ester, -acryl	328.2
	Viskose, Poly-ester, -acryl	327.4
	Viskose, Poly-ester, -acryl	316.2

Table 2.5: Material, size and mass of wet wipes and the rag (Katscher, 2016).

waves and number of drape waves will be used to calibrate the discrete element textile model which is presented in the following chapter.

2.3 Applicability of the Rag in Artificial Wastewater

Katscher (2016) compared the properties of the used synthetic non-woven Aro super dust cloths to the properties of the wet wipes, which are often the cause of clogging in waste water pumps. These dust cloths are also referred to as rags in the present work. Different baby-, toilet-, and cosmetic wipes were selected and a variety of tests were done to determine the properties of each of the materials. The following properties were tested:

- dimensions: length, width and thickness
- mass
- material
- tensile force as function of material strain
- breaking strength

An overview of the wet wipes and the rag selected for investigation in the work by Katscher (2016) is presented in Table 2.5, along with the area of each piece of textile. As indicated in the table, the area of the rag is approximately double the area of the different toilet, cosmetic and baby wipes.

Figure 2.13 shows a comparison between the breaking strength and elongation properties of the wet wipes and the rag. The bars in the plot have been normalised with the result for the rag. TW, BW and CoW indicated in the bars are abbreviations for toilet wipes, baby wipes and cosmetic wipes respectively. Both figures show measurements for wet and dry textiles. It is clear from the figure that the breaking strength and elongation properties

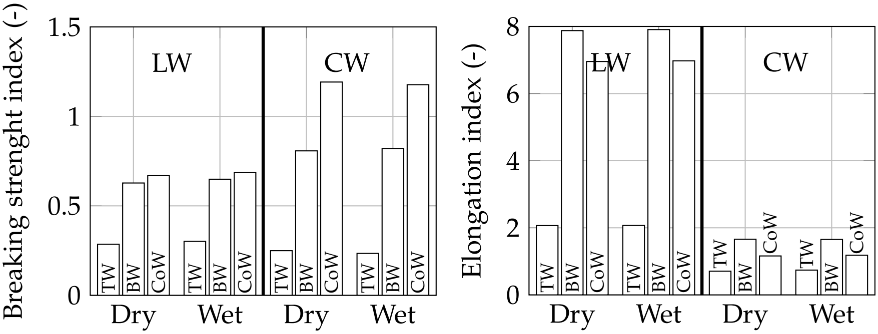

Fig. 2.13: Comparison of breaking strength and maximum strain of different wipes. The results are normalised with the corresponding results for the rags. TW: Toilet wipes, BW: Baby wipes, CoW: Cosmetic wipes. The figure is based on data from Katscher (2016).

are very similar for the two cases. This indicates that these materials are not easily degradable in the wastewater system.

Figure 2.13 to the left shows that the breaking strength of toilet wipes is around half of the breaking strength of the other types of wipes and around one fourth of the breaking strength of the rag. This makes the toilet wipes easier to handle in the wastewater system as they are more easily torn apart. The rag have a high tensile strength in the lengthwise direction compared to the rest of the materials and in the same order as the baby wipes and cosmetic wipes in the crosswise direction.

Figure 2.13 to the right, show the maximum strain before the materials break. Again, the values have been normalised with the results for the rag. It is clear how the strain before tearing of the rag is very limited compared to the different wipes. In the lengthwise direction, the elongation of the baby wipes and cosmetic wipes are 7-8 times higher than the rags. In the crosswise direction the elongation properties are in the same range.

Based on this comparison, the breaking strength of the rags most closely resembles baby wipes and cosmetic wipes. On the other hand, with respect to the elongation, the rags most closely resemble the toilet wipes. Similar to the properties of the wipes, it was found that the rags have different properties in the lengthwise and crosswise direction. These differences were however not as distinct as for the tested wipes. Noting the difference between the different types of wipes, it is difficult to choose a single material to represent all sanitary wipes causing clogging in wastewater pumps. The rags are easily accessible and and relatively high breaking strength of the rags can be an advantage during experiments as the rags will have a long lifetime. Moreover, as mentioned in Section 1.2, the rags are used in TU Berlin for clogging tests

(Gerlach et al., 2017) and in work to define a standard approach to evaluate the ability of wastewater pumps to handle materials such as rags and wet wipes (Pöhler et al., 2015). Therefore, despite the differences illustrated in Figure 2.13, the rags are also used in the present work as they are the closest to a standard piece of textile for clogging tests.

Chapter 3

Discrete Element Modelling of Textile

This chapter firstly gives an overview of the Discrete Element Method (DEM) with particle bonds. This is followed by a description of the arrangement of the particles to collectively form a rag and a description of the particle properties. Subsequently, a novel calibration approach to determine appropriate bond properties to model textile is presented and used to determine bond properties for the rag model based on the experimental results presented in Chapter 2. By implementing a modification to the 'updated bond model' in the commercial DEM software EDEM, good agreement between the experimental results from Chapter 2 and the rag model is obtained. The chapter is concluded with a summary of the calibration process and an overview of the determined bond properties.

3.1 The Discrete Element Method with Particle Bonds

The Discrete Element Method (DEM) can simulate the motion of a large number of particles. By connecting these particles with elastic bonds, they can collectively form a flexible surface representing a piece of textile. This application of the Discrete Element Method is far from the original use of the classical Discrete Element Method to simulate the motion of granular media. Therefore, an approach to calibrate the bond properties with realistic textile properties was developed based on the results of the textile tests presented in Chapter 2. Before the calibration is described, the following section gives a brief overview of the Discrete Element Method and the bond model used to connect the particles.

3.1.1 Overview of the Discrete Element Method

The Discrete Element Method (DEM) was first proposed by Cundall and Strack (1979), for simulation of granular media. The method uses Newtons 2nd law of motion to determine the motion of large numbers of particles as presented in (3.1)-(3.2) (Guo et al., 2013b).

$$m_{\mathrm{p}}\frac{\mathrm{d}^2\boldsymbol{x}_{\mathrm{p}}}{\mathrm{d}t^2} = \boldsymbol{F}_{\mathrm{b}} + \boldsymbol{F}_{\mathrm{c}} + \boldsymbol{F}_{\mathrm{f}} + \boldsymbol{F}_{\mathrm{g}} \tag{3.1}$$

$$J_{\mathrm{p}}\frac{\mathrm{d}^2\boldsymbol{\theta}_{p}}{\mathrm{d}t^2} = \boldsymbol{M}_{\mathrm{b}} + \boldsymbol{M}_{\mathrm{c}} \tag{3.2}$$

In these equations, m_{p} is the mass of the particle and $\boldsymbol{x}_{\mathrm{p}}$ is the translational displacement. The displacement of each of the particles is determined by a bond force $\boldsymbol{F}_{\mathrm{b}}$, a contact force due to collisions between particles which are not bonded $\boldsymbol{F}_{\mathrm{c}}$, a force due to gravity $\boldsymbol{F}_{\mathrm{g}}$, and a fluid force $\boldsymbol{F}_{\mathrm{f}}$ for simulations coupled to a fluid flow simulation. Furthermore, J_{p} is the moment of inertia and $\boldsymbol{\theta}$ is the angular displacement. The angular displacement is determined by a moment $\boldsymbol{M}_{\mathrm{b}}$ from the bond force $\boldsymbol{F}_{\mathrm{b}}$ and a moment $\boldsymbol{M}_{\mathrm{c}}$ from the contact force, $\boldsymbol{F}_{\mathrm{c}}$.

The contact force F_{c} between colliding DEM particles which are not bonded can be determined using the Hertz-Mindlin contact model, which is build-in in EDEM. The Hertz-Mindlin contact model is a soft sphere contact model allowing the particles to overlap slightly. The contact force is determined based on the overlap between the particles and the particle properties. Using the Hertz-Mindlin contact model, the normal contact force is determined using Equation (3.3) and the normal contact force with damping is determined using Equation (3.4).

$$\boldsymbol{F}_{\mathrm{n}} = \frac{4}{3}E^{*}\sqrt{R^{*}}\delta_{\mathrm{n}}^{\frac{3}{2}} \tag{3.3}$$

$$\boldsymbol{F}_{\mathrm{n}}^{\mathrm{d}} = -2\sqrt{\frac{5}{6}}\beta\sqrt{S_{\mathrm{n}}m^{*}}\boldsymbol{v}_{\mathrm{n}} \tag{3.4}$$

Where E^{*}, R^{*} and m^{*} are the equivalent Young's modulus, particle radius and mass respectively and δ_{n} is the normal particle overlap. Furthermore, $\boldsymbol{v}_{\mathrm{n}}$ is the relative velocity of the particles in the normal direction, the coefficient β accounts for kinetic energy dissipation through the coefficient of restitution is calculated using Equation (3.5) and the normal stiffness of the particles $S_{\mathrm{n,p}}$ is calculated using Equation (3.6).

$$\beta = \frac{\ln e}{\sqrt{\ln^2 e + \pi^2}} \tag{3.5}$$

$$S_{\mathrm{n,p}} = 2E^{*}\sqrt{R^{*}\delta_{\mathrm{n}}} \tag{3.6}$$

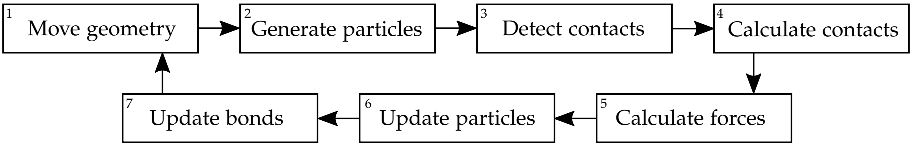

Fig. 3.1: Overview of one iteration in the commercial DEM software EDEM.

The tangential contact force is calculated using Equation (3.7) and the tangential contact force with damping is calculated using Equation (3.8).

$$\boldsymbol{F}_\mathrm{t} = -S_{\mathrm{t,p}}\delta_\mathrm{t} \tag{3.7}$$

$$\boldsymbol{F}_\mathrm{t}^\mathrm{d} = -2\sqrt{\frac{5}{6}}\beta\sqrt{S_{\mathrm{t,p}}m^*}\boldsymbol{v}_\mathrm{t} \tag{3.8}$$

Where $\boldsymbol{v}_\mathrm{t}$ is the tangential relative velocity of the particles, m^* is the equivalent mass, δ_t is the tangential overlap and $S_{\mathrm{t,p}}$ is the tangential stiffness as shown in Equation (3.9), where G^* is the equivalent shear modulus.

$$S_{\mathrm{t,p}} = 8G^*\sqrt{R^*\delta_\mathrm{n}} \tag{3.9}$$

Figure 3.1 illustrates the steps of an iteration in the commercial DEM software EDEM. The first step in an iteration is to move the geometry if a motion is prescribed. Then particles are generated. The third and fourth steps are to detect particle contacts and use the contact model to calculate the contact force. Afterwards, additional forces are determined, and the particles are updated based on the determined forces. Finally the bonds are updated and the iteration is over.

3.1.2 Modelling of Particle Bonds

A bond model is used to connect a number of discrete particles to form a flexible surface to represent the described rag. Potyondy and Cundall (2004) presented an incremental bonded particle model for rock, which is widely used. Guo et al. (2013b) used this bonded particle model for rock to model a flexible fibre and thoroughly validated tension, bending, torsion and vibrations of the fibre. Input parameters to this bond model include normal bond stiffness, tangential bond stiffness, critical normal stress, critical shear stress and bond radius. Normally, if two particles of same radius are bonded, the bond radius will be equal to the particle radius (Brown, 2013). Figure 3.2 illustrates two bonded particles, where the bond and particle radii are equal. Normal and tangential forces and moments act on the bond as sketched in the figure.

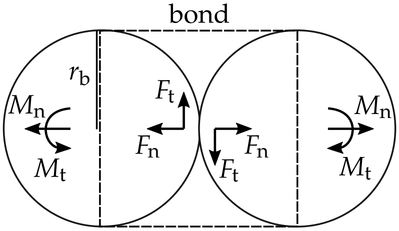

Fig. 3.2: Sketch of bond with normal and tangential force F_n and F_t and normal and tangential torque M_n and M_t.

Using the bond model by Potyondy and Cundall (2004), the incremental force on a bond is determined using Equation (3.10)-(3.13).

$$\mathrm{d}\boldsymbol{F}_\mathrm{n} = -\boldsymbol{v}_\mathrm{n} \cdot S_\mathrm{n} \cdot A_\mathrm{b} \cdot \mathrm{d}t \tag{3.10}$$

$$\mathrm{d}\boldsymbol{F}_\mathrm{t} = -\boldsymbol{v}_\mathrm{t} \cdot S_\mathrm{t} \cdot A_\mathrm{b} \cdot \mathrm{d}t \tag{3.11}$$

$$\mathrm{d}\boldsymbol{M}_\mathrm{n} = -\boldsymbol{\omega}_\mathrm{n} \cdot S_\mathrm{t} \cdot J \cdot \mathrm{d}t \tag{3.12}$$

$$\mathrm{d}\boldsymbol{M}_\mathrm{t} = -\boldsymbol{\omega}_\mathrm{t} \cdot S_\mathrm{n} \cdot I \cdot \mathrm{d}t \tag{3.13}$$

In the equations above, $\boldsymbol{v}_\mathrm{n}$ and $\boldsymbol{v}_\mathrm{t}$ are the relative velocities between two bonded particles in the normal and tangential direction, and $\boldsymbol{\omega}_\mathrm{n}$ and $\boldsymbol{\omega}_\mathrm{t}$ are the relative angular velocities in the normal and tangential direction. S_n and S_t denote stiffness per unit area of the bond in the normal and tangential direction and have the unit $\mathrm{N/m^3}$. Finally, $\mathrm{d}t$ is the time step, A_b is the cross-sectional area of the bond which is determined in Equation (3.14), J is the polar area moment of inertia determined in Equation (3.15) and I is the area moment of inertia determined using Equation (3.16).

$$A_\mathrm{b} = \pi \cdot r_\mathrm{b}^2 \tag{3.14}$$

$$J = \frac{1}{2} \cdot \pi \cdot r_\mathrm{b}^4 \tag{3.15}$$

$$I = \frac{J}{2} \tag{3.16}$$

Here r_b is the radius of the bond which is equal to the radius of the particles in the present work.

In each time step the total bond forces and moments are determined using Equation (3.17)-(3.20), where the incremental forces determined in Equations (3.10)-(3.13) are added to the total bond force.

$$\boldsymbol{F}_\mathrm{b,n} = \boldsymbol{F}_\mathrm{b,n} + \mathrm{d}\boldsymbol{F}_\mathrm{n} \tag{3.17}$$

$$\boldsymbol{F}_\mathrm{b,t} = \boldsymbol{F}_\mathrm{b,t} + \mathrm{d}\boldsymbol{F}_\mathrm{t} \tag{3.18}$$

$$\boldsymbol{M}_\mathrm{b,n} = \boldsymbol{M}_\mathrm{b,n} + \mathrm{d}\boldsymbol{M}_\mathrm{n} \tag{3.19}$$

$$\boldsymbol{M}_\mathrm{b,t} = \boldsymbol{M}_\mathrm{b,t} + \mathrm{d}\boldsymbol{M}_\mathrm{t} \tag{3.20}$$

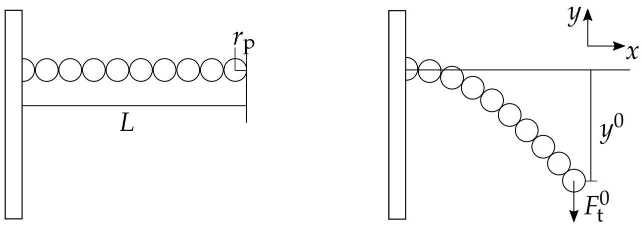

Fig. 3.3: Bending under load. The setup and definitions correspond to the case presented by Guo et al. (2013b).

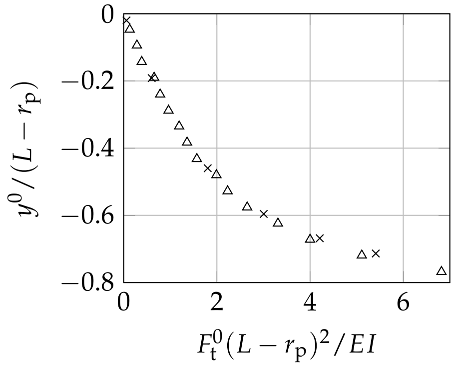

Fig. 3.4: Normalised deflection of the particle at the end of the fibre. × present work, △ Guo et al. (2013b).

3.1.3 Validation of the 'Updated Bond Model' in EDEM

Guo et al. (2013b) used the bonded particle model for rock by Potyondy and Cundall (2004) to model flexible fibres. They validated the results for bending with small and large deformation theory. In the work by Guo et al. (2013b) a force was applied to the outermost particle in one end of a fibre, while the other end was fixed and the rotation of the fixed particle was zero. The applied force was varied and the fibre deflection was recorded for different numbers of particles in the fibre. The simulation case is sketched in Figure 3.3.

The 'updated bond model' in EDEM is based on the same equations as used by Guo et al. (2013b) and the same case as presented by Guo et al. (2013b) is used for a series of simulations using EDEM for a case with 10 particles in the fibre. The result is shown in Figure 3.4. In the figure, F_t^0 is the force applied to the outermost particle, y^0 is the deflection L is the length of the fibre and r_p is the radius of the particles as sketched in Figure 3.3. As seen in Figure 3.4, the results in EDEM are very similar to the results presented by Guo et al. (2013b).

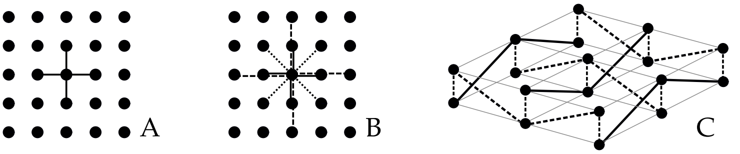

Fig. 3.5: Different configurations of discrete particles and connection between the particles. A) Breen et al. (1994) and Eberhardt et al. (1996), B) Provot (1995), where ——- marks structural springs, · · · · marks shear springs, and − − −− marks flexion springs C) Ballhause et al. (2008), where the yarn structure is imitated with the particle and spring configuration.

3.2 Particle- and Bond Arrangement to Represent Textile Material

The arrangement of the bonded particles used to collectively form the flexible rag must be determined before calibrating the particle and bond properties since the calibration will depend on the arrangement. Particle based models have been used for simulation of woven textiles where the grid lines have been parallel to the warp and weft direction of the textile (Sze and Liu, 2005; Breen et al., 1994; Eberhardt et al., 1996). Breen et al. (1994) developed a model for simulating the static draping behavior of a woven cloth based on a system of interacting point particles including experimentally obtained cloth properties. Breen et al. (1994) noted that ideally, each point in the particle model represents a thread crossing in a plain weave structure, and that representing the full detail of the weave structure with more particles is "*neither desirable nor computationally practical*". The structured in-line configuration of particles by Breen et al. (1994), where each particle is connected to four neighbouring particles except on the boundary of the textile, is sketched in Figure 3.5A. Eberhardt et al. (1996) used the methodology presented by Breen et al. (1994) as a basis for development of a dynamic cloth simulation, including a very simple drag model. However, in general the energy-based technique used by Breen et al. (1994) and Eberhardt et al. (1996) is most commonly used to produce static simulations while force based techniques are used in dynamic simulations in e.g. computer graphics techniques for modeling cloth (Ng and Grimsdale, 1996).

Provot (1995) used a force based technique were the connection between the particles consisted of structural springs to resist stretching stresses, shear springs to resist shearing stresses and flexion springs to resist bending stresses. The spring configuration used by Provot (1995) is sketched in Figure 3.5B. A more complex structure was adopted by Ballhause et al. (2008), who modelled fabric-reinforced membranes using discrete elements, imitating a weave structure as sketched in Figure 3.5.

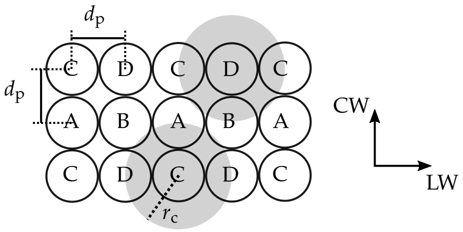

Fig. 3.6: In-line particle configuration with four particle types marked with A, B, C and D. The bonds C-D and A-B represent the lengthwise direction (LW) and the bonds A-C and B-D represent the crosswise direction (CW) of the modelled cloth.

In the present work the modelled textile is non-woven, but the simple orthogonal grid as sketched in Figure 3.5A, is maintained for simplicity and computational speed and a forced based technique using the Discrete Element Method is used to model the textile material. Accordingly, the textile surface is represented by an in-line network spherical particles as sketched in Figure 3.6. All particles have the same size and density and the distance between the particle centres corresponds to one particle diameter. As described in Chapter 2 the modelled rag has different properties in the lengthwise (LW) and crosswise (CW) direction (see definition in Figure 2.4). In order to implement this, four particle types are introduced. The four particle types have exactly the same properties, but enable the introduction of different bond properties between different types of particles. The four different particles are marked with A, B, C and D in Figure 3.6. Bonds between particles A-C and B-D represent textile properties in the crosswise direction while bonds between particles A-B and C-D represent textile properties in the lengthwise direction. No bonds can exist between particles A-D, B-C, A-A, B-B, C-C, D-D.

3.2.1 Determination of Contact Radius

The formation of bonds is controlled by a particle contact radius r_c marked with grey for a particle of type C and a particle of type D in Figure 3.6. If two particles are placed so their contact radii overlap at time zero, and if a bond between these two particles is defined (A-C, B-D, A-B and C-D), a bond is formed. The bond will break if a defined critical stress is exceeded or if the contact radii no longer overlap. The contact radius should be chosen so the critical stress is reached within a strain that does not break the overlap between the contact radii. For the described particle configuration sketched in Figure 3.6, the minimum contact radius to ensure that the contact radii overlap at the maximum strain of the modelled textile can be determined from Equation (3.21).

$$r_{\mathrm{c,min}} = r_{\mathrm{p}} + L_0 \cdot \epsilon \tag{3.21}$$

Where $r_{\mathrm{c,min}}$ is the minimum contact radius, r_{p} is the particle radius, ϵ is the maximum strain of the modelled textile before tearing and L_0 is the initial bond length, which is equal to the particle diameter in the present case where there is no space between the particles.

There is also a limit to the size of the contact radius since a too large contact radius will lead to overlapping contact radii of particles, which are not neighbours, leading to unwanted bond formation. Therefore, it must also be ensured that the contact radius is limited so that the contact radii of particles which should not be bonded do not overlap at time zero. This is exemplified in Figure 3.6, where a bond will be formed between the particles C and D if the contact radius is increased so the grey circles overlap. The maximum contact radius to avoid bond formation between particles which are not neighbours can be determined for the present particle arrangement by Equation (3.22).

$$r_{\mathrm{c,max}} = \sqrt{5} \cdot r_{\mathrm{p}} \tag{3.22}$$

With the particle arrangement sketched in Figure 3.6 and the maximum textile strain before tearing determined in Chapter 2 to be $\epsilon = 0.358$, the minimum ratio between the contact radius and the particle radius, determined using Equation 3.21 is 1.72. Similarly, based on Equation 3.22, the maximum ratio between $r_{\mathrm{c,max}}$ and r_{p}, avoiding overlapping contact radii and unwanted bond formation is $\sqrt{5}$. Therefore the contact radius should be in the range between 1.72 and $\sqrt{5}$. Based on this, a contact radius of $2.2 \times r_{\mathrm{p}}$ is used for the simulations. This allows strains up to $\epsilon = 0.73$.

3.2.2 Considerations on Discretization and Particle Properties

The choice of the size of the particles forming the rag is a trade-off between accuracy and computational requirements. Furthermore, considerations on the cell size versus the particle size in coupled simulations may set a limitation to the possible discretization of the textile.

Particle Density

When modelling a rag with a 2D network of 3D spherical particles, a change in the size of the particles forming the rag will also mean a change in the thickness of the rag surface. If the particle density is kept constant and set to the same as the density of the rag, this will mean that the total mass of

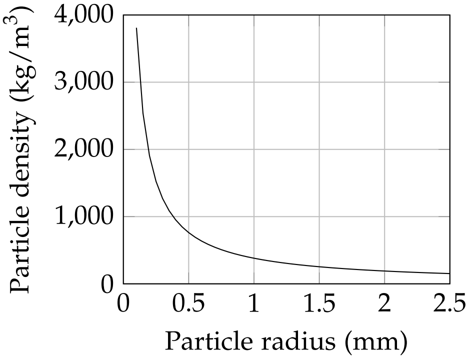

Fig. 3.7: Particle density as function of particle radius, for the case with constant mass per area.

the modelled rag will be different from the mass of the actual rag. Instead of using a constant particle density, the density can be scaled as the particle size is changed to ensure that the total mass of the modelled rag is equal to the mass of the actual rag. The mass per unit area of the rag samples used in the bending experiments described in Subsection 2.2.2 was approximately 0.42 kg/m^2. As an example, the required particle density to obtain the correct total mass per unit area as function of the particle radius is presented in Figure 3.7. As seen in the figure, to keep a constant mass of the modelled rag, the density of the particles decreases as the particle size increases. In coupled simulations taking into account fluid-particle interaction, a changed density will lead to a change in the conservative forces of buoyancy and gravity. However, these forces are not expected to have a dominant influence on the transport of rags in pumping systems and therefore they will be neglected in the coupled simulations. This is discussed further in Chapter 5.

Elastic Moduli

The particle stiffness, defined with the shear modulus G and Young's modulus E influences the time step of a DEM simulation. It is common to decrease the stiffness of particles in DEM simulations to be able to increase the simulation time step. Several authors, including Lommen et al. (2014) investigated the effect of particle stiffness on the behavior of bulk material. However, textile is a soft material compared to the materials commonly modelled using the Discrete Element Method, and therefore the Shear modulus of textile is already low. The shear modulus and Young's modulus are related as given in Equation (3.23), where ν is Poisson's ratio.

Paramenter	Unit	Value
Particle radius (r_p)	mm	0.5-2.5
$r_\mathrm{c}/r_\mathrm{p}$	-	2.2
Particle density	kg/m^3	215.2-1076
Shear modulus	MPa	1

Table 3.1: Properties of the particles forming the rag.

Particle-particle interaction	Unit	Value
Coefficient of restitution	-	0.01
Coefficient of static friction	-	0.5
Coefficient of rolling friction	-	0.01

Particle-geometry interaction	Unit	Value
Coefficient of restitution	-	0.01
Coefficient of static friction	-	0.5
Coefficient of rolling friction	-	0.01

Table 3.2: Particle-particle and particle-geometry interaction coefficients.

$$G = \frac{E}{(2 \cdot (1 + \nu))} \tag{3.23}$$

The properties of the particles representing the textile are summarised in Table 3.1.

Interaction Coefficients

Interactions between particles and between particles and geometry are defined through the coefficient of restitution, the coefficient of static friction and the coefficient of rolling friction. Table 3.2 presents the values used for these coefficients.

3.3 Calibration of Bond Properties

Parameter calibration of DEM models is often based on a trial and error approach where microscopical properties are changed until the expected macroscopic response is obtained (Wang and Guo, 2016). In classical DEM the macroscopic response could be the angle of repose of a pile of particles used to calibrate the rolling and sliding friction coefficients between the particles or simple drop tests to estimate the coefficient of restitution. Using the particle

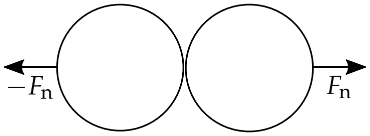

Fig. 3.8: Simulation of bond elongation. A force is applied to the two particles in opposite directions and the elongation is determined.

properties described in the previous section, the properties of the bonds connecting the particles are calibrated through simple simulations cases, each representing one of the standard textile tests described in Chapter 2. The bond model presented in Section 3.1.2 needs inputs of bond normal stiffness S_n and tangential stiffness S_t. As seen in Equations (3.10)-(3.13), the tangential bond stiffness S_t influences the tangential force $\boldsymbol{F}_\mathrm{t}$ and the twisting moment $\boldsymbol{M}_\mathrm{n}$, while the bond stiffness S_n influences both the force in the normal direction $\boldsymbol{F}_\mathrm{n}$ and the bending torque $\boldsymbol{M}_{\mathrm{t},}$. This means that S_n is responsible for both elongation and out of plane bending. However, Vidal-Salle and Boisse (2010) stated that there is no direct relation between tension and bending rigidity for textiles. Therefore, a new variable is introduced in the bond model to separate the tensile stiffness and the bending torque as it must be expected that the value of S_n modelling the right tensile properties will lead to an underestimation of the deflection of the fibre. The new variable $S_\mathrm{n,b}$ is calibrated to ensure agreement between the measured and simulated bending deflection and entails that Equation (3.13) in the existing bond model is replaced with Equation (3.24).

$$\mathrm{d}\boldsymbol{M}_\mathrm{t} = -\boldsymbol{\omega}_\mathrm{t} \cdot S_\mathrm{n,b} \cdot I \cdot \mathrm{d}t \tag{3.24}$$

The value of S_n to correctly model the elongation properties of the rag and determine an appropriate critical normal stress is determined in the following subsection based on the breaking strength and elongation test presented in Chapter 2. This is followed by the determination of appropriate values of $S_\mathrm{n,b}$ and S_t using the results of the bending and drape tests.

3.3.1 Normal Stiffness Based on Elongation Test Results

The normal bond stiffness S_n is calibrated using the results of the elongation test presented in Subsection 2.2.1. The elongation simulation is simplified to consist of two particles. A force of equal size but opposite direction is applied to the two particles to pull them apart. The simulation case is sketched in Figure 3.8.

The stiffness constant k_exp of the tested rags is determined using Eq. (3.25), where $F_\mathrm{max,exp}$ is the maximum force, measured immediately before the rags start tearing in the experiment, and $\Delta L_{\text{max,exp}}$ is the elongation in meters as the maximum force is applied.

$$k_{\text{exp}} = \frac{F_{\text{max,exp}}}{\Delta L_{\text{max,exp}}} \tag{3.25}$$

The strain at the maximum elongation is determined using Eq. 3.26, where $\Delta L_{\text{max,exp}}$ is the elongation and $L_{0,\text{exp}}$ is the initial length of the rag.

$$\epsilon_{\text{exp}} = \frac{\Delta L_{\text{max,exp}}}{L_{0,\text{exp}}} \tag{3.26}$$

Equation (3.27) is used to convert from the measured elongation $\Delta L_{\text{exp,max}}$ to elongation per bond in the bond model. $L_{0,\text{m}}$ is the initial length of the bond and $\epsilon_{\text{max,exp}}$ is the strain determined from (3.27).

$$\Delta L_{\text{m}} = \epsilon_{\text{max,exp}} \cdot L_{0,\text{m}} \tag{3.27}$$

The force applied per particle bond is found in Eq. 3.28, where n_{p} is the number of particles needed to cover the total length of the clamps holding the textile in the experiments (2 × 0.1 m).

$$F_{\text{m}} = \frac{F_{\text{max,exp}}}{n_{\text{p}}} \tag{3.28}$$

The stiffness of the bonds between the particles is calculated in Eq. (3.29), using the maximum elongation of the bonds, ΔL_{m} determined in Eq. (3.27).

$$k_{\text{m}} = \frac{F_{\text{m}}}{\Delta L_{\text{m}}} \tag{3.29}$$

The normal stiffness S_{n}, which is needed as an input to the bond model, has a unit of stiffness per unit area (N/m^3). This is calculated based on the stiffness constant of the bonds and the cross-sectional area of the bonds A_{b}.

$$S_{\text{n}} = \frac{k_{\text{m}}}{A_{\text{b}}} \tag{3.30}$$

The critical normal stress on the bonds before breakage under tension is determined in Eq. (3.31).

$$\sigma_{\text{c,n}} = \frac{\frac{F_{\text{max,exp}}}{n_{\text{p}}}}{A_{\text{b}}} \tag{3.31}$$

The normal stiffness per unit area S_{n} and the critical normal stiffness $\sigma_{\text{c,n}}$ depend on the bond radius. Figure 3.9 to the left shows S_{n} as function of the bond radius. It is seen how the normal stiffness per unit area decreases as the bond radius increases. Figure 3.9 to the right shows how the critical

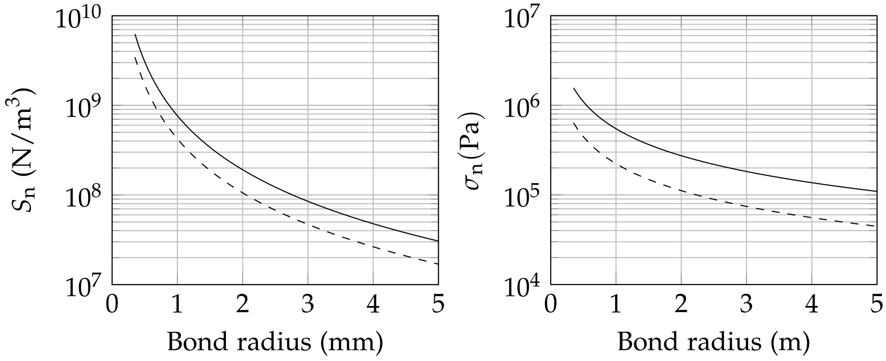

Fig. 3.9: Left: S_n as function of the bond radius. Right: critical normal stress as function of the bond radius. —— Lengthwise direction (LW), - - - - Crosswise direction (CW).

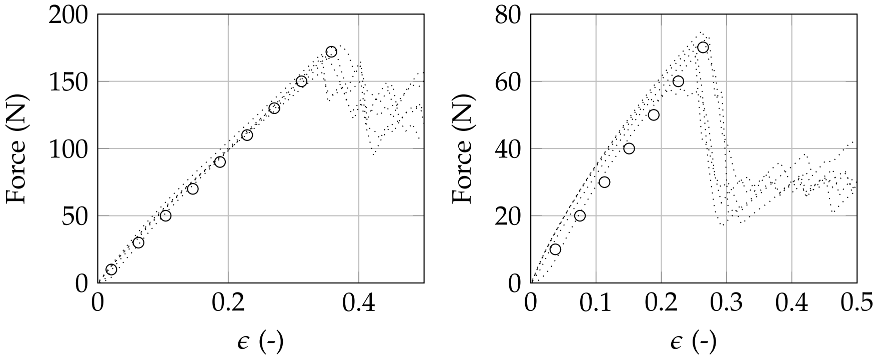

Fig. 3.10: Force as function of the textile elongation. · · · · measurements, ○ simulation.

normal stress also decreases with an increasing bond radius. In both figures, the dashed line represents the crosswise direction of the rag and the full line represents the lengthwise direction of the rag as defined in Figure 2.4.

The described simple case of two bonded particles was used validate the determined value of S_n. An increasing force was applied to the two particles and the resulting elongation was determined. The result is presented in Figure 3.9, which also shows the results from the experimental breaking strength and elongation test.

3.3.2 Bending Stiffness Based on Bending Test Results

The new variable of bending stiffness $S_{n,b}$ is calibrated based on a simplified simulation of the bending test presented in Chapter 2. The simulation case

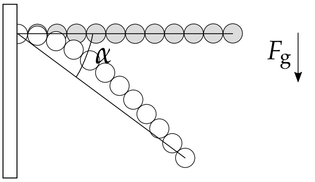

Fig. 3.11: Sketch of the simplified simulation of the bending test presented in Chapter 2. Bonded particles form a fibre and the bending stiffness $S_{n,b}$ of the bonds is calibrated so the outermost particle of the fibre reaches the line at an angle $\alpha = 41.3$ degrees from horizontal when gravity is acting on the particles.

is sketched in Figure 3.11. As illustrated in the figure, a fibre of bonded particles represents the bending rag sample in the simulation. Gravity acts on the fibre, and the deflection of the fibre depends on the bending stiffness $S_{n,b}$. The bending stiffness is calibrated so the outermost particle of the fibre will touch the sketched line at an angle $\alpha = 41.3$ degrees from horizontal. The length of the fibre and the mass per unit area were determined in the bending tests described in Subsection 2.2.2.

Figure 3.12 illustrates the method used to determine the bending stiffness $S_{n,b}$. Several simulations of a bending fibre was made using different values of $S_{n,b}$. For each simulation, the distance from the outermost particle in the fibre to the line at an angle α of 41.3 degrees from horizontal was determined. Figure 3.12 illustrates this distance as function of the stiffness $S_{n,b}$. An estimate of the right value of $S_{n,b}$ to model the bending deflection is found using linear interpolation between a point on each side of the line at 41.3 degrees. The points used for interpolation to determine a better estimate of $S_{n,b}$ are marked with $\times$ and connected with dotted lines. The point representing the final value of $S_{n,b}$ is marked with $\circ$.

The full lines in Figure 3.13 show the resulting deflection of a fibre representing the lengthwise direction (left) and a fibre representing the crosswise direction (right). The dashed lines in the figure represent the deflection of fibres using the original bond model where $S_{n,b} = S_n$. From the figure it is clear that the original bond model would underestimate the deflection of the rag sample.

3.3.3 Tangential Stiffness Based on Drape Test Results

A simulation of the drape experiment presented in Chapter 2 is made to determine the value of the last stiffness parameterm S_t. This parameter influences the tangential force and the twisting moment on the bonds and has no influence on the results of the elongation and bending simulations presented in the previous subsections.

In the drape simulations a circular arrangement of in-line particles repre-

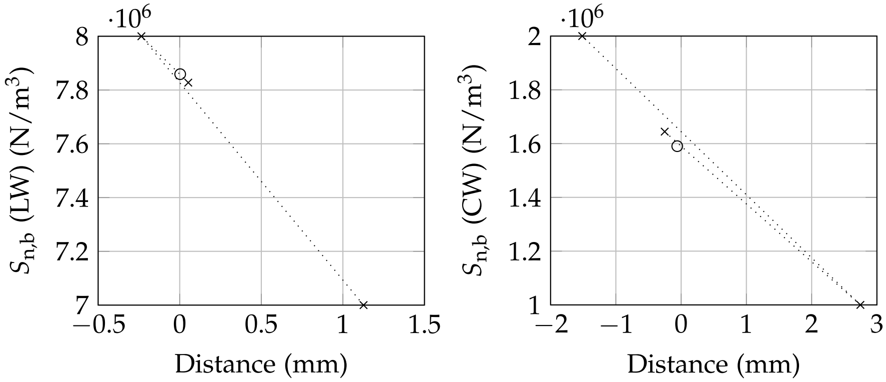

Fig. 3.12: Left: Results of bending simulations imitating the bending test of a sample in the lengthwise direction of the rag. Right: Results of bending simulations imitating the bending test of a sample in the crosswise direction of the rag. × results of initial bending simulations, · · · · line between interpolated points, ○ final calibrated value of $S_{\mathrm{n,b}}$.

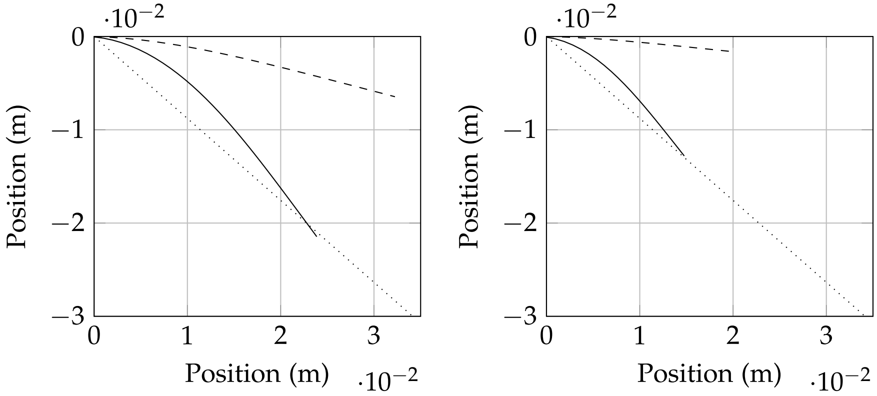

Fig. 3.13: Bending deflection of fibres of particles representing LW (left) and CW (right) strips of the rag. · · · · line declining 41.3 degrees, —— final deflection of the fibre using the calibrated value of $S_{\mathrm{n,b}}$, − − − final deflection of the fibre using the original bond model.

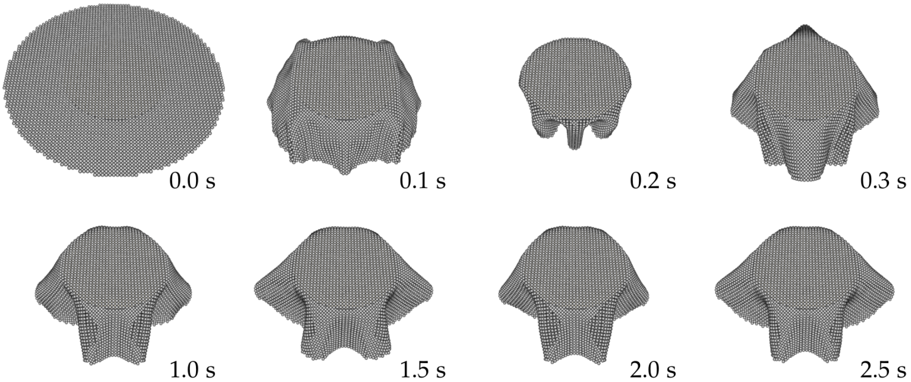

Fig. 3.14: Drape over time of a rag model with particles of radius 1.5 mm.

sent a round sample of the rag with a diameter of 0.210 m. This sample is placed directly on top of a cylinder with radius 0.05 m. Gravity is acting on the particles and the simulated textile sample will drape over the cylinder. An example of the a drape simulation is presented in Figure 3.14 for a particle radius of 1.5 mm. The initial condition of the circular rag sample is shown at time 0.0 s and the final drape is seen after 2.5 s. The density of the particles in the drape simulation is determined based on the densities of the samples used in the drape experiments. The mean density of the samples used in the experiments was 730 $\mathrm{kg/m^3}$ as seen in the table to the right in Figure 2.10, corresponding to a mass per unit area of approximately 0.56 $\mathrm{kg/m^2}$.

Figure 3.15 illustrates the contour of a simulated piece of textile with different values of the tangential bond stiffness, S_t. The figure shows results of simulations with a particle radius of 1.5 mm. The dashed circle is the mean size of the drape waves in the experimental investigation. The dotted circles are the minimum and maximum size of the drape waves recorded in the experiment. It is seen in the figure, that the size of the drape waves of the simulated textile is very similar to the mean size of the drape waves in the experiment. As the tangential bond stiffness S_t increases there is a tendency of the size of the drape waves to increase. Furthermore, the area of the draping textile seen from above increases with an increasing tangential bond stiffness S_t. This is illustrated in Figure 3.16, which shows the deviation in drape area and size of drape waves between the drape simulation using particles with a radius of 1.5 mm and the drape experiment. It is seen that at a tangential stiffness S_t of $1 \cdot 10^6$ $\mathrm{N/m^3}$, the drape area only deviates very slightly with 1.3% from the mean drape area observed in the experiment. At this tangential stiffness S_t the deviation in wave size is 2.1% and the textile forms 6 drape waves. The average number of drape waves formed by the rags during the drape experiment was 6.4. Therefore, the results of the drape simulation are

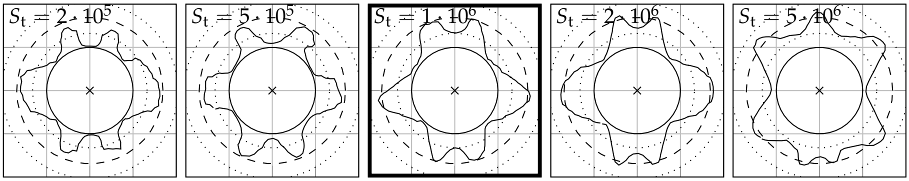

Fig. 3.15: Piece of textile draping over cylinder. The particles forming the piece of textile have a radius of 1.5 mm. The tangential bond stiffness, S_t, is varied from $5 \cdot 10^5$ N/m^3 to $5 \cdot 10^6$ N/m^3. The thick box marks the chosen value of the tangential bond stiffness.

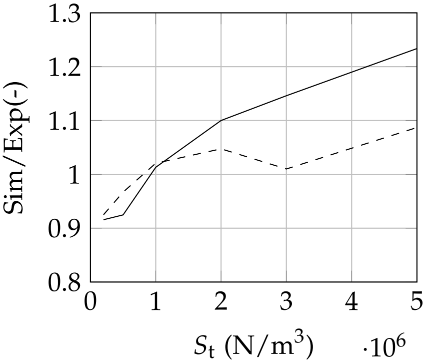

Fig. 3.16: Deviation between the size of the drape waves and the drape area found experimentally and by simulation with $r_p = 1.5$ mm as function of the value of the tangential bond stiffness. – – – size of drape waves, —— drape area.

satisfactory and it is shown that the DEM textile model is able to predict a static drape very close to experimental drape observations. Therefore a tangential stiffness of $S_t = 1 \cdot 10^6$ N/m^3 is chosen. To ensure that the presented results are independent of the size of the particles forming the rag and the time step size, an independence study of these parameters has been made. The results are presented in Appendix 1. This also includes considerations on damping coefficients.

The comparison between the drape experiment and the drape simulation shows that the macroscopic drape behaviour of the rag can be modelled using the described approach. The steps of the calibration of the rag model are summarised in the following.

3.4 Concluding Remarks on the Discrete Element Textile Model

An approach to model textiles, such as rags, using the Discrete Element Method has been presented.

Firstly, an appropriate arrangement of the particles forming the rag was determined. To enable the properties of the rag to be different in the lengthwise and crosswise direction, and to enable a larger particle contact radius without unwanted bond formation, four different particle types were introduced. The four particle types have the same properties, but enable different properties of the bonds connecting different types of particles.

Furthermore, a new variable was introduced to take into account the lack of correlation between the out of plane bending stiffness and normal stiffness in textile material. This variable is a bending stiffness affecting the bending moment in the bond model and has been termed $S_{\mathrm{n,b}}$.

Using the described arrangement of the particles forming the textile surface, a calibration approach to implement realistic textile properties was proposed. The approach uses experimental data on the elongation, bending and draping properties of the modelled rag.

3.4.1 Guidelines to Calibration of DEM Textile Models

An outline of the steps to setup and calibrate the presented DEM rag model are presented below. The model uses the 'updated bond model' in the commercial DEM software EDEM, which is based on the bond model presented by Potyondy and Cundall (2004).

1. Conduct elongation experiment for the lengthwise and crosswise direction of the rag to determine maximum strain before tearing and the force applied as the maximum strain is reached.
2. Conduct bending test for the lengthwise and crosswise direction of the rag and determine the length of the rag samples needed to reach the line at -41.3 degrees from horizontal.
3. Conduct draping test and determine the mean number of drape waves, the mean size of drape waves and the mean drape area.
4. Determine the normal stiffness per unit area and critical shear stress of the bonds for the lengthwise and crosswise direction using equation 3.25 and 3.31.
5. Calibrate the bending stiffness per unit area $S_{\mathrm{n,b}}$ by simulating the bending of a string of particles at different values of $S_{\mathrm{n,b}}$ and determining the distance from the outermost particle to the line at -41.3 degrees.

The value of $S_{\mathrm{n,b}}$ is modified to reduce the distance. An appropriate value of $S_{\mathrm{n,b}}$ can be determined by interpolating between results as illustrated in Figure 3.12.

6. Calibrate the tangential stiffness S_{t} through draping simulations.

After finishing these steps, the rag model is considered calibrated and ready to use in coupled flow simulations.

3.4.2 Overview of the Determined Bond Properties

The calibrated bond properties to model the described rag, which have been determined using the calibration method presented in this chapter, are listed below and will be used in the coupled simulations presented in Chapter 5. The properties for the lengthwise direction are listed in Table 3.3, and the properties for the crosswise direction are listed in Table 3.4. Note that both tables also show bond properties for rags formed by particles of radius 1 mm and 2 mm. The determination of these bond properties is described in Appendix 1.

Additionally, an overview of the number of particles needed to form the rag is given in Table 3.5 for particle radii of 1.0 mm, 1.5 mm and 2 mm.

r_p (mm)	ρ (kg/m^3)	$\sigma_{\mathrm{c,n}}$ (Pa)	S_{n} (N/m^3)	$S_{\mathrm{n,b}}$ (N/m^3)	S_{t} (N/m^3)
1.0	401.07	$5.47 \cdot 10^5$	$7.65 \cdot 10^8$	$3.86 \cdot 10^7$	$5 \cdot 10^6$
1.5	267.38	$3.65 \cdot 10^5$	$3.40 \cdot 10^8$	$7.86 \cdot 10^6$	$1 \cdot 10^6$
2.0	200.54	$2.74 \cdot 10^5$	$1.91 \cdot 10^8$	$3.15 \cdot 10^6$	$5 \cdot 10^5$

Table 3.3: LW model parameters. The density is the particle density used in the bending simulation.

r_p (mm)	ρ (kg/m^3)	$\sigma_{\mathrm{c,n}}$ (Pa)	S_{n} (N/m^3)	$S_{\mathrm{n,b}}$ (N/m^3)	S_{t} (N/m^3)
1.0	362.87	$2.23 \cdot 10^5$	$4.23 \cdot 10^8$	$1.03 \cdot 10^7$	$5 \cdot 10^6$
1.5	241.92	$1.49 \cdot 10^5$	$1.88 \cdot 10^8$	$1.59 \cdot 10^6$	$1 \cdot 10^6$
2.0	181.44	$1.12 \cdot 10^5$	$1.06 \cdot 10^8$	$4.05 \cdot 10^5$	$5 \cdot 10^5$

Table 3.4: CW model parameters. The density is the particle density used in the bending simulation.

Number of Particles			
particle radius (mm)	1.0	1.5	2.0
n_{p} (circular sample for drape sim., radius 105 mm)	8664	3852	2171
n_{p} (real size rag, 220 mm × 300 mm)	21008	9337	5252

Table 3.5: Number of particles constituting the rag surface at different particle radii.

Chapter 4

Experimental Investigation of the Transport of Rags in Pumping Systems

In this chapter the transport of rags in 1) the inlet pipe of a dry-installed pump, 2) the inlet of a submersible pump, and 3) the housing of a submersible pump is investigated experimentally. Visual access is enabled using perspex in parts of the test rigs. The chapter summarises work documented in Papers A, B and C.

4.1 Overview of Experiments

Experimental investigation of the motion of rags in pumping systems is accomplished in test rigs with major parts constructed in perspex to enable good visual access to the system. The rags are recorded with a fast digital camera in the inlet pipe of a dry-installed pump, in the impeller inlet of a submersible pump and inside the housing of a submersible pump. The results will enable validation of simulations of the motion of rags in wastewater pumps and provide appropriate initial conditions of the rags in these simulations.

The experiments were carried out in Department of Energy Technology in Aalborg University (AAU) and in the Department of Fluid System Dynamics in Technische Universität Berlin (TU Berlin), where a wet pit with two submersible pumps as well as a pumping station for dry installed pumps in scale 1:3 are located. Figure 4.1 presents simplified sketches of the three test rigs used in the experiments. Figure 4.1A shows a part of a scaled pumping station for a dry installed pump, Figure 4.1B shows a wet pit with a submersible pump and Figure 4.1C shows a test rig with a glass aquarium used as pump

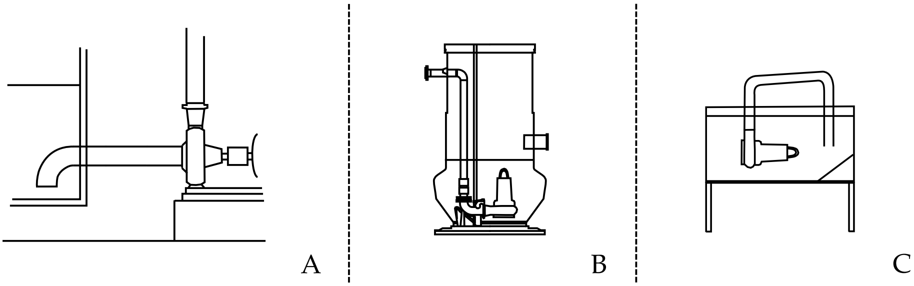

Fig. 4.1: A) Dry-installed pump in scaled pumping station with major parts constructed in perspex, B) Submersible pump in wet pit with modified bottom in perspex, C) Submersible pump with perspex housing placed in fully transparent aquarium. The transport of rags in the test rigs is captured with a fast digital camera.

sump for a submersible pump with a transparent housing, enabling full visual access into the housing. The experiments have been documented in Paper A, Paper B and Paper C, as well as in Jensen et al. (2017) and Sørensen and Jensen (2017).

For all experiments, artificial wastewater is created using clean water containing the rags presented and characterised in Chapter 2. To ensure that the rags are saturated with water, they are left in water for 24 hours prior to the experiments. Recall that the experiments to characterise the properties of the rags were also done using rags that had been in water for 24 hours.

The results of each experiment are obtained by image processing of the images captured with the fast digital camera. During the image processing the rags are identified in the images and properties such as position of the centroid, covered area and elongation ratio are extracted for further analysis. The steps used in the image processing are similar for the experiments in the three test rigs and are presented below.

4.2 Image Processing

The image processing steps to extract and analyse results from the acquired images are similar for the investigations in each of the three test rigs presented in paper A, B and C. Only the choice of threshold and the extracted properties deviate. The five main steps of the image processing are listed below and will be described in the following.

1. Determine average background
2. Background subtraction
3. Conversion to binary image using an intensity threshold
4. Deletion of small blobs using a size threshold
5. Extract properties of the remaining blob

The first step of the image processing is determination of an average background. The average background is found by briefly capturing images before each experiment is initiated and calculating an average pixel intensity for each pixel. This results in an image of the average background, which can be subtracted from images captured during the tests. This subtraction makes the rag more easily distinguishable from the background. All acquired images are grey scale images with pixel intensities in the range 0-255. Figure 4.2 illustrates how the pixel intensity values in an image change when the average background is subtracted. As seen in the figure, the average background mainly contains pixels with intensities of less than 40, the original image before background subtraction contains pixels with intensities up to around 100, with most pixels having an intensity of around 65. In the resulting image after background subtraction, there is a very low amount of pixels with intensities in the range from 10-30 and the background mainly consists of pixels with an intensity close to zero. The rag in this case consists of pixels with intensities between 30-80. The image used in Figure 4.2 was acquired in connection with the experiments with the test rig with the dry-installed pump.

After background subtraction the images are converted from grey scale to binary images using an intensity threshold value. An appropriate threshold value is determined based on an analysis of the change in identified rag area as function of the threshold value. Different threshold values were used for each test. This is due to a variation of the amount of daylight in the laboratory where the experiments were conducted, as well as different amounts of air bubbles in the water depending on the operating point.

When the grey scale images are converted to binary images, small blobs may appear apart from the main blob representing the rag. These small blobs are results of reflection of light in the perspex, air bubbles or small pieces of rags in the flow. They are removed using a size filter removing all objects with an area smaller than a specified size threshold.

After the described steps only a blob representing the rag is present on the final binary image, and parameters to characterise this blob can be extracted. The parameters used to characterise the rags depend on the experiment (A, B or C in Figure 4.1) and include elongation ratio, orientation, area and position. The parameters used for the experiment focusing on rags in the suction pipe to a dry-installed pump (Figure 4.1A), are sketched in Figure 4.3.

The following three sections describe the experiments in each of the three test rigs sketched in Figure 4.1. Examples of the image processing in each of the three experiments are presented in Figure 4.6, 4.8 and 4.11 in these sections.

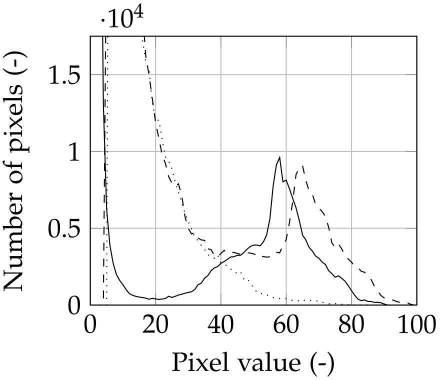

Fig. 4.2: Pixel values before and after background subtraction. – – – original image, · · · · average background, ——- resulting image.

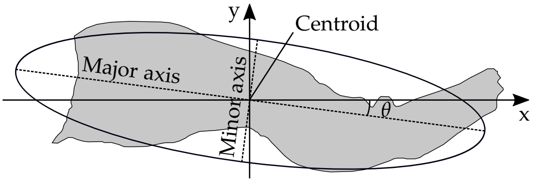

Fig. 4.3: Parameters used to characterise the rags.

Camera Settings		
Area of interest	AOI1	AOI2
Camera	Basler acA1300-30um	Basler acA1920-155um
Lens	Navitar 24 mm	Nikon Nikkor 50 mm 1:1.4
Image size [mm]	850 mm × 635 mm	520 × 225 mm
Resolution	1280 × 960 pixel	1920 × 832 pixel
Frame Rate	30 fps	150 fps
Exposure time	4000 µs	1500 µs

Table 4.1: Settings of the cameras synchronously recording AOI1 and AOI2.

4.3 Characterisation of the Shape and Position of Rags Upstream of a Dry-installed Wastewater Pump

As sketched in Figure 4.1, wastewater enters dry-installed pumps through a suction pipe. This entails that the rags entering the pump can only come from a direction directly in front of the pump impeller. Detailed investigations of the characteristics of the rags as they move through the inlet pipe are needed to provide realistic initial conditions for clogging simulations and can additionally form a validation case for coupled simulations. Parts of this analysis have been documented in Paper C, *Characterisation of Textile Shape and Position Upstream of a Wastewater Pump under Different Part Load Conditions*.

4.3.1 Experimental Setup

A scaled pumping station, with major parts constructed in perspex, is located in Department of Fluid System Dynamics in TU Berlin. This test rig is sketched in Figure 4.4. In the figure, A) marks the pump sump, B) is the suction pipe, C) is the pump, D) is the outlet of the pump, E) is a throttling valve used to control the operating point and F) is a box from where the water and rags flow back into the pump sump. The volume flow in the system is limited by the size of this box, which will overflow at flow rates through the system of around 600 m^3/h and higher. The rags were recorded at two areas of interest. These are marked with AOI1 and AOI2 in the simplified sketch to the right in Figure 4.4. AOI1 covers the pump sump at the inlet to the suction pipe and AOI2 covers 0.5 m of the suction pipe 0.5 m upstream of the pump, corresponding to 2.5-5.0 suction pipe diameters from the impeller inlet. The two areas of interst, AOI1 and AOI2, were recorded with two synchronised fast digital cameras to capture the motion of the rags. The camera specifications are given in Table 4.1.

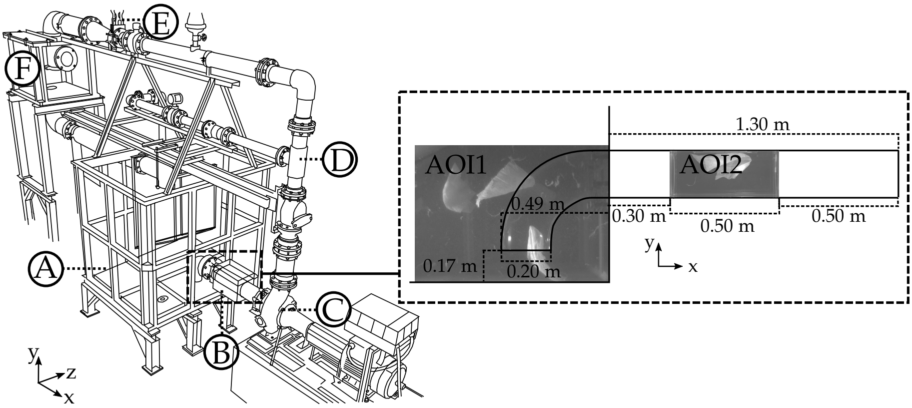

Fig. 4.4: Scaled pumping station (1:3). A) pump sump, B) suction pipe, C) pump, D) outlet pipe, E) throttling valve and F) box. This sketch is based on a sketch presented in Jensen et al. (2017). The areas of interests AOI1 and AOI2 are marked in the magnified part to the right, which is based on a sketch first presented in Paper E.

	50% of BEP	75% of BEP	100% of BEP
800 RPM	286	196	207
985 RPM	265	116	241
1200 RPM	337	241	234

Table 4.2: Number of recorded rags at each operating point. In total 2123 rags were recorded as they moved through the inlet pipe.

Since the flow rate was limited by the size of the box marked with F) in Figure 4.4, the pump was not operated at the nominal rotational speed of the impeller of 1475 RPM. Instead the experiments were done at impeller speeds of 800 RPM, 985 RPM and 1200 RPM. Furthermore, the experiments were made at the best efficiency point (100% Q_{BEP}), part load (75% Q_{BEP}) and heavy part load (50% Q_{BEP}) for each rotational speed of the impeller. The operating point was controlled using the valve marked with E) in Figure 4.4. The mentioned variations result in 9 different operating points. For each operating point 5-8 tests were made to ensure that a high number of rags had been recorded at the areas of interest. Table 4.2 shows the number of rags recorded at each of the tested operating points.

For each experiment, 20 new rags were added to the pump sump and the experiment was run until the pump operating point changed due to clogging or, if the pump did not clog, until the appearance of the rags changed as they got worn by repeatedly passing through the system. When an experiment was over, the rags were removed from the system and 20 new rags were added for the next experiment. Figure 4.5 shows QH curves of the pump

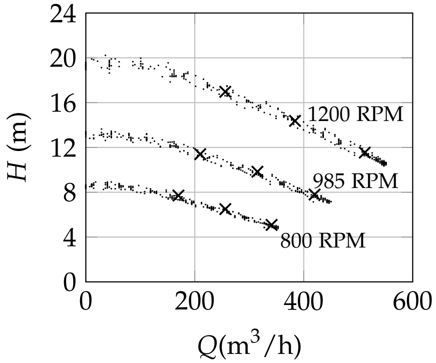

Fig. 4.5: QH-curves of the tested pump. · measured points, × operating points chosen for the experiments.

at the three rotational speeds of the impeller. In the figure, the dots mark measured points and the crosses mark the operating points chosen for the experiments.

An example of image processing of the acquired images is presented in Figure 4.6. The steps of the image processing presented in this figure correspond to step 2-4 presented in Section 4.2. After image processing, properties of elongation ratio, area, position and orientation of the remaining blob were extracted and analysed.

4.3.2 Discussion of the Results

Results of the analysis of the properties of elongation ratio, orientation, 2D area as well as the distribution of rags in the suction pipe were presented in Paper A. In the paper, the properties were compared for the nine tested operating points. The results showed that the most probable position of the rags was around the centre of the suction pipe, with a slight shift below the horizontal centreline. The maximum elongation ratio of the rags was observed when they were located at the centre of the pipe. Furthermore, the maximum area was observed when the rag was located close to the centre of the pipe. Finally, there was a tendency of the rags in the bottom part of the pipe to have an orientation of up to 12 degrees (counter-clockwise from horizontal as defined in Figure 4.3). Rags in the upper part of the suction pipe were more closely aligned with the main flow direction. The described characteristics of the rags are plotted in Figure A.5 in Paper A. Interestingly, the 2D area was the only property that changed with the operating point.

The cameras were placed on the side of the test rig capturing the images of the rags from this side only. This meant that a 2D representation of the rags was obtained rather than the full 3D description. Since the system is not

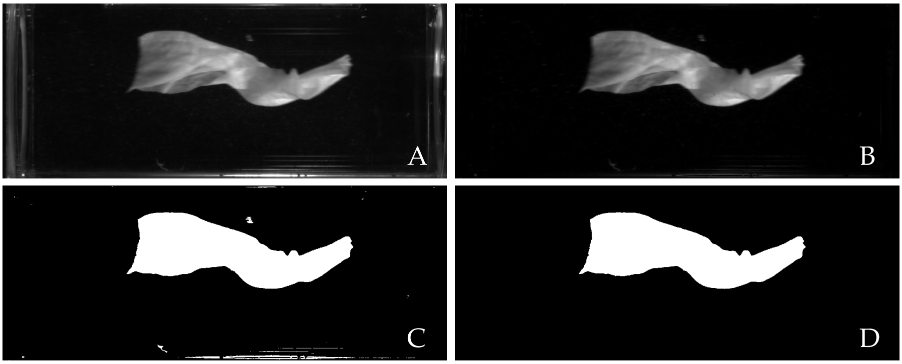

Fig. 4.6: Example of image processing of the images captured in the test rig with a dry installed pump (AOI2 in Figure 4.4). A-B) Background subtraction, B-C) conversion to binary image using intensity threshold, C-D) removal of small blobs using a size filter.

symmetric, a simplifying assumption of a symmetric shape of the rags is not appropriate, and a description of the 3D shape of the rags in the inlet pipe is not possible on the basis of the current data. Therefore a conclusion on the change in area contains uncertainties on how the change in the 2D area affects the 3D shape of the rags. Additionally, geometry changes of the suction pipe and bend as well as the pump are likely to affect the characteristics of the rags. This forms another uncertainty since only the presented configuration of the test rig has been tested and the influence of the geometry is unknown.

Based on the presented results, the lack of change of the characterised properties with the operating point suggests that different types of clogging occurring at different operating points are mainly due to a change in flow conditions inside the pump. This brings valuable information on the initial conditions of rags for clogging simulations as they can mainly remain the same at different operating points. The described characteristics of area, elongation ratio, orientation and position in the pipe (see Figure A.5 in Paper A) can be used to define the initial conditions of rags in simulations of rag transport through wastewater pumps.

The results motivate a study on the motion of rags as they reach the impeller and the motion of the rags inside the pump housing to identify differences in the motion characteristics of the rags at different operating points. This is investigated using test rigs B and C sketched in Figure 4.1. The results are summarised in the two following sections, to form a basis for validation of clogging simulations.

4.4 The Motion of Rags in the Inlet to a Submersible Pump

Submersible pumps are placed directly in a pump sump with the impeller inlet near the bottom as sketched in Figure 4.1B. Therefore, the sanitary objects causing clogging can enter the inlet of the pump from the all directions around the impeller inlet.

The study of the motion of the rags in the inlet pipe to a dry-installed pump, described in the previous section, did not have visual access to the pump itself. The very limited change in rag transport characteristics from operating point to operating point motivates a study in a test rig where the motion of the rags entering the pump impeller can be observed. The motion of rags at the impeller inlet is recorded and analysed to identify differences from operating point to operating point and to form a basis for validation of simulations of rags entering the pump impeller. A preliminary analysis of the rags entering the impeller in this setup was presented in Paper C, *Experimental Investigation of the Motion and Shape of Flexible Objects near a Pump Inlet*.

4.4.1 Experimental Setup

A modified wet pit with a bottom made of perspex is located in the Department of Fluid System Dynamics in TU Berlin. A sketch of the test rig is presented in Figure 4.7. As sketched in the figure, a fast digital camera was placed under the wet pit. The camera captured the motion of rags as they entered the impeller of the submersible pump. The pump had an inlet diameter of 150 mm and the impeller was a single channel impeller for wastewater applications. The camera had a frame rate of 160 fps with an exposure time of 1000 µs. The rotational speed of the pump impeller was the nominal 1445 RPM. This resulted in a rotational movement of the impeller of approximately 50 degrees between two images and a movement of around 8 degrees during the exposure time for a image. To create artificial wastewater with a high degree of contamination, 175 wet rags were added to the water in the wet pit for each test. The motion of the rags was recorded at 4 different operating points. These were 60%, 80% 100% and 120% of the Q_{BEP}. An example of an image acquired during the experiment is given in Figure 4.8A. As seen in the image, only the impeller inlet is captured. Figure 4.8A-D also presents an example of the image processing of the acquired images. The steps of the image processing presented in this figure correspond to step 2-4 described in Section 4.2.

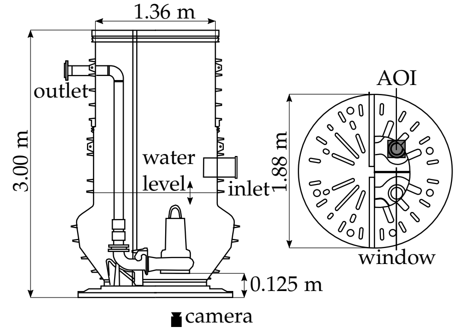

Camera Settings	
Camera	Basler acA1920-155um
Lens	Nikon Nikkor 50 mm 1:1.4
AOI	150 × 150 mm
Resolution	1216 × 1216 pixel
Frame rate	160 fps
Exposure time	1000 µs

Fig. 4.7: Left: Sketch of the wet pit test rig where a part of the bottom is replaced by perspex. A fast digital camera is placed under the wet pit and the AOI captured by the camera is marked on the sketch to the right. This sketch was originally presented in Paper C. Right: Table of the camera setting used during the test.

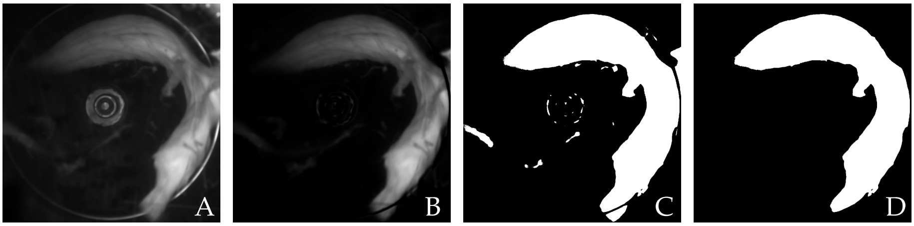

Fig. 4.8: Example of image processing of the images captured in the test rig sketched in Figure 4.7. A-B) Background subtraction, B-C) conversion to binary image using intensity threshold, C-D) removal of small blobs using a size filter.

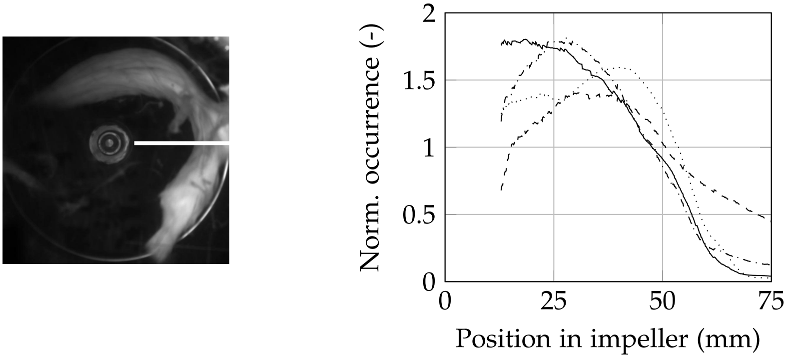

Fig. 4.9: Distribution of rags in the inlet to the impeller. $x = 0$ is the centre of the impeller. – – – 60% of Q_{BEP}, – · –· 80% of Q_{BEP}, —— 100% of Q_{BEP}, · · · · 120% of Q_{BEP}.

4.4.2 Discussion of the Results

During the experiments, there was a clear tendency of the rags to get stuck on the impeller leading edge. By sorting the acquired images and using the images containing only one rag at the time, Paper C described different types of movements of the rags as they entered the impeller inlet, getting stuck on the impeller leading edge. These observations correspond well to the observations by McEvoy (2011), who observed impeller leading edge blockage and impeller eye blockage, and to Connolly (2017), who particularly investigated leading edge blockage as it was identified as the most commonly occurring type of blockage.

Additionally, all the acquired images ($1.2 \cdot 10^6$ images, corresponding to 2 hours of recording), including images of several rags in the impeller, were processed as illustrated in Figure 4.8 to further investigate where in the inlet the rags were accumulating. The result is presented in Figure 4.9 to the right. The figure shows the distribution of rags in the impeller inlet at the four tested operating points. The data is extracted from the white line marked in Figure 4.9 to the left. For every image where a rag covers the line, the pixels covered by the rag are registered and a sum of all occurrences of rags on the line is computed. Finally, the result at each operating point is normalised with the mean value of the occurrences of rags along the line at each of the operating points. It is observed in the figure that the rags tend to stay around the centre of the impeller when the pump is operated at the best efficiency point. At part load and over load the rags tend to be between 25 mm and 50 mm from the centre. Additionally, at heavy part load at 60% of Q_{BEP}, the rags are more evenly distributed along the line than at operating points closer to the best efficiency point. This is in agreement with observations during the experiment noting that the rags did not accumulate in the impeller at this operating point. However, 60% of Q_{BEP} was the only operating point where the experiment had to be terminated due to clogging. When disassembling the pump it was clear that rags had accumulated at the tongue, blocking the outlet of the pump. The clear change from operating point to operating point was not found when observing the rags in the suction pipe to a dry installed pump, and this suggests that flow conditions inside the pump are the main factor influencing the risk of clogging.

When the rags accumulated in the impeller inlet, the pump efficiency was severely affected. Surprisingly, it was repeatedly observed that the rags would suddenly disappear from the impeller inlet. As rags accumulated at the inlet to the impeller the volume flow would decrease and the power consumption would increase to a point where the pump was close to breakdown. However, at one point the rags would leave the impeller inlet and the pump would immediately return to normal operation. This ability of self-cleaning meant that no clogging events led to breakdown of the pump during test of the operating points 80 %, 100 %, and 120 % of Q_{BEP}, even though the test was run with highly contaminated artificial wastewater in the form of 175 rags/test.

The visual access in the described experiments was limited to directly at the impeller inlet, and consequently the motion of the rag inside the pump housing could not be observed. To enable investigation of what happens when rags enter the pump housing causing blockages by accumulating at the tongue, a pump casing was constructed in perspex.

4.5 The Motion of Rags through Impeller and Housing of a Submersible Pump

A transparent housing for a submersible centrifugal pump with a single channel impeller was constructed to enable visual access to the motion of rags inside the casing (Bjerg et al., 2016). Several experiments have been made with one rag at the time, to analyse the motion of the rags through the pump. The results will form a good basis for validation of coupled simulations of rag transport through wastewater pumps. The experiments are also presented by Sørensen and Jensen (2017) and in Paper B.

4.5.1 Experimental Setup

The test rig with a pump with a transparent casing is sketched in Figure 4.10. It differs from the traditional wet pit (Section 4.4), as the pump is placed horizontally in the setup. The experiments were conducted at a rotational speed of the impeller of 1200 RPM at five different volume flows resulting

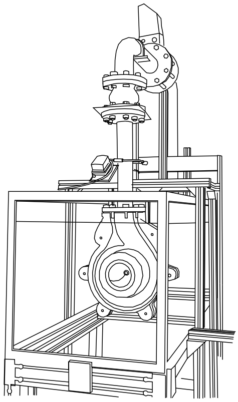

Camera Settings	
Camera	Basler acA1920-155 µm
Lens	Cosmicar/Pentax TV lens 25 mm
AOI	0.21 m × 0.27 m
Resolution (FOV)	1044 × 1344
Frame rate	100 fps
Exposure time	350 µs

Fig. 4.10: Left: Sketch of the test rig with a submersible pump with a transparent casing placed in an aquarium. Right: Table of camera settings during the experiment.

in five operating points ranging from 55% to 90% of Q_{BEP}. The pump had an inlet diameter of 100 mm, an outlet diameter of 80 mm, and a specific speed of 81. The volume flow and head at the best efficiency point at 1200 RPM was 26.8 m^3/h and 5.6 m respectively. The impeller was an asymmetric single channel impeller for wastewater applications.

The aquarium was 1.95 m × 0.56 m × 0.58 m. A plate was placed 125 mm from the inlet of the impeller to ensure inlet conditions similar to those in a traditional wet pit. The experiments were made with one rag at the time based on the expectation that if a rag is observed to stay in the pump casing following the flow or to get stuck on the tongue, the risk of accumulations of rags inside the pump is higher. The tests were repeated 50 times for each operating point. As the rag would not leave the pump in all cases, a test would be terminated if the rag had been stuck in the same way for 30 s, or if the rag had been in the pump for 60 s.

A fast digital camera was used to capture the motion of the rags through the pump. The camera settings are listed in the table to the right in Figure 4.10. Figure 4.11A shows an example of an image of the area of interest where a rag is stuck on the tongue of the pump. Additionally, Figure 4.11A-D illustrates the image processing used to isolate the rag in the images acquired during the experiment. The illustrated steps correspond to step 2-4 presented in Section 4.2.

4.5.2 Discussion of the Results

Three types of motion of the rags were observed during the experiments. These were 1) the rag got stuck on the tongue, 2) the rag recirculated in the volute and 3) the rag exited the pump as it reached the outlet. Examples

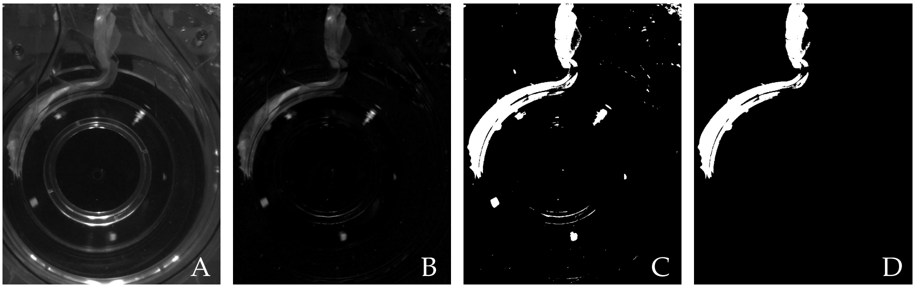

Fig. 4.11: Example of image processing of the images of rags inside the transparent pump housing. A-B) Background subtraction, B-C) conversion to binary image using intensity threshold, C-D) removal of small blobs using a size filter.

of the three cases are presented in Figure 4.12, 4.13 and 4.14. Figure 4.12 shows an example of a rag moving into the pump impeller, through the volute and in the end getting stuck on the tongue as it reaches the outlet. Figure 4.13 shows an example of a rag that recirculates in the volute. As the rag reaches the outlet it passes the tongue and moves back into the volute. Finally, Figure 4.14 illustrates how a rag enters the pump impeller and exits the pump as it reaches the outlet. Unexpectedly, there was no occurrences of the rag getting stuck in the impeller inlet edge as observed in the experiment described in Section 4.4 and described in the studies by McEvoy (2011) and Connolly (2017).

Paper B, describes how image analysis was used to determine the motion of the rag throughout the casing. The images where sorted into the three cases presented in Figure 4.12, 4.13 and 4.14. For each case the mean distance from the centre of the impeller to the centre of mass of the blob representing the rag as function of the angular position was determined for the motion of the rag through the pump. It was shown that a difference between the three cases is most distinct at angular positions of the centroid of the rags of 100 degrees or less before the tongue of the pump (see definition in Figure B.2). Moreover, using image analysis, the number of occurrences of each of the events was determined. The mean number of re-circulations in the volute as function of the operating point is presented in Figure 4.15. Note that re-circulation and the rag getting stuck on the tongue can occur several times per test. As seen in the figure a tendency of the rags to stay inside the pump was mainly observed at part load conditions of less than 70% of Q_{BEP}. At 60% of Q_{BEP} the mean number of recirculations was 5, while it was 111 at 55% of Q_{BEP}. The figure also shows the number of occurrences of the rags getting stuck on the tongue for one second or more. In heavy part load conditions, the rag would be stuck on the tongue for one second or more in almost all tests with a mean of 0.82 occurrences per test. Finally, the percentage of times

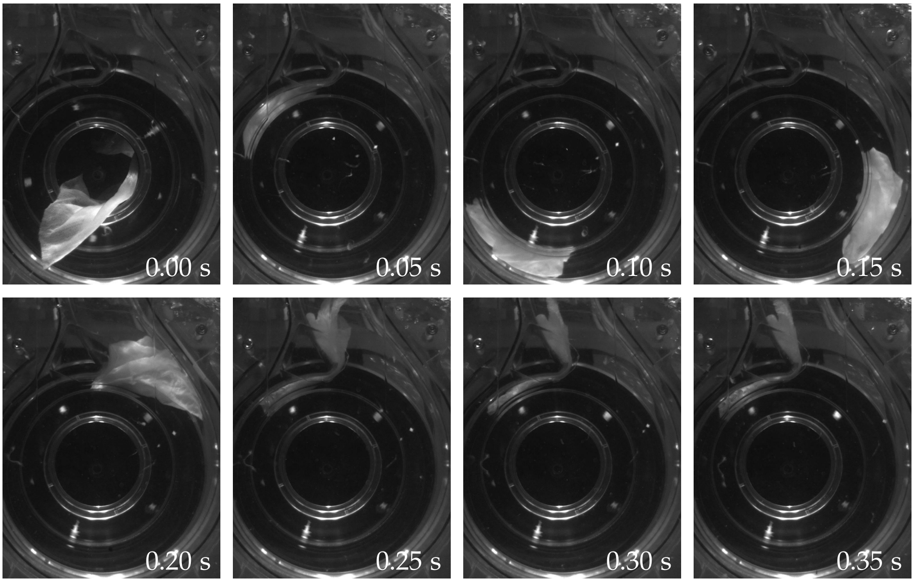

Fig. 4.12: Image sequence showing an example of a rag getting stuck on the tongue.

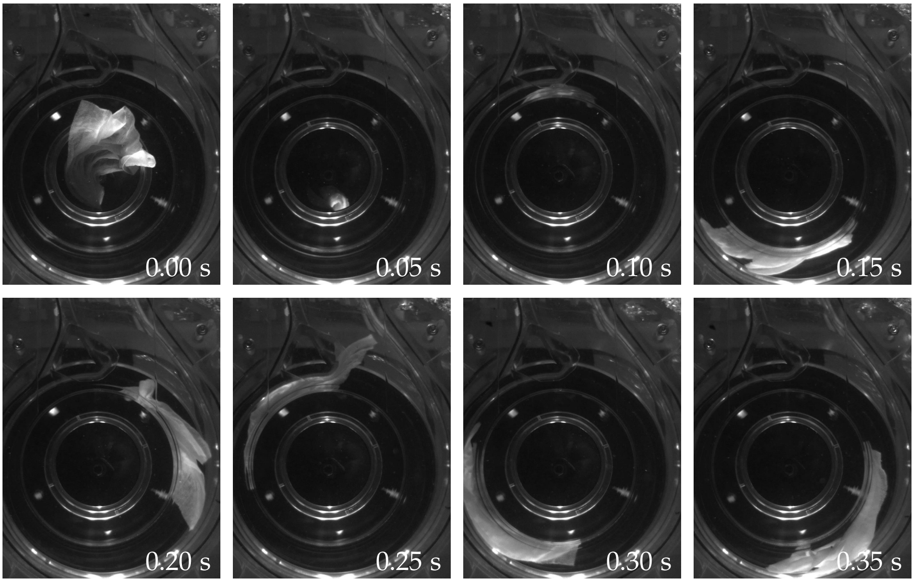

Fig. 4.13: Image sequence showing an example of a rag recirculating in the volute.

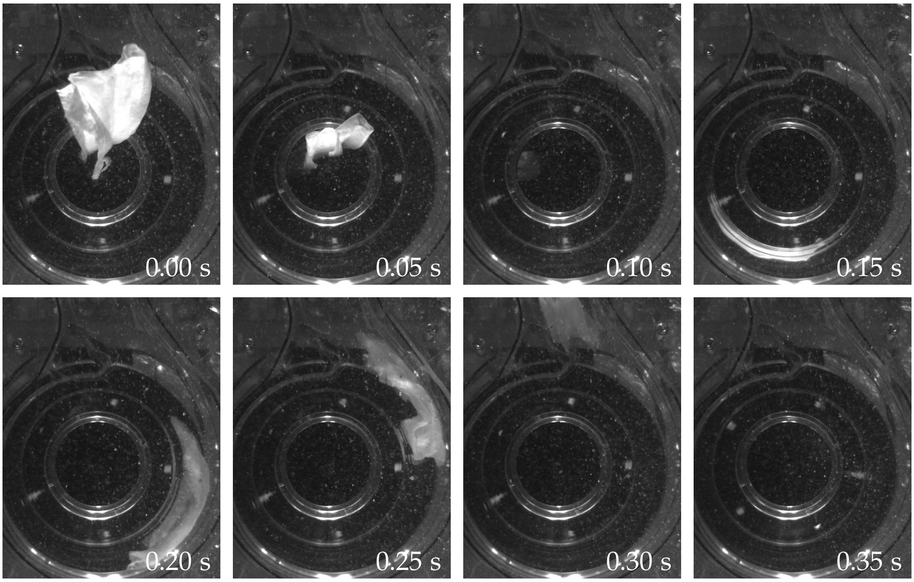

Fig. 4.14: Image sequence showing an example of a rag exiting the pump the first time it reaches the outlet.

the rags ended up leaving the pump before the test was terminated increased from 4% of the tests at 55% of Q_{BEP} to 100% closer to Q_{BEP}.

The increased tendency of the rags to recirculate in the volute and get stuck on the tongue at part load conditions can be explained by the change in the flow conditions inside the pump (Sørensen and Jensen, 2017). Using PIV the change in flow around the tongue was investigated by Bjerg et al. (2016) in the described pump geometry. They showed an increased flow from the high pressure side of the tongue to the low pressure side of the tongue as the pump was run in part load compared to near the best efficiency point. Similarly, Brownell and Flack (1984) used streak photography to visualise the flow near the tongue and construct streamlines based on the photographs. They used the streamlines to identify the tongue stagnation point, separation zones and approximate flow angles. They showed that, at low flow rates there was recirculation between the impeller and tongue and the stagnation point on the tongue moved to the outside of the tongue as the flow was deflected to the low pressure side of the tongue. Closer to the best efficiency point the stagnation point moved to the inside of the tip of the tongue.

When simulating clogging effects, the results presented in this section give valuable knowledge on how the rag can be expected to move inside the pump. This will be used for validation of the simulation results in Chapter 5.

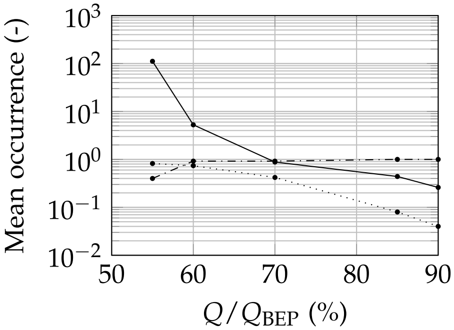

Fig. 4.15: The number of occurences of the rag 1) getting stuck on the tongue for more than one second, 2) recirculating in the volute or 3) exiting the pump, as function of the operating point. This figure was first presented in Paper B.

4.6 Concluding Remarks on the Experimental Investigations

Experimental investigation on the motion of rags in pumping systems has led to three main results:

- Detailed characterisation of rags at the inlet to a dry installed pump led to the conclusion that there are limited differences between the operating points. The lack of more significant changes indicates that the main reason for the occurrence of different types of clogging at different operating points is changed flow conditions inside the pump. The identified properties of elongation ratio, position, area and orientation of the rag in the suction pipe to a dry-installed pump describe appropriate initial conditions for simulation of rag transport inside a wastewater pump. Furthermore, it can form a case for validation of the coupled simulations through simulations of rags in a pipe with a bend.
- Experiments in a wet pit with a modified bottom show that the rags have different paths through the impeller at different operating points and shows that the risk of clogging at the impeller inlet in the tested pump type is highest close to the best efficiency point and in overload, while rags accumulated at the tongue in heavy part load conditions in the tested pump geometry.
- Results on the motion of rags inside the pump confirm that different types of clogging occur at different operating points and that the risk of clogging is highest at heavy part load conditions. The characterised

motion of the rags through the pump house form the basis for validation of the simulated motion of a rag through a wastewater pump in Chapter 5.

Chapter 5

CFD-DEM Simulation of Rag Transport in Wastewater Pumps

The coupling of CFD and DEM using ANSYS Fluent 18.1 and EDEM 2017.2 is described, and considerations on particle size and appropriate fluid force models are presented. This is followed by a description of simulations of the modelled rag (Chapter 3) moving through a wastewater pump in two cases: 1) when the pump is running at the best efficiency point and 2) when the pump is running in part load. The simulation results are compared to experimental results from the experiment described in Section 4.5. A preliminary study using the coupling between ANSYS Fluent and EDEM was presented in Paper D.

5.1 CFD-DEM Coupling

The motion of a rag through a wastewater pump is simulated by coupling the modelled rag, described in Chapter 3, with a CFD simulation of the fluid flow through a pump. A coupling interface between the commercial DEM software EDEM and the commercial CFD software ANSYS Fluent already exists and version 2.2 of this coupling is used for the coupled simulation.

As briefly described in Chapter 1, the discrete element model of the rag is not resolved by the CFD mesh in the coupled simulations, and therefore the fluid force on each of the particles forming the rag must be modelled. Figure 5.1A shows an example of a coupled CFD-DEM case. A fibre of four bonded particles is sketched in a CFD mesh with four cells. There is a different fluid velocity u_f in each of the cells, and each of the particles have different velocities u_p. To determine the fluid force on a DEM particle in

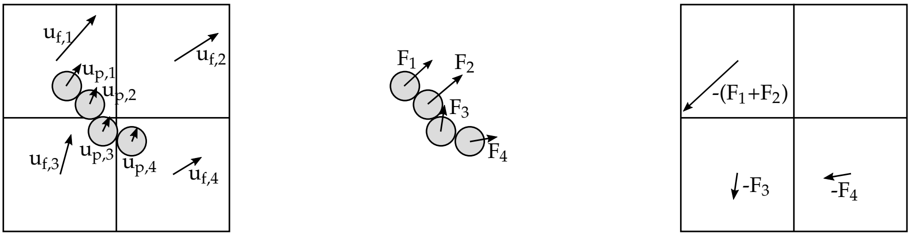

A) Coupled simulation

B) DEM solver:
Particles influenced by the fluid

C) CFD solver:
Fluid influenced by particles

Fig. 5.1: Sketch of momentum coupling between particles and fluid. A) Velocity of particles and fluid. B) The particles are influenced by a fluid force determined based on a force model and the relative velocity between particles and fluid. C) The fluid is influenced by the particles through a source term in CFD. The source term is determined based on the sum of fluid forces on the particles in each cell.

a coupled CFD-DEM simulation, the cell in which the particle is located is identified and the force is determined using a force model and the relative velocity between the particle and the fluid velocity in the cell. Figure 5.1B illustrates the determined fluid force on each of the four particles. The determined fluid force is transferred to the DEM solver where it is used to determine the acceleration of the particles. Finally, for each cell containing one or more particles, a momentum source term is determined based on the fluid force on the particles in the cell as sketched in Figure 5.1C. If there is more than one particle in a cell, the total force acting on the particles in the cell is used to determine the momentum source term. Using the existing coupling between EDEM and ANSYS Fluent it is possible to choose Lagrangian coupling where only momentum is exchanged between the DEM and CFD solver and Eulerian coupling which also solves for the volume fraction.

During a coupled simulation ANSYS Fluent and EDEM are simulating alternately as illustrated in Figure 5.2. The coupled simulation is initiated in ANSYS Fluent which runs a time step before calling EDEM, which runs the same time step. Commonly the time step in DEM is much smaller than the CFD time step. Therefore, EDEM runs the number of time steps necessary to reach the same time as ANSYS Fluent.

Figure 5.3 gives an overview of a DEM time step. The figure is modified from Figure 3.1, which did not include coupling to a fluid phase. EDEM moves the geometry if a geometry motion is defined, and generates particles in simulations where particles are continuously generated. Then particle contacts are detected and contact forces are calculated. Based on the contact forces as well as the fluid forces from ANSYS Fluent, gravity etc., the particle position and velocities are determined and the bonds are updated. In step 7-8 data on particle velocities and positions are transferred from EDEM to ANSYS Fluent. In ANSYS Fluent the particles are handled using the Discrete

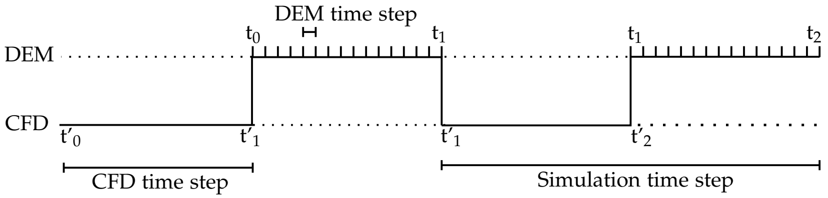

Fig. 5.2: ANSYS Fluent and EDEM simulates alternately in coupled transient simulations. ANSYS Fluent finishes a time step and transfers information to EDEM which simulates to the same point in time. Note that the DEM time step is generally several times smaller than the CFD time step. Therefore the DEM simulation requires more time steps to reach the same time as the CFD simulation.

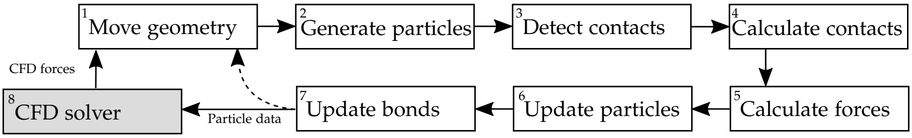

Fig. 5.3: Overview of an iteration in EDEM when coupling to ANSYS Fluent.

Phase Model (DPM) framework. Within a time step, ANSYS Fluent calculates the fluid forces on the particles using force correlations and updates the momentum sources in each cell based on the determined fluid forces. Subsequently, the determined fluid force on each particle is transferred back to EDEM (step 8-1) where it is one of the forces used to determine the acceleration of the particles.

5.1.1 Modelling of Drag on the Rag

The modelled rag is formed by a collection of spherical particles as described in Section 3.2, and illustrated in Figure 5.4. Similar to the fibre sketched in Figure 5.1, a fluid force will be determined for each of the particles forming the rag in a coupled simulation. The drag force is expected to be the dominating fluid force on the rag, and only the drag force will be included in the present coupling. Currently, the free stream drag model for spherical particles and the model for non-spherical particles by Ganser (1993) are implemented and can be used to model the fluid force on the particles in coupled simulations.

Paper D presented simulations of flexible fibres of bonded particles in shear flow and briefly discussed the use of the free stream drag model to determine the fluid force on each of the particles forming the fibre. As mentioned in the paper, no drag model has been developed for an application similar to the current simulation of a rag of bonded particles and it is unknown how the overall shape of the rag will affect the drag on each of the

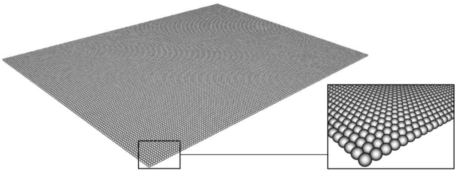

Fig. 5.4: Image of the arrangement of spherical particles in an uncrumbled rag. The particles are bonded to collectively form a flexible surface to represent a rag.

particles forming the rag. Despite this, the free stream drag model was used in the study presented in Paper D. Using the free stream drag model the drag coefficient is determined as given in Equation (5.1).

$$c_\mathrm{d} = \begin{cases} 24/\mathrm{Re}, & \text{if } \mathrm{Re} \leq 0.5; \\ 24 \cdot \left(1 + 0.15 \cdot \mathrm{Re}^{0.687}\right)/\mathrm{Re}, & \text{if } 0.5 < \mathrm{Re} \leq 1{,}000; \\ 0.44, & \text{otherwise.} \end{cases} \tag{5.1}$$

The free stream drag model, and drag models in general, depend on the particle Reynolds number which is calculated based on Equation (5.2).

$$\mathrm{Re} = \frac{\rho_\mathrm{f} \cdot v_\mathrm{rel} \cdot d_\mathrm{p}}{\mu_\mathrm{f}} \tag{5.2}$$

Where v_rel is the relative velocity between the particle in question and the fluid, ρ_f is the density of the fluid and μ_f is the viscosity of the fluid. In a simulation of rag transport through a wastewater pump, the rag will in some cases be following the fluid resulting in particle velocities very close to the fluid velocity. In other cases the rag will be stuck at the tongue with particle velocities close to zero leading to a higher relative velocity between the particles forming the rag and the fluid in the pump. Therefore, a large variation in the particle Reynolds number is expected during a simulation.

Similar to the work presented in Paper D, Lindström and Uesaka (2007) also modelled a flexible fibre in fluid flow as a chain of segments, taking into account a separate fluid force on each of the segments. They modelled both the viscous effects and dynamic effects of drag opposed to previous studies on flexible fibres taking only the viscous effects for low particle Reynolds numbers into account (Yamamoto and Matsuoka, 1993; Schmid et al., 2000). Lindström and Uesaka (2007) approximated the viscous drag force and torque on a cylindrical segment based on an analytical solution combined with a semi-empirical formula valid for isolated particles, like the assumption in the free stream drag model. The dynamic drag on the fibre was approximated by the drag on a finite section of an infinite cylinder.

Eberhardt et al. (1996) modelled a rag using a particle based approach and discussed the difficulty of determining a value of the drag coefficient for each particle because of the dependency of the location of the particles in the rag. In the model by Eberhardt et al. (1996), all particles with four neighbouring particles inside the cloth had the same drag coefficient, while the particles at the border had a higher drag coefficient. It was stated by Eberhardt et al. (1996) that *"this model of air resistance is very simple and could be improved, but calculating an individual* c_w *for each particle is a difficult and expensive task"*.

Looking into studies on agglomerates, which can be complex structures consisting of several particles, different suggestions have been made on how to take the agglomerate shape into account when calculating the fluid force on the agglomerate. Dietzel and Sommerfeld (2013) performed high resolution simulations using the Lattice-Boltzmann method to determine correlations between the structure of the agglomerates and the fluid force. The correlations were used to simulate agglomerates as point particles, not considering the fluid force on each of the particles separately. Subsequent to the work by Dietzel and Sommerfeld (2013), Sommerfeld and Stübing (2017) presented an agglomeration model storing vectors from the initial primary particle to each of the particles collected by the agglomerate. Using this information, and the correlations by Dietzel and Sommerfeld (2013), the agglomerates were simulated as point particles with a drag coefficient accounting for the overall shape of the agglomerate.

As it is the case in the mentioned rag model by Eberhardt et al. (1996) and the fibre model by Lindström and Uesaka (2007), each of the particles forming the rag will have a fluid force acting on them in a coupled simulation. The fact that the rag consists of more particles forming a 2D surface makes it harder to justify the approximation of isolated particles by Paper D and Lindström and Uesaka (2007). However, the influence of the neighbouring particles on the drag is unknown. With inspiration from Sommerfeld and Stübing (2017), a structure model storing location vectors of the particles may be a step on the way, if the drag on each particle can be made dependent on the position of the neighbouring particles or even the overall shape of the rag. However, this solution is cumbersome and will be computationally expensive. Therefore, the solution adopted in Paper D, using the free stream drag model is also used for the preliminary simulations presented here.

Keeping these considerations in mind, there are uncertainties connected with the choice of the free stream drag model. Since drag is expected to be the dominating fluid force on the rag, and due to the difficulty of describing separate forces on each of the particles, only the free stream drag model is included, neglecting lift, virtual mass and other fluid forces. An investigation of the influence of the fluid force model(s) on the result is an interesting perspective for further work.

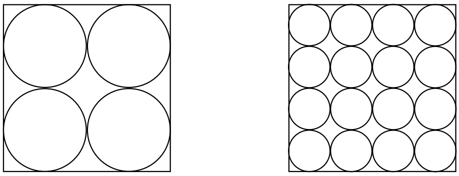

Fig. 5.5: Sketch of cases with different particle sizes forming the rag. The ratio between the area of rectangular surface and the area covered by the particles is constant and is $\pi/4$.

5.1.2 Considerations on Particle Size and Density

Since the rag is modelled as a collection of spherical particles, the thickness of the surface changes as the discretization changes. This was briefly discussed in Section 3.2, where the arrangement of the particles to form a flexible surface was determined. As discussed, the particle density is changed if the particle size is changed to ensure that the total weight of the rag is constant. This is opposed to keeping the density constant meaning that the larger the particles the higher the total weight of the rag. By changing the particle density the gravitational force and buoyancy will change. However, since the density of rags and similar materials in real life will be close to the density of the water and thereby neutrally buoyant and since fluid forces are expected to be the main force contribution to the motion of the rags inside pumps, gravity and buoyancy forces are neglected in the simulations.

Figure 5.5 illustrates two different sizes of spherical particles forming the rag surface. Assuming the relative velocity between particles and fluid to be the same, smaller particles forming the rag lead to smaller particle Reynolds numbers (Eq. (5.2)). Using the free stream drag model, the drag coefficient is decreasing as the Reynolds number increases until a Reynolds number of 1000 where the coefficient becomes constant (Eq. (5.1)). The ratio between the area covered by the particles forming the rag and the area of the rectangular rag surface is $\pi/4$ and is independent of the particle size, furthermore as mentioned above, the mass per unit area is kept constant as the particle size changes. The adjustment of the particle density to ensure a constant mass per unit area, and the constant area covered by the particles independent of the size, would lead to the acceleration of the particles being independent of the particle size if the drag coefficient did not depend on the particle Reynolds number. Due to the change in the drag coefficient with the particle Reynolds number, the acceleration of larger particles will be smaller than the acceleration if the rag was formed by smaller particles. This is clearly impractical for the present case and a new drag formulation is required to fix it.

The current EDEM-ANSYS Fluent coupling (version 2.2) uses the position of the centre of the particles when identifying the cells in which the

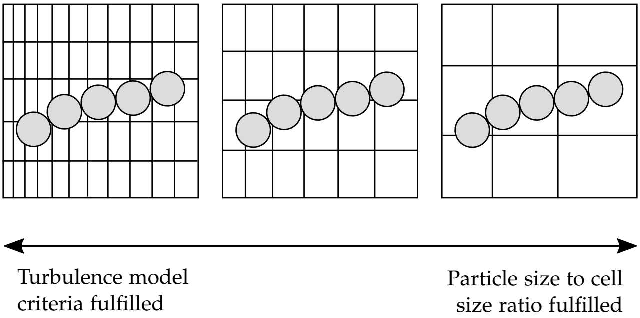

Fig. 5.6: Particle size and cell size ratio for three different grids. If the grid meets the turbulence model criteria at the wall the particle size commonly exceeds the cell size. Oppositely, if the cell size is large enough to meet a particle size to cell size ratio of less than one, the turbulence model criteria at the wall can possibly not be fulfilled.

particles are located. Even though a particle can cover more cells, the momentum source is only acting in the cell where the centre of the particle is located. This is problematic if the particle is around the same size as the cell or larger. Therefore the particles need to be smaller than the cells in the CFD mesh. This criteria is especially hard to satisfy at the wall boundaries of the mesh as RANS turbulence model requirements dictate the cell size at the boundary. This is sketched in Figure 5.6. The issue can be partly overcome using wall functions, allowing a larger cell size at the boundary. Furthermore, to allow a larger particle size and improve stability in cases where the particle size is close to the cell size, smoothing can be enabled to spread the particle sources over more cells which can improve the stability. Finally, simulations using the Lagrangian type of coupling where only the momentum is exchanged between fluid and particles and the volume of the particles is not used to determine a particle-fluid volume fraction in each cell are less sensitive to particle-cell size requirements. The Lagrangian coupling is for dilute systems with low particle fraction. Despite this, the Lagrangian coupling is used in the preliminary coupled simulation of rag transport through a pump presented in the following section.

5.2 Simulation of Rag Transport in a Pump

The following section presents preliminary results of a coupled CFD-DEM simulation of a rag moving through a single channel impeller in a pump geometry corresponding to the geometry used in the experiments presented in Section 4.5. The preliminary simulation acts as a proof of concept of the coupled CFD-DEM model being able to simulate the modelled rag passing through a pump with the current setup. Note that the discussed uncertainties

Fig. 5.7: The pump geometry used for the simulation of a rag as it moves through a pump. The pump has a single channel impeller the length of the inlet pipe is three times the inlet diameter and the length of the outlet pipe is eight times the outlet diameter.

in e.g. the modelling of fluid forces and the Lagrangian type of coupling leaves room for improvement of the accuracy of the coupling.

5.2.1 Geometry and Mesh

The pump geometry used in the simulations corresponds to the pump used in the experiments with a transparent house described in Section 4.5. As described, the pump has a single channel impeller and an inlet diameter of 100 mm and an outlet diameter of 80 mm. To simplify the geometry for simulation, the simulated pump has an inlet pipe like a dry-installed pump instead of the setup with a submersible pump used in the experiments. The pump geometry used for the simulation is illustrated in Figure 5.7. The inlet pipe length is 3 times the pipe diameter and an outlet pipe length is 8 times the pipe outlet diameter to ensure well defined inlet profiles and prevent recirculation in the outlet. The geometry and mesh has been provided by Grundfos and no further analysis on mesh independence and quality has been performed. The mesh consists of $1.1 \cdot 10^6$ tetrahedral cells with a minimum volume of $1.3 \cdot 10^{-12}$ m^3 and a maximum volume of $4.4 \cdot 10^{-7}$ m^3.

A sliding mesh enables rotation of the impeller in the transient simulation. The interface between the stationary and the rotating part of the mesh is sketched in Figure 5.8. Since the geometry corresponds to the geometry used in the experiments described in Section 4.5, the simulated operating point is chosen to correspond to an operating point used in the experiments with an impeller speed of 1200 RPM.

5.2.2 Simulation Setup

The setup of the coupled simulation of rag transport through a wastewater pump is described in the following. The rag is simulated in EDEM 2017.2, the flow through the pump is simulated using ANSYS Fluent 18.1. The simulations are coupled using the commercially available EDEM-ANSYS Fluent coupling interface (version 2.2).

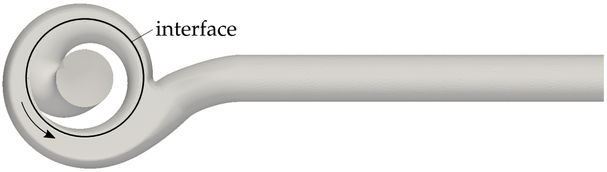

Fig. 5.8: To enable impeller rotation, the mesh has an interface between the rotating impeller and the stationary part of the mesh.

DEM

The model of the rag presented in Chapter 3 is used in the coupled simulation. The radius of the particles forming the rag was 1 mm. The rag used in the experiments has a size of 300 mm × 220 mm, leading to a rag of 150 particles × 110 particles. The particle arrangement and bond properties correspond to the properties determined in Chapter 3. These properties are listed in Table 5.1. See Chapter 3 for more detail on the rag model.

When an EDEM simulation starts, bonds are formed between time zero and a specified time after this. The bonds are formed if the particle contact radii overlap and if a bond is defined between the two particle types (Section 3.2). Since the number of contacts in a crumbled rag will lead to the formation of unwanted bonds, the rag is initially placed as a straight surface. As the length and the width of the rag are larger than the inlet pipe diameter in the present geometry, the rag must initially be placed outside the inlet pipe and an initial simulation without coupling to the fluid phase is made for the rag to move into the inlet pipe under the force of gravity. The rag is placed above the inlet pipe and a geometry of a hopper is placed below the rag, gravity is acting on the rag, and the hopper leads the rag into the inlet pipe. When the rag is fully inside the inlet pipe, the simulation is stopped and a simulation deck is saved with the rag inside the inlet pipe at time zero. The bond model is altered so that no new bonds will be formed when the simulation is started again. Breaking criteria of maximum force and moment on the bond are not included in the present simulation.

The diameter of the inlet pipe in the geometry used for the present simulation is 100 mm compared to a diameter of 200 mm used in the experiments presented in Section 4.3 to determine appropriate initial conditions for simulations. Therefore it is not possible to directly use the knowledge obtained from the experiments to determine realistic initial conditions for the present simulation. The rag is placed so it is close to parallel to the flow direction and the elongation ratio is 6.9. This is higher than the average of 3.1 observed in the experiments, but not unseen as illustrated in Figure 5.9. Figure 5.10 illustrates the initial position of the rag before the coupled simulation is started.

EDEM Settings	
Time integration scheme	Runge Kutta
Time step	5e-7 s
Particle radius	1 mm
Bond radius	1 mm
Particle contact radius	2 mm
Particle density	538 $\mathrm{kg/m^3}$
Number of particles	16500 particles
Rag size	300 mm × 220 mm
S_n (CW)	$4.23 \cdot 10^8$ $\mathrm{N/m^3}$
S_t (CW)	$5.00 \cdot 10^6$ $\mathrm{N/m^3}$
$S_\mathrm{n,b}$ (CW)	$1.03 \cdot 10^7$ $\mathrm{N/m^3}$
S_n (LW)	$7.65 \cdot 10^8$ $\mathrm{N/m^3}$
S_t (LW)	$5.00 \cdot 10^6$ $\mathrm{N/m^3}$
$S_\mathrm{n,b}$ (LW)	$3.86 \cdot 10^7$ $\mathrm{N/m^3}$

Table 5.1: Details of the DEM simulation setup.

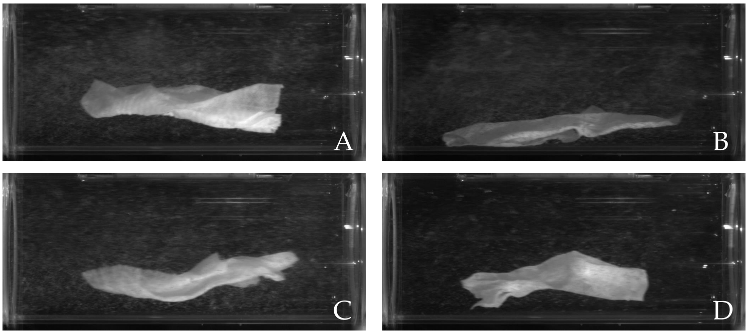

Fig. 5.9: Example of rags in the inlet pipe to a dry-installed pump during experiments (Section 4.3). Note that the diameter of the inlet pipe is double the diameter of the inlet diameter in the simulated geometry. Elongation ratio: A) 5.2, B) 8.5, C) 6.0, D) 4.5

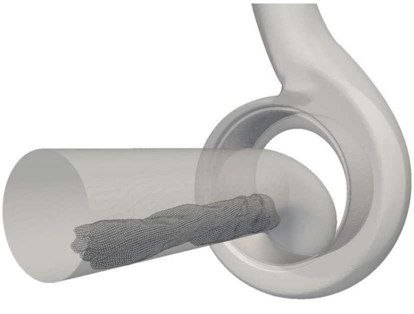

Fig. 5.10: Initial position of the rag before the coupled CFD-DEM simulation is started.

CFD

The flow in the pump is simulated using ANSYS Fluent. Prior to the coupled simulation, the CFD case is run to ensure that the CFD solution has reached a steady cycle independent of start up phenomena. An interpolation file is saved and loaded when starting the coupled simulation. It is ensured that the impeller position at the last time step of this simulation is exactly the same as it was initially.

The simulation uses a pressure based transient solver and the k-ϵ turbulence model with standard wall functions. The pumped fluid is water with a density of 998.2 kg/m^3 and viscosity of 1.003 mPa·s. As mentioned, the gravity force is not included in the simulation.

The simulation uses pressure inlet and pressure outlet boundary conditions. At the pressure outlet, a target mass flow of 26.8 kg/s is specified, corresponding to the best efficiency point at an impeller speed of 1200 RPM. The gauge pressure at the outlet is specified to 32200 Pa, corresponding to the expected head gain. The geometry wall has a no slip boundary condition. A time step of 0.1 ms corresponding to an angular impeller motion of 0.72 degrees per time step is chosen. The settings are summarised in Table 5.2.

Coupling

The coupled simulation is initiated in ANSYS Fluent. The coupling is initiated by starting the coupling server in EDEM and loading a coupling journal file in ANSYS Fluent. After loading the journal file, the coupling settings can be chosen in a new menu. This preliminary simulation, uses a free stream drag model for spherical particles and Lagrangian coupling which does not take the volume of the particles into account in ANSYS Fluent. When the coupled simulation has been initiated in ANSYS Fluent, data is transferred between EDEM and ANSYS Fluent in each simulation time step.

The simulation of rag transport in a wastewater pump was made for two

CFD Simulation Settings	
Turbulence model	k-ϵ
Impeller speed	1200 RPM
Target mass flow	26.8 kg/s
Pressure at outlet	32200 Pa
Fluid density	998.2
Fluid viscosity	0.001003
Max iterations per time step	80
Time step	0.0001 s

Table 5.2: Simulation approach used in the present work.

cases. Firstly, the flow through the pump was simulated at the best efficiency point of the pump. Secondly, the flow through the pump was simulated at heavy part load condition with a flow rate of 55% of the flow rate at the best efficiency point. The initial condition of the rag for the two cases was the same. As seen in Figure 5.10, the rag is parallel to the pipe and as mentioned the rag is placed so that the elongation ratio defined in Chapter 4 is high. The following two subsections present the results of the coupled simulations.

5.2.3 Simulation of Rag Transport in a Pump Operating at the Best Efficiency Point

The images in Figure 5.11 illustrate how the rag moves through the pump in a coupled simulation where the fluid flow through the pump corresponds to the flow at the best efficiency point at an impeller speed of 1200 RPM. The figure illustrates nine steps from time 0 ms to time 160 ms. The rag moves into the pump and folds around the impeller in the first five images. In the last four images the rag moves outwards in the housing and it leaves the pump as it reaches the outlet.

Figure 5.12 shows nine images from the experiment. The images show a rag moving through the pump. The time is defined to time 0 ms at the point where the rag starts moving into the impeller. This is evaluated based on images from the side of the pump. The image at time 0 ms in Figure 5.12 corresponds to the image to the left in Figure 5.13. On the first four images the rag moves into the pump. On the fifth image the rag is barely visible inside the impeller. At time 200 ms the first part of the rag appears inside the housing and in the last three images the rag moves outwards in the housing. Notice how this motion is very similar to the motion observed in the simulated case presented in Figure 5.11.

The geometry used for the simulation has an inlet pipe instead of the tank used in the experiments. This entails that the boundary conditions in

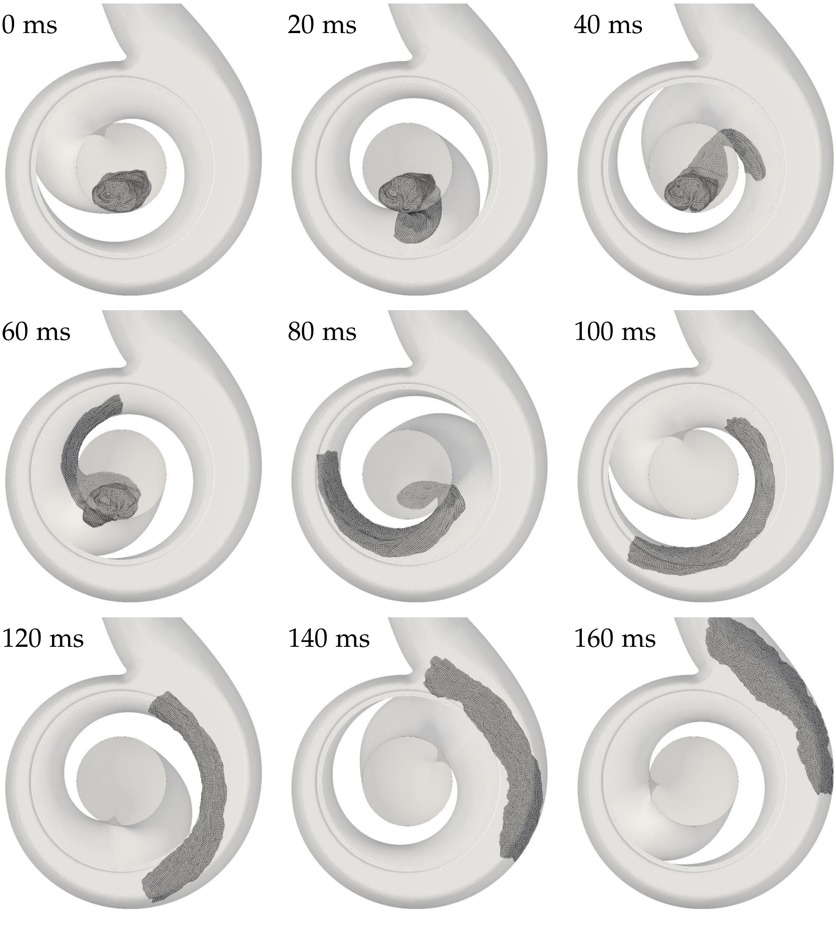

Fig. 5.11: Simulation of the modelled rag moving through a pump. The pump is operating at the best efficiency point with an impeller speed of 1200 RPM.

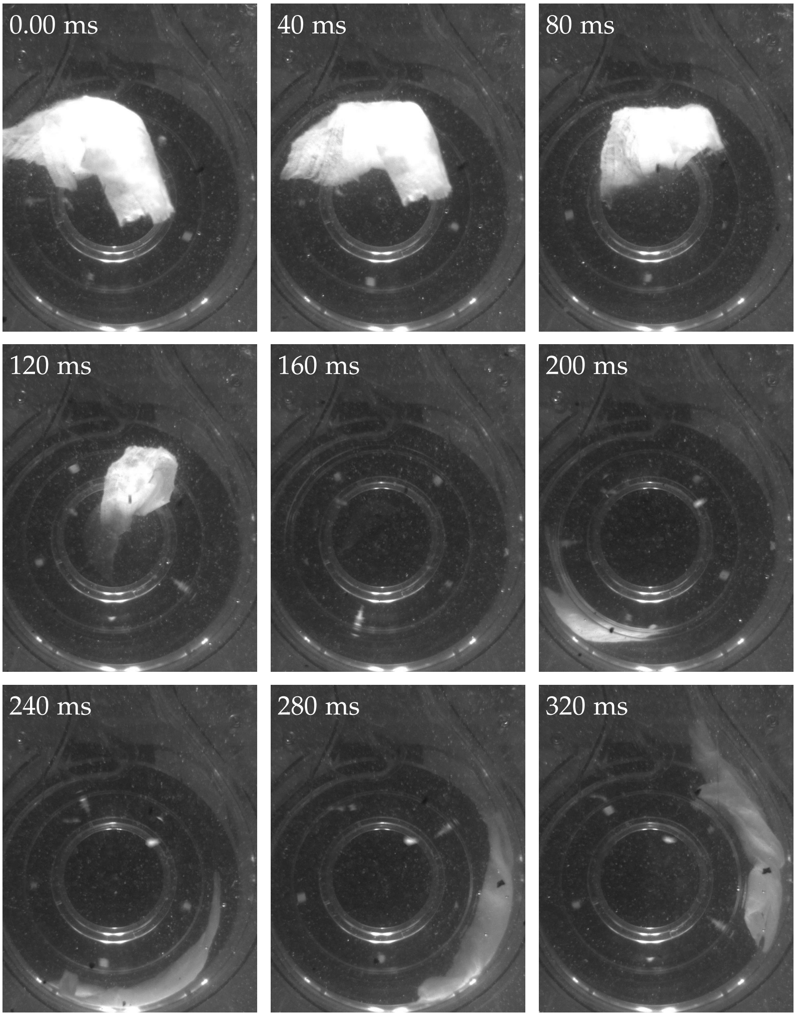

Fig. 5.12: Example of a recording from the experiments described in Section 4.5. The pump is operating at the best efficiency point with an impeller speed of 1200 RPM. The rag enters a housing and impeller geometry corresponding to the simulated geometry.

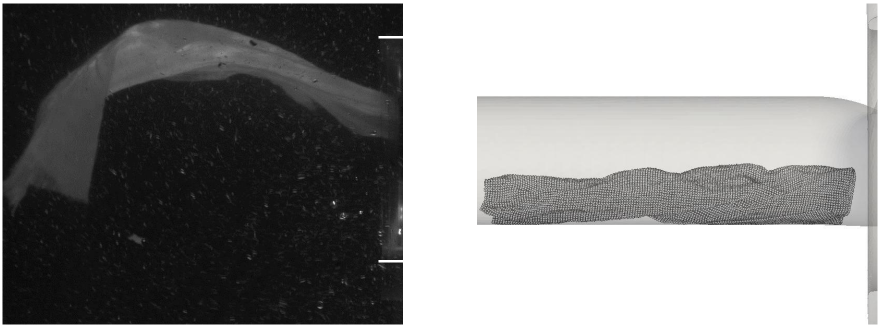

Fig. 5.13: Initial condition of the rag in the simulation and a case from the experimental investigation presented in Section 4.5. The white lines mark the pump inlet.

the simulation are different from the boundary conditions in the simulations. The influence of the boundary conditions on the flow inside the pump is unknown, and may cause differences in the results. However, in connection with the experiment described in Section 4.5, the pump was filmed from the front but also from the side, recording the rags as they moved into the pump. Based on these images, an experiment with initial conditions resembling the simulation case was identified. This is illustrated in Figure 5.13.

The main difference between the experimental results and the simulation, is the time that it takes for the rag to move through the pump. Notice that the time interval between the images in the experiment is twice the time interval between the images from the simulation. Sørensen and Jensen (2017) experimentally identified the average retention time of the rags inside the housing of the present pump geometry to be 239 ms. The retention time is defined as the time from when the whole rag is inside the pump house to the time where the whole rag has left the pump house. Notice that the time marked in the image as time 0 ms, does not correspond to time 0 ms when determining the retention time. In the case illustrated by the images in Figure 5.12, the retention time was 240 ms, which is very close to the mean. However, it is much higher than for the simulated case where the retention time was 130 ms.

With a standard deviation in the retention time measured in the experiments of 75 ms, the simulated results is however still within two standard deviations from the mean. Recall from Section 4.5 that the experiment was repeated 50 times. In one of the 50 times the rag was recorded passing through the pump, the retention time was 110 ms, which is lower than the simulation result. However, in this case the initial condition and the characteristics of the rag were very different from the characteristics of the rag in the simulation results. This is illustrated in Figure 5.14, which shows the recorded motion of the rag in this case. It is seen in the figure that the rag is much less elon-

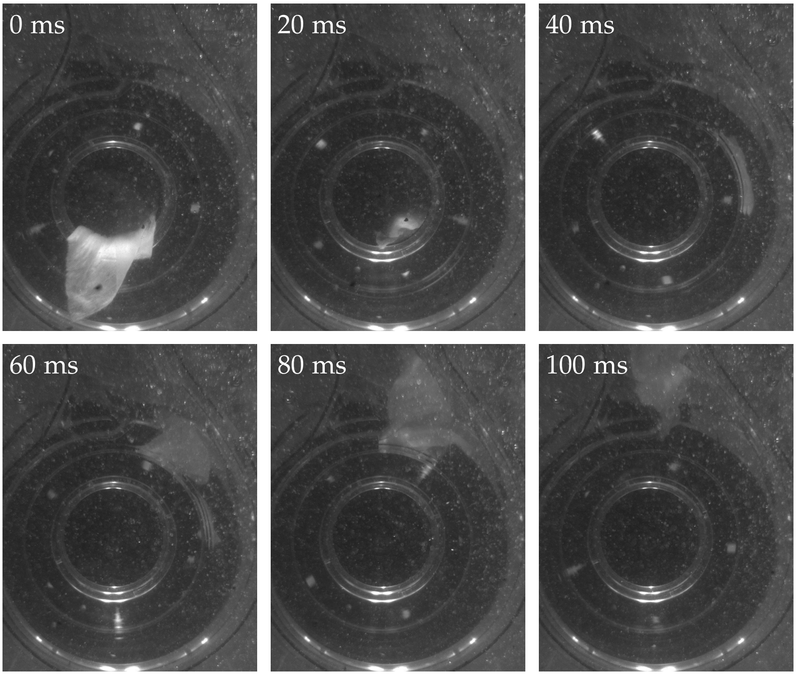

Fig. 5.14: Example of a recording from the experiments described in Section 4.5, where the rag has a short retention time in the pump. The pump is operating at the best efficiency point with an impeller speed of 1200 RPM. The rag enters a housing and impeller geometry corresponding to the simulated geometry.

gated than in the simulation case, and furthermore the rag leaves the pump impeller very close to the outlet of the pump and proceeds directly to the outlet with no interaction with the tongue. Based on these clear differences, and the clear correspondence in the motion of the rag comparing Figure 5.12 and 5.11, it is most likely that the simulation result underestimates the time that the rag stays inside the pump.

5.2.4 Simulation of Rag Transport in a Pump Operating in Part Load

In the experiments presented in Section 4.5 a clear change in the motion of the rag through the pump was observed when going from the best efficiency point to heavy part load conditions. Therefore, a simulation of rag transport through a pump in part load condition is done to see if the same changes can be observed. The described simulation setup is used again. However, the outlet boundary conditions are changed to simulate the pump in part load condition with a flow of 55% of Q_{BEP}.

Figure 5.15 illustrates the simulated motion of the rag through the wastewater pump running in part load. As seen by a comparison of this figure with Figure 5.12, it takes longer time for the rag to pass through the pump. This is a natural consequence of the lower flow rate through the pump. However, also the interaction between the rag and the pump geometry contributes to the time the rag stays in the pump, as the rag is stuck on the impeller inlet for a longer time than it was the case at the best efficiency point.

During the experimental investigation the rag was observed to recirculate hundreds of times in the volute and getting stuck on the tongue when the pump was running in the simulated part load condition. Figure 5.16 illustrates an example of the motion of the rags in the pump observed experimentally as described in Section 4.5. It is seen in the figure how the rag recirculates in the volute. As the rag reaches the outlet after 490 ms it re-enters the volute rather than exiting the pump. Additionally, as the rag reaches the outlet again after 650 ms, it gets briefly stuck on the tongue before it continues recirculating in the volute. As discussed in Section 4.5, this is a consequence of an increased flow from the high pressure side of the tongue to the low pressure side. Furthermore, the decreased flow rate entails a lower fluid velocity outwards in the housing. Note that a re-circulation of the rag in the volute takes approximately 200 ms (image 450 ms to image 650 ms), while a rotation of the impeller at 1200 RPM takes 50 ms. This clearly indicates that the rag is no longer attached to the impeller as it recirculates in the volute.

The inlet flow from a pipe in the simulations rather than from the a tank as in the experiments may be a contributing factor to the observed differences. As the simulated rag is initially placed in an inlet pipe where the

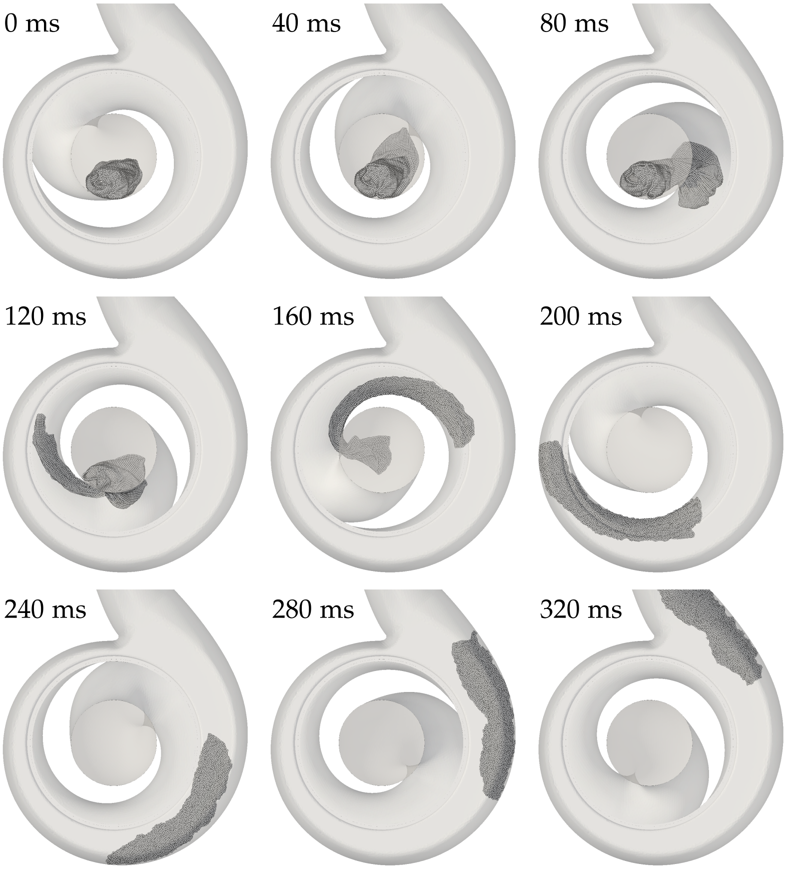

Fig. 5.15: Simulation of the modelled rag moving through a pump. The pump is operating in part low with 55% of Q_{BEP} at an impeller speed of 1200 RPM.

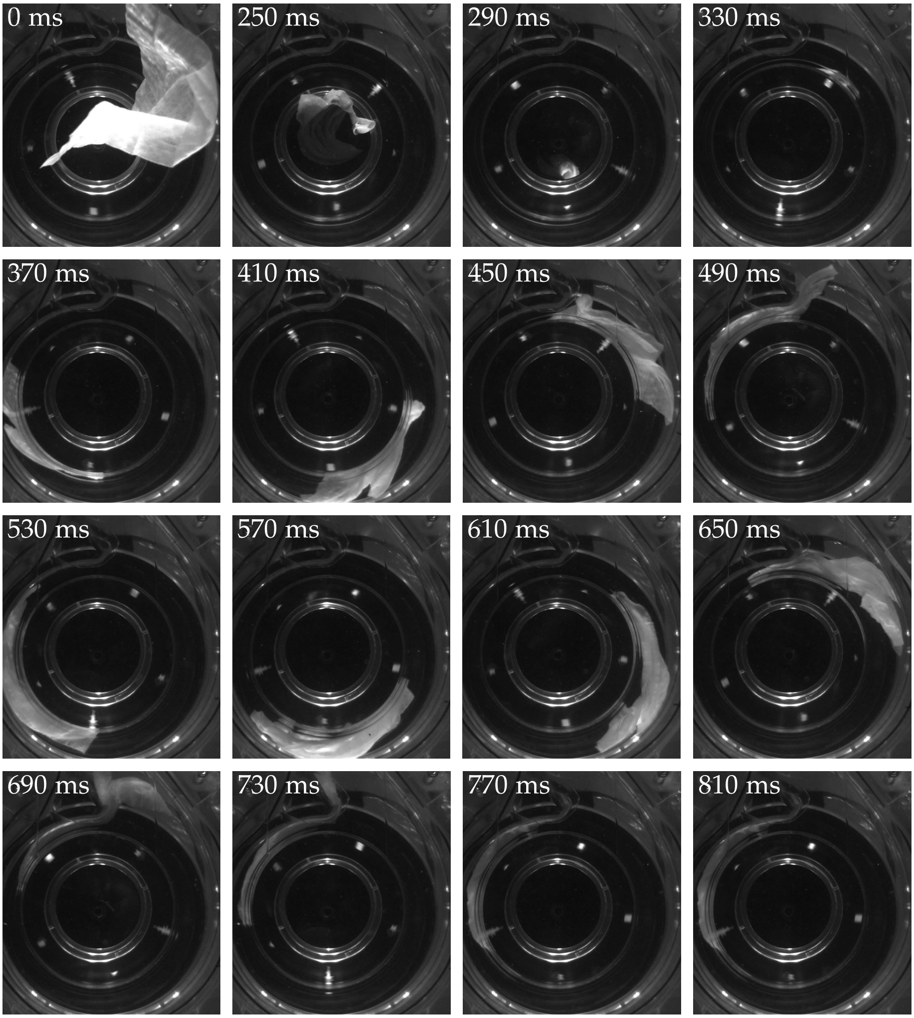

Fig. 5.16: Example of a recording from the experiments described in Section 4.5. The pump is running in part load with 55% of Q_{BEP} at an impeller speed of 1200 RPM. The rag enters a housing and impeller geometry corresponding to the simulated geometry.

fluid velocity into the pump is high, the rag is quickly accelerated to the fluid velocity. Oppositely, the water surrounding the rag in the experiments may not have a high velocity towards the pump inlet, only immediately in front of the inlet. Therefore, it may be expected that the acceleration of the rag into the pump takes longer time in the experiment than in the simulation. This corresponds to the observed difference as it takes the rag around 250 ms from a position where the front part of the rag is right in front of the pump inlet until the whole rag is inside the pump in the experiments, compared to around 120 ms in the simulation.

The simulation of the motion of the rag through a wastewater pump in part load does not resemble the experimental results as the rag after seven impeller rotations and no re-circulations in the volute leaves the pump. The difference between the simulation result and the observations during experiments may be due to the simplified modelling of fluid forces on the rag.

5.3 Concluding Remarks on the Preliminary Simulations of Rag Transport in a Wastewater Pump

Simulation of rag transport through a wastewater pump at two different operating points have been achieved using coupled CFD-DEM.

The results of the coupled simulations of rag transport through a wastewater pump are similar to experimental results from a test rig with a pump corresponding to the simulated geometry. However, there is a tendency of the simulations to underestimate the time that it takes the rag to move through the pump. This may be due to the simplified coupling or due to the impeller-rag interaction as the rag stayed inside the impeller for a longer time during the experimental investigation.

Due to the simplifying assumptions in connection with the fluid force modelling and coupling between CFD and DEM, the presented simulations are preliminary and serve as a proof of concept that the CFD-DEM approach can be used to simulate clogging effects in wastewater pumps.

Chapter 6

Closure

Main conclusions of the dissertation are summarised followed by an outlook with suggestions for future work.

6.1 Conclusion

Simulation of clogging in wastewater pumps requires 1) simulation of the fluid in the pump, 2) simulation of the material causing clogging e.g. a rag, 3) handling of the interaction between the rag and the fluid as well as between the rag and the pump. This is accomplished using CFD to simulate the fluid and bonded DEM to simulate a rag.

A literature review showed that wet wipes are commonly the cause of clogging issues in real life applications. However, ongoing work to define a standard for evaluating the performance of wastewater pumps uses a synthetic non-woven dust cloth (rag). Since this is currently the closest one can get to a standard piece of textile to create artificial wastewater, this rag was also used in the present work in all experiments and simulations.

The 'updated bond model' in EDEM, based on Potyondy and Cundall (2004) and used by Guo et al. (2013b) for modelling of flexible fibres, has not previously been used to model textile behaviour. Using this model, the out of plane bending stiffness and the tensile stiffness are the same. However, due to the fibre structure in textile material the bending stiffness is not related to the tensile stiffness. Therefore the bond model was modified to separate the bending stiffness from the tensile stiffness. After this modification the bond model requires inputs of normal stiffness S_{n}, tangential stiffness S_{t} and bending stiffness $S_{\mathrm{n,b}}$. The particles and bonds were placed in an in-line arrangement where each particle was bonded to four neighbouring particles, except on the boundary of the rag. The bond model was calibrated based on elongation, bending and drape experiments using wet rags under standard climate conditions. The normal stiffness was calibrated based on an elongation test, the bending stiffness was calibrated based on a bending test. Finally, the tangential stiffness was calibrated based on a drape test. The final static drape shape was compared to the measured drape using quantitative parameters of drape area and size of the drape waves. There was a good correspondence between the final simulated drape after calibration and the experimental results with deviations between 1% and 7% in the drape area and 2% for the size of the drape waves in three cases using particle radii of 1 mm, 1.5 mm and 2 mm respectively.

Experimental investigations using image analysis to characterise the motion of rags in pumping systems were used to determine realistic initial conditions of the rag for simulations and to enable validation of simulations of rag transport in pumping systems. Since different types of clogging have been observed at different operating points in previous experimental investigations, the experiments were done at various operating points. The rags in the inlet pipe to a dry installed pump were characterised by properties of position, elongation ratio, orientation and 2D area. Of these properties, only the mean area changed significantly with the operating point from 0.011 m^2 (16.7% of maximum posible 2D area) at high flow rates at the best efficiency point to 0.015 m^2 (22.7% of maximum posible 2D area) at the lowest flow rate where the pump was operating in heavy part load. An investigation of the motion of textiles at the inlet to a submersible pump revealed different positions of the rag as it moved through the impeller. A transparent pump house was constructed based on a real pump geometry to further investigate the motion of rags inside the pump. At each operating point the number of re-circulations in the volute, the occurrence of the rag been stuck on the tongue for more than one second, and the number of rags exiting the pump within one minute was identified. Furthermore, the motion of the rag from the impeller outwards in the housing was analysed. At 55% of Q_{BEP}, the average number of re-circulations of the rag in the volute was 111. This was reduced to less than one when the pump was operating at the best efficiency point. Simultaneously, the number of rags leaving the pump within the time frame was increased from less than half at 55% of Q_{BEP} to all at 90% at Q_{BEP}.

Using a mesh and pump geometry provided by Grundfos, coupled simulations of a rag moving through a pump were achieved. The rag motion in a simulation with the pump running at the best efficiency point clearly resembled the rag motion recorded during the experiments using the transparent housing. However, the simulation underestimated the time the rag spend inside the housing. This may be a result of the drag model, the Lagrangian type of coupling not taking the volume of the particles into account in the CFD solution or the simulation geometry having an inlet pipe like a dry-installed pump as opposed to the submersible pump used in the experiments.

A second simulation was made for the pump running in part load conditions at 55% of Q_{BEP}. The motion of the rag through the pump was slower than observed in the simulation where the pump was running at the best efficiency point. This is a natural consequence of the lower flow rate in part load. However, the simulation did not re-create the motion observed in the experiments with several re-circulations and a tendency to get stuck on the tongue. Similar to the simulation case with the pump running at the best efficiency point, this may be due to the described uncertainties in connection with the boundary conditions, Lagrangian coupling and fluid force modelling using the free stream drag model. Due to the mentioned simplifying assumptions, the presented simulations are preliminary and serve as a proof of concept that the CFD-DEM approach can be used to simulate clogging effects in wastewater pumps.

Summing up, the main contributions of this work are:

- Determination of appropriate initial conditions for simulation of rag transport in wastewater pumps through experimental analysis and image processing.
- Characterisation of the motion of textiles inside a pump at different operating points based on a thorough experimental analysis and subsequent image processing to enable validation of the simulations.
- A textile model and a calibration approach in DEM with separate values for tensile and bending stiffness of the bonds. Using this, the drape of the rag was accurately modelled.
- Coupled CFD-DEM simulations of rag transport through a wastewater pump with results that resembles the recorded motion of rags in experiments when simulating at the best efficiency point of the pump.

These contributions can facilitate further development of CFD-DEM simulation of rag transport in pumping systems, which have the potential to significantly facilitate the design process of wastewater pumps.

6.2 Outlook

Even though the coupled simulations of rag transport presented in this work give results similar to the rag transport observed in experiments, there are issues that should be improved to ensure reliable simulation results.

One disadvantage of the CFD-DEM approach for the present application to model a textile surface is that the fluid force on each particle is determined based on force models. The presented preliminary simulations are made using a free stream drag model for spherical particles as the only fluid force model. This is a coarse simplification. There is a need to improve the coupling between the textile and fluid, possibly by taking into account the angle between the bond between the particles and the flow direction or the overall shape of the rag when modelling the drag on each of the particles.

Additionally, mainly the final static shape of the draping rag was used to evaluate the DEM rag model. However, the dynamics of the model are also very important, and this could therefore be investigated to further validate the model.

When the coupled simulations have been further developed and validated several variations in the simulations are interesting. The influence of the size of the rag and the rag properties on the risk of clogging as well as the influence of the initial conditions would be very interesting to investigate.

Finally, the most interesting perspective and the final long term aim is to use the simulation to identify pump design features that can be changed to reduce the risk of clogging.

References

Aberdeen Group. Simulation driven design benchmark report. Technical report, Aberdeen Group, 2006.

Andersen, L. How grundfos talk lifecycle costs for wastewater pumps. Technical report, GRUNDFOS Holding A/S, 2012.

Ascough, J., Bez, H., and Bricis, A. A simple finite element model for cloth drape simulation. *International Journal of Clothing Science and Technology*, 8(3):59–74, 1996.

Ballhause, D., König, M., and Kröplin, B. *Textile Composites and Inflatable Structures II. Computational Methods in Applied Sciences*, chapter Modelling Fabric-Reinforced Membranes with the Discrete Element Method, pages 51–67. Springer, Dordrecht, 2008.

Bassett, R., Postle, R., and Pan, N. Experimental methods for measuring fabric mechanical properties: A review and analysis. *Textile Research Journal*, 69:866–875, 1999.

Berliner Wasserbetriebe. Dem abwasser auf der spur. `http://www.bwb.de/content/language1/html/991.php`, 2016. Accessed: 2016-05-09.

Bio by Deloitte. Work on preparatory studies for implementing measures of the ecodesign directive 2009/125/ec, ener lot 28 - pumps for private and public wastewater and for fluids with high solids content - task 1-8. Technical report, Working document prepared for European Commission, DG ENER, April 2014.

Bjerg, A., Winther, A., Christoffersen, K., Steenstrup, M., and Noaparast, M. Investigation of the flow in the near-tongue region of a waste water pump. Technical report, December 2016.

Breen, D., House, D., and Wozny, M. A particle-based model for simulating the draping behavior of woven cloth. *Textile Research Journal*, 64(11):663–685, 1994.

Brown, N. *Discrete Element Modelling of Cementitious Materials*. PhD thesis, The University of Edinburgh, 2013.

Brownell, R. and Flack, R. Flow characteristics in the volute and tongue region of a centrifugal pump. ASME 1984 International Gas Turbine Conference and Exhibit, June 4-7 1984.

Chu, C., Cummings, C., and Teixeira, N. Mechanics of elastic performance of textile materials. *Textile Research Journal*, 20(8):539–548, 1950.

Collier, B., Collier, J., Scarberry, H., and Swearingen, A. Development of digital drape tester. *ACPTC Combined Proceedings*, page 35, 1988.

Connolly, R. An experimental and numerical investigation into flow phenomena leading to wastewater centrifugal pump blockage. Master's thesis, Dublin City University, September 2017.

Cundall and Strack. A discrete numerical model for granular assemblies. *Geotechnique*, 29:47–65, 1979.

Cusick, G. The measurement of fabric drape. *The Journal of the Textile Institute*, 59(6): 253–260, 1968.

Davies, J., Butler, D., Small, J., and Sekuloski, V. Gross solids transport and degradation. *Water Science and Technology*, 37(1):61–68, 1998.

Dietzel, M. and Sommerfeld, M. Numerical calculation of flow resistance for agglomerates with different morphology by the lattice-boltzmann method. *Powder Technology*, 250:122–137, 2013.

DIN 53362:2003-10. Prüfung von kunststoff-folien und von textilen flächengebilden (ausser vliesstoffe), mit oder ohne deckschicht aus kunststoff - bestimmung der biegesteifigkeit (din 53362:2003-10). Technical report, DIN Deutsches Institut für Normung e.V., October 2003.

Eberhardt, B., Weber, A., and Strasser, W. A fast, flexible, particle-system model for cloth draping. *Computer Graphics in Textiles and Apparel*, 16(5):52–59, 1996.

Flygt. Wastewater pump clog resistance cannot be determined by throughlet size. Technical report, Xylem Inc., 2012.

Friedler, E., Brown, D., and Butler, D. A study of wc derived solids. *Water Science and Technology*, 33:17–24, 1996.

Ganser, G. A rational approach to drag prediction of spherical and non-spherical particles. *Powder Technology*, 77:143–152, 1993.

Gerlach, A., Wulff, S., Perlitz, D., Lykholt-Ustrup, F., and Thamsen, P. The optimal vortex pump impeller - an experimental study on clogging behaviour. In *Proceedings of 12th European Conference on Turbomachinery Fluid dynamics and thermodynamics*, April 3-7 2017.

Gerlach, S., Ugarelli, R., and Thamsen, P. Case study on the functional performance of a large wastewater pumping station. In *International Symposium on Transport Phenomena and Dynamics of Rotating Machinery*, April 10-15 2016.

Ghosh, T. and Zhou, N. Characterisation of fabric bending behaviour: A review of measurement principles. *Indian Journal of Fibre & Textile Research*, 28:471–476, 2003.

Guo, Y., Curtis, J., Wassgren, C., Ketterhagen, W., and Hancock, B. Granular shear flows of flexible rod-like particles. In *Powders and Grains*, AIP Conference Proceedings, pages 491–494, 2013a.

Guo, Y., Wassgren, C., Hancock, B., Ketterhagen, W., and Curtis, J. Validation and time step determination of discrete element modelling of flexible fibers. *Powder Technology*, 249(2013):386–395, 2013b.

Hobbs, A. Simulation of an aggregate dryer using coupled cfd and dem methods. *International Journal of Computational Fluid Dynamics*, 23(2):199–207, 2009.

Höchel, K., Thamsen, P., and Rauwald, H. Problem analysis of sewage pumping stations. *International Rotating Equipment Conference, Düsseldorf*, 2012.

House, D. and Breen, D. *Cloth Modeling and Animation*. AK Peters, Ltd., 2000. ISBN: 9781439863947.

ISO 139:2005. Textilen - normalklimate für die probenvorereitung und prüfung (iso 139:2005 + amd. 1:2011); deutche fassung en iso 139:2005 + a1:2011. Technical report, European Committee for Standardization, October 2011.

ISO 9073-9:2009. Textilen - prüfverfahren für vliesstoffe - teil 9: Bewertung des textilen falls einschliesslich des fallkoeffizienten (iso 9073-9:2009); deutsche fassung en iso 9073-9:2008. Technical report, European Committee For Standardization, March 2008.

Isono, M., Nohmi, M., Uchida, H., Kawai, M., Kudo, H., Kawahara, T., Miyagawa, K., and Saito, S. An experimental study on pump clogging. *IOP Conference Series: Earth and Environmental Science*, 22:012009, 2014.

Jensen, A., Gerlach, S., Lykholt-Ustrup, F., Sørensen, H., Rosendahl, L., and Thamsen, P. Investigation of the influence of operating point on the shape and position of textile material in the inlet pipe to a dry-installed wastewater pump. In *Proceedings of ASME 2017 Fluids Engineering Division Summer Meeting*, July 31-August 3 2017.

Jeong, Y. A study of fabric-drape behaviour with image analysis part 1: Measurement, characterisation and instability. *The Journal of The Textile Institute*, 89(1):59–69, 1998.

Jeong, Y. and Phillips, D. A study of fabric-drape behaviour with image analysis part 2: The effects of fabric structure and mechanical properties on fabric drape. *The Journal of The Textile Institute*, 89(1):70–79, 1998.

Katscher, B. Textilen im abwasser - bestandsanalyse und erstellung eines lastenheftes für die zugfestigheitsprüfung im feuchten zustand von feuchttüchern. Technical report, Hochschule für Technik und Wirtschaft Berlin, Fachbereich Gestaltung und Kultur, Studiengang Bekleidungstechnik/Konfektion, 2016.

Kenkare, N. and Plumlee, T. Evaluation of drape characteristics in fabrics. *International Journal of Clothing Science and Technology*, 17(2):109–123, 2005.

Korving, H., Clements, F., and van Noortwijk, J. Statistical modeling of the serviceability of sewage pumps. *Journal of Hydraulic Engineering*, 132:1076–1085, 2006.

Lindström, S. and Uesaka, T. Simulation of the motion of flexible fibers in viscous fluid flow. *Physics of Fluids*, 19(11):113307, 2007.

Lommen, S., Schott, D., and Lodewijks, G. Dem speedup: Stiffness effects on behavior of bulk material. *Particuology*, 12:107–112, 2014.

McEvoy, R. *Innovative Development of Single-Blade-Impeller Hydraulics for Wastewater Application*. PhD thesis, University of Limerick, 2011.

Mitchell, R.-L., Gunkel, M., Waschnewski, J., and Thamsen, P. Investigations into wastewater composition focusing on nonwoven wet wipes. *Technical Transactions*, 1: 125–135, 2017.

Mitchell, R.-L., Gunkel, M., Thamsen, P. U., and Waschnewski, J. Investigations into wastewater composition focusing on nonwoven wet wipes. *Water Convention, Singapore International Water Week*, July 2016.

Ng, H. and Grimsdale, R. Computer graphics techniques for modeling cloth. *Computer Graphics in Textiles and Apparel*, 16(5):28–41, 1996.

Niessen, W. and Chansky, S. The nature of refuse. In *Proceedings of National Incinerator Conference, New York*, 1970.

Peirce, F. The handle of cloth as a measurable quality. *J. Text. Inst.*, 21(9):T377–T416, 1930.

Plaut, R. Formulas to determine fabric bending rigidity from simple tests. *Textile Research Journal*, 85(8):884–894, 2015.

Pöhler, M., Gerlach, S., Höchel, K., Mengdehl, T., and Thamsen, P. Linking efficiency to functional performance by a pump test standard for wastewater pumps. In *ASME/JSME/KSME 2015 Joint Fluids Engineering Conference, Seoul, South Korea*, July 26-31 2015 2015.

Potyondy, D. and Cundall, P. A bonded particle model for rock. *Int. J. Rock Mech. Min. Sci.*, 41:1329–1369, 2004.

Provot, X. Deformation constraints in a mass-spring model to describe rigid cloth behaviour. In *Proceedings of Graphics Interface '95*, Proceedings of Graphics Interface '95, pages 147–154, May 17-19 1995.

Sanad, R., Cassidy, T., and Cheung, V. Fabric and garment drape measurement - part 1. *Journal of Fiber Bioengineering & Informatics*, 5(4):341–358, 2012.

Schmid, C., Switzer, L., and Klingenberg, D. Simulations of fiber flocculation: Effects of fiber properties and interfiber friction. *Journal of Rheology*, 44(4):781–809, 2000.

Sommerfeld, M. and Stübing, S. A novel lagrangian agglomerate structure model. *Powder Technology*, 319:34–52, 2017.

Specklin, M., Albadawi, A., Connolly, R., Breen, B., and Delaure, Y. A coupled lattice boltzmann - immersed boundary method to model the behaviour of thin flexible structures in fluids. In *13th International Conference on Heat Transfer, Fluid Mechanics and Thermodynamics*, 2017.

Spence, K., Digman, C., Balmforth, D., Houldsworth, J., Saul, A., and Meadowcroft, J. Gross solids from combined sewers in dry weather and storms, elucidating production, storage and social factors. *Urban Water Journal*, 12:773–789, 2016.

Sørensen, H. and Jensen, A. Visualization of the motion of textiles through a waste water pump at different operating points. *Journal of Flow Control, Measurement and Visualization*, 2017.

Sze, K. and Liu, X. A new skeletal model for fabric drapes. *International Journal of Mechanics and Materials in Design*, 2:225–243, 2005.

Teng, J., Chen, S., and Hu, J. A finite-volume method for deformation analysis of woven fabrics. *International Journal for Numerical Methods in Engineering*, 46:2061–2098, 1999.

Thamsen, P. Cutting clogging in wastewater. *World Pumps*, April:22–25, 2009.

TU Berlin, Chair of Fluid System Dynamics. Images of materials from the mechanical cleaning stage in wastewater plants, clogged impeller and example of wet wipes found in wastewater samples.

Vangheluwe, L. and Kiekens, P. Time dependence of the drape coefficient of fabrics. *International Journal of Clothing Science and Technology*, 5(5):5–8, 1993.

Vassiliadis, S., Kallivretaki, A., Domvoglou, D., and Provatidis, C. *Advances in Modern Woven Fabrics Technology*, chapter Mechanical Analysis of Woven Fabrics: The State of the Art, pages 41–64. InTech, 2011. ISBN: 978-953-307-337-8.

Vidal-Salle, E. and Boisse, P. *Modelling and predicting textile behaviour*, chapter Modelling the structures and properties of woven fabrics, pages 144–155. Woodhead Publishing Limited, The Textile Institute, 2010. ISBN: 978-1-84569-721-1.

Wang, X., Liu, X., and Hurren, C. *Fabric Testing*, chapter Physical and Mechanical Testing of Textiles, pages 90–124. Woodhead Publishing Ltd, 2008.

Wang, Y. and Guo, W. W. *Rock Anisotropy, Fracture and Earthquake Assessment*, chapter Reproducing the Realistic Compressive-tensile Strength Ratio of Rocks using Discrete Element Model, pages 142–174. De Gruyter, 2016.

Wu, Z., Au, C., and Yuen, M. Mechanical properties of fabric materials for draping simulation. *International Journal of Clothing Science and Technology*, 15(1):56–68, 2002.

Yamamoto, S. and Matsuoka, T. A method for dynamic simulation of rigid and flexible fibers in a flow field. *The Journal of Chemical Physics*, 98(1):644–650, 1993.

Part II

Appendices

Appendix 1

Time Step and Particle Size Independence Analyses

The DEM model of the rag should be independent of the discretization and a time step must be chosen so the solution is time step independent. Since the bond stiffness parameters are adapted based on the particle size, the influence of the particle size on the elongation and bending properties of the rag model should be limited. This is investigated in the following. The particle sizes used in this analysis are r_{p} = [0.5, 1.0, 1.5, 2.0, 2.5] mm. All simulations use a fixed time step. The density of the particles has been scaled with the particle radius to ensure equal mass per unit area for rags of different discretizations.

1.1 Simulation of Bond Elongation

Recall the simulation case described in Subsection 3.3.1. This simulation case had two particles with a force of same magnitude but opposite direction acting on the two, and it was based on the breaking strength and elongation test in Chapter 2. The simulation is repeated with different particle radii, r_{p} = [0.5, 1.0, 1.5, 2.0, 2.5] mm, and a variation of time step sizes. Figure 1.1 to the left illustrates the deviation in the final strain as the time step size is varied between 0.001 µs and 50 µs for the five different particle radii. It is seen that the final strain is larger at higher time steps but decreases and reaches time step independence. The larger the particle and bond radius the higher the time step is possible. The stiffness of the bonds is adapted when the particle radius is changed. With this adjustment, the strain is kept constant as the particle size is changed. Since an increase in the particle radius entails that each particle constitute a larger part of the rag, the force applied on the particles is also scaled with the particle size. Figure 1.1 to the right shows

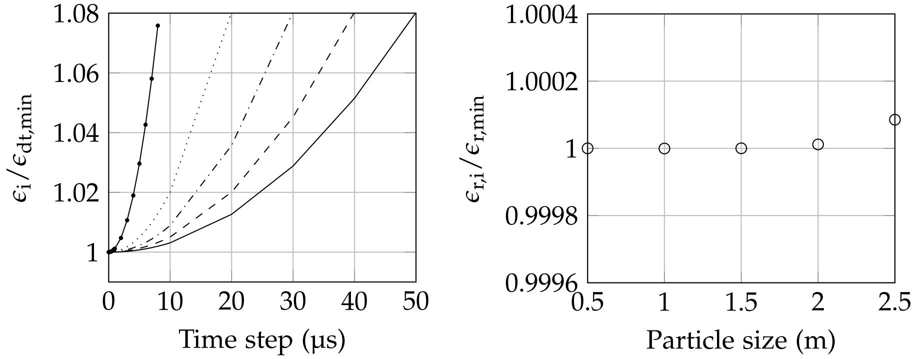

Fig. 1.1: Left: The deviation in the final strain between the smallest time step and larger time steps. The larger the particles, the higher the time step is possible before the deviation becomes significant. · · · · $r = 1$ mm, · — ·— $r = 1.5$ mm, — — — $r = 2.0$ mm, —— $r = 2.5$ mm. Right: Deviation in final strain as function of the particle size, using a particles of radius 0.5 mm as reference.

the strain divided by the strain at the smallest particle radius. As seen in the figure the strain is independent of the particle size with a deviation of less that 0.02% between the smallest to the largest particle.

1.2 Simulation of Bending Fibre

The bending stiffness $S_{n,b}$, which has been introduced in the present work, was calibrated based on simulations of the deflection of a bending fibre of particles as described in Subsection 2.2.2. This simulation is repeated for different time step sizes to investigate the influence of the time step on the final deflection of the bending fibre. The analysis is made for a fibre of 11 bonded particles with a radius of 1.5 mm. The result is presented in Figure 1.2. It is seen in the figure that the final deflection is very similar for all time steps and the deviation between the minimum and maximum deflection is less than 1%. Therefore, the result of the bending simulation is considered independent of the time step using a time step of 10 µs or smaller.

The bending stiffness $S_{n,b}$ must be re-calibrated if the particle- and bond radii change. The calibration has been done for particle radii of r_p = [0.5, 1.0, 1.5, 2.0, 2.5] mm. Figure 1.3 illustrates the resulting $S_{n,b}$ as function of the particle radius. As seen in the figure, the bending stiffness decreases as the radius of the bond increases.

Using the calibrated value of the bending stiffness $S_{n,b}$ for the different particle sizes, the bending of fibres of different discretisations are shown in Figure 1.4. The figure to the left presents the results of simulations repre-

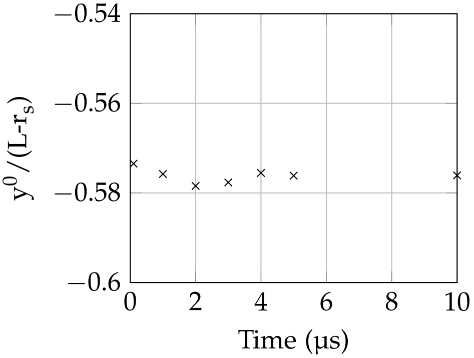

Fig. 1.2: Left: Final bending deflections using time step sizes between 0.1 µs and 10 µs for a fibre of 11 particles of radius 1.5 mm.

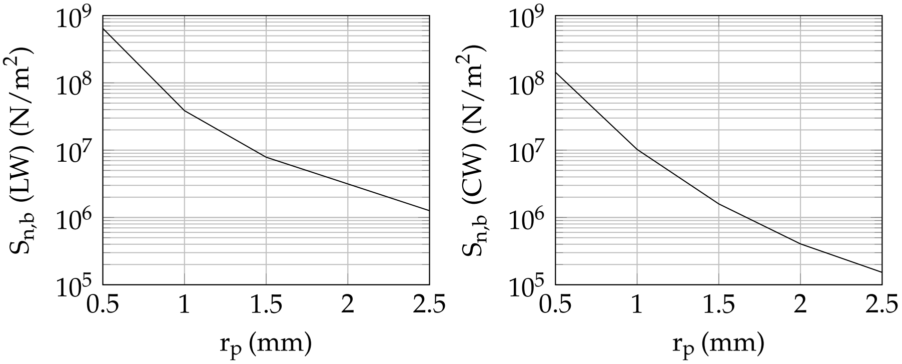

Fig. 1.3: $S_{n,b}$ for the lengthwise (left) and crosswise (right) direction to ensure a bending deformation corresponding to the bending deformation found in the experiment.

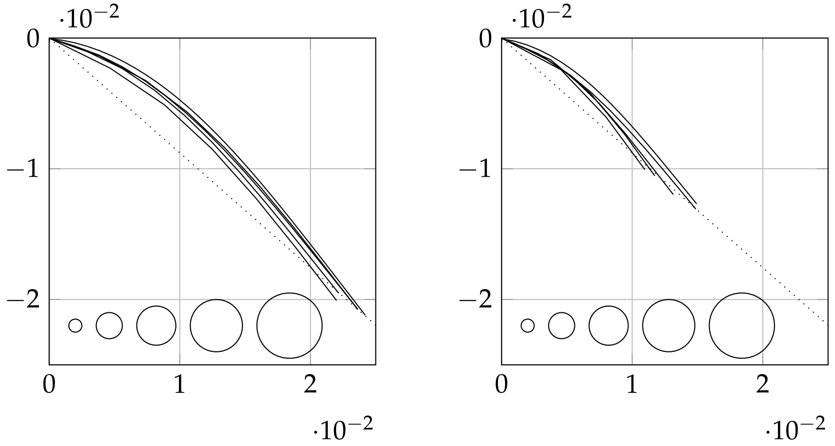

Fig. 1.4: Bending fibres with different discretisations and the calibrated values of normal bending stiffness $S_{\mathrm{n,b}}$. Left: lengthwise, Right: crosswise.

senting the lengthwise direction of the rag with a sample length of 3.4 cm. The figure to the right is a result of simulations representing the crosswise direction of the rag with a sample length of 2.1 cm (see Table 2.3). It is seen that the lengths of the fibres deviate slightly from particle size to particle size. This is due to the discrete nature of the fibre of particles, which means that the lengths of 2.1 cm and 3.4 cm can not be exactly recreated for all particle sizes. The fibre and the fibres consist of 4-34 particles and the five particles sizes are sketched in the bottom of the figures. Based on Figure 1.4, the bending is considered adequately independent of the particle size for the present purpose.

1.3 Simulation of Draping Rag

Simulations of a circular rag samples draping over a circular disk were used to calibrate the value of the tangential bond stiffness S_{t}. Similar to the elongation and bending simulations, the drape simulation was repeated with different particle sizes. Figure 1.5 illustrates the outline of draping rags with different values of the tangential bond stiffness S_{t}. The particles forming the rags have radius of 2.0 mm. As seen in the figure, the area of the draping rag increases as the tangential stiffness increases. Furthermore, the overall shape of the draping rag changes significantly with the tangential stiffness. In the figure, the inner circle is the disc the rag is draping over. The dotted circles are the minimum and maximum size of the drape waves obtained during experiments and the dashed line is the mean size of the drape waves in the experiments. It is seen that the size of the drape waves is realistic

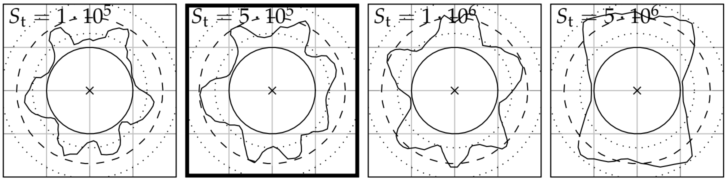

Fig. 1.5: Draping cloth consisting of particles with r_p = 2.0 mm.

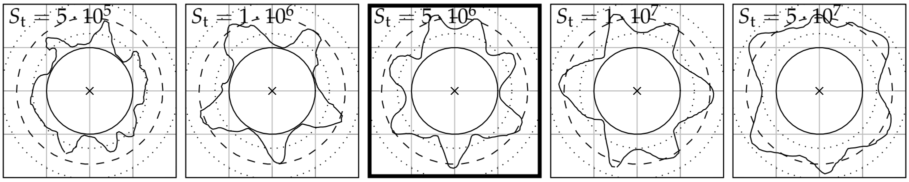

Fig. 1.6: Draping cloth consisting of particles with r_p = 1.0 mm.

for a tangential stiffness between $1 \cdot 10^5$ N/m^3 and $1 \cdot 10^6$ N/m^3 with sizes of the drape waves close to the mean size from the experiments. Based on the size of the drape waves and the drape area, the result marked with the thick square is the result closest to the experimental results, and therefore a tangential stiffness of $5 \cdot 10^5$ N/m^3 is chosen for the particle radius of 2 mm.

Figure 1.6 illustrates the same result for a rag consisting of particles with r_p = 1.0 mm. Similar to the case with a particle radius of 2 mm, the size of the drape waves produced in the simulation is realistic for more of the cases with different values of the tangential stiffness S_t. Comparing Figure 1.5 and Figure 1.6, it is clear that the tangential stiffness needed to create a realistic drape increases as the radius of the particles decreases. Based on the size of the drape waves and the drape area, the result marked with the thick square is the result closest to the experimental results, and therefore a tangential stiffness of $5 \cdot 10^6$ N/m^3 is chosen for the particle radius of 1 mm.

The change in area and drape wave size as function of the tangential stiffness is presented in Figure 1.7. The figure to the left shows the result for a particle radius of 1 mm, while the figure to the right shows the result for a particle radius of 2 mm. As seen in the figure, the lowest value of the tangential stiffness S_t in both cases underestimates both the size of the drape waves and the drape area. In both cases the tangential stiffness resulting in the smallest deviation in drape wave size and drape area is chosen. As marked in Figure 1.5, this results in a tangential stiffness S_t of $5 \cdot 10^5$ N/m^3 for a particle radius of 2 mm. A this tangential stiffness the simulation overestimates the drape area with 7% and underestimates the size of the drape waves with 2%. For particles of radius 1 mm, a tangential stiffness of $5 \cdot 10^6$

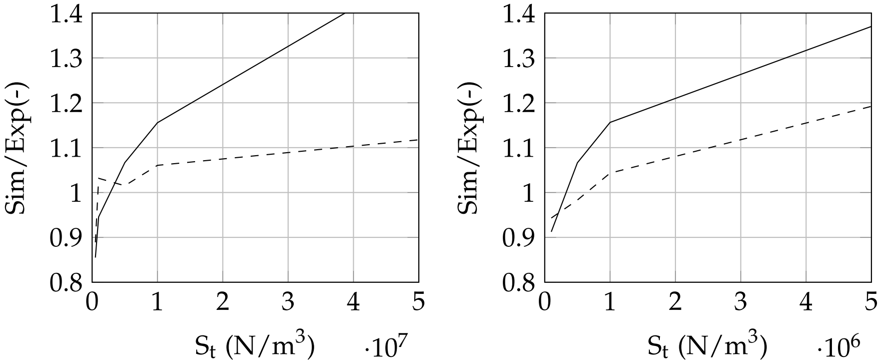

Fig. 1.7: Deviation between the size of the drape waves and the drape area found experimentally and by simulation with $r_\mathrm{p} = 2.0$ mm as function of the value of $\mathrm{S_t}$. − − − size of drape waves, ——- drape area.

N/m^3 leads to the smallest deviation between simualtion and experiment. At this tangential stiffness the simulation overestimates the drape area with 7% and the size of the drape waves with 2%.

Figure 1.8 illustrates the drape area and the size of the drape waves as function of the tangential stiffness for three different particle sizes of r_p = [1.0, 1.5, 2.0] mm. As seen in the figure, the size of the drape waves is less sensitive to the tangential stiffness than the area, and the deviation between the size of the drape waves in the experiments and the simulation is generally lower than the deviation in drape area. Furthermore, it is clear from Figure 1.8 to the left, that the tangential stiffness of the bonds should decrease as the bond radius increases.

Figure 1.9 and 1.10 illustrates the dynamics of the drape simulation from the initial condition with the rag placed above the disc to the final drape after 2.5 seconds for particle radii of 1 mm and 2 mm respectively.

The drape of the rags with different discretizations and calibrated values of the tangential stiffness S_t is compared in Figure 1.11. The outlines of the drape have similar characteristics in the three cases, with similar size of drape waves and drape area. The number of drape waves varies between 6 and 7, which is realistic with a mean number of drape waves in the experiments of 6.4. Furthermore, the size of the drape waves deviates with around 2% from the experiments in all cases while the drape area deviates between 1% an 7% from the experiments in the three cases. The determined properties of the bonds are summarised in Table 3.3, 3.4 and 3.5.

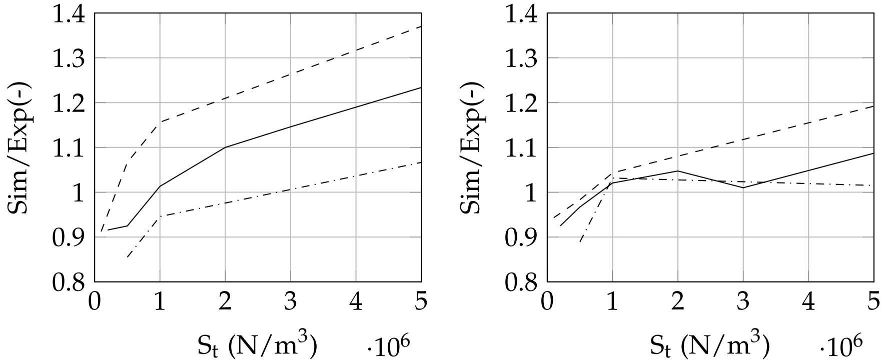

Fig. 1.8: Comparison between experiments and simulations of drape. The drape area and the size of the drape waves as function of the tangential bond stiffness S_{t} for different particle radii. — — — r_{p} = 1.0 mm, —— r_{p} = 1.5 mm, · — · — · r_{p} = 1.5 mm

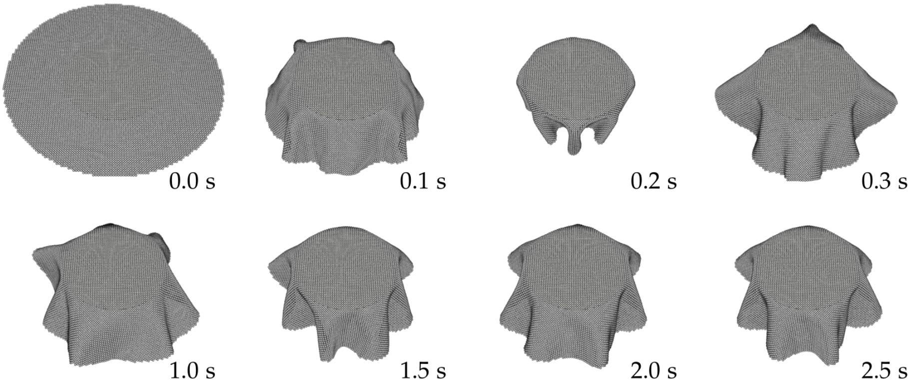

Fig. 1.9: Drape over time of a rag model with particles of radius 1 mm.

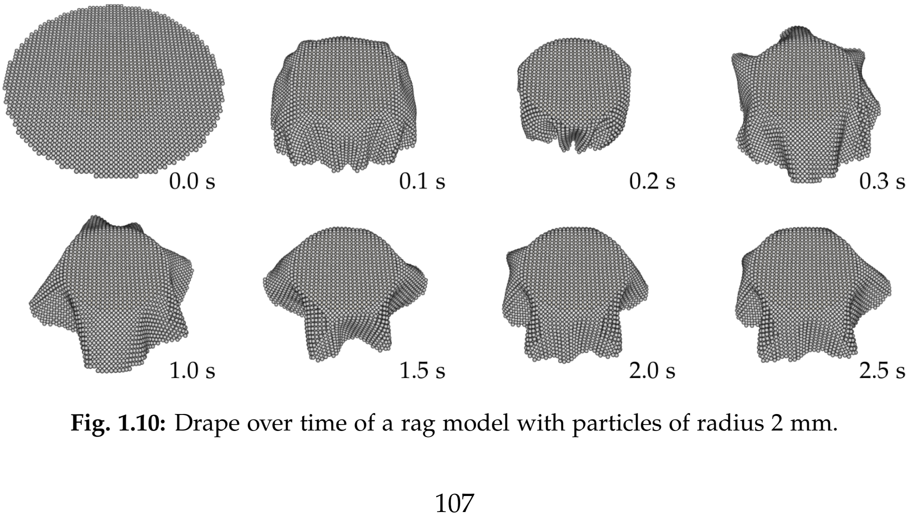

Fig. 1.10: Drape over time of a rag model with particles of radius 2 mm.

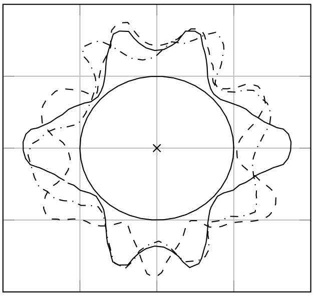

Fig. 1.11: Comparison of the drape with different discretizations of the rag. The circle shows the disc the rag is draping over, — — — r_p = 1 mm, —— r_p = 1.5 mm, · — · — · r_p = 2 mm

1.4 Influence of Damping

In order to improve the stability of the textile model to handle the harsh conditions inside a pump a build-in damping coefficient or rotation friction coefficient can be applied in the bond model.

The damping coefficient in the 'updated bond model' in the DEM software EDEM is based on Guo et al. (2013a). The normal and tangential force after damping a determined using Eq. (1.1) and (1.2) respectively.

$$\boldsymbol{F}_{\mathrm{d,n}} = \boldsymbol{v}_{\mathrm{n}} \cdot c_{\mathrm{d}} \cdot \sqrt{S_{\mathrm{n}} \cdot A_{\mathrm{b}} \cdot 2.0 \cdot m_{\mathrm{eqm}}} \tag{1.1}$$

$$\boldsymbol{F}_{\mathrm{d,t}} = \boldsymbol{v}_{\mathrm{t}} \cdot c_{\mathrm{d}} \cdot \sqrt{S_{\mathrm{t}} \cdot A_{\mathrm{b}} \cdot 2.0 \cdot m_{\mathrm{eqm}}} \tag{1.2}$$

In these equations $\boldsymbol{v}_{\mathrm{n}}$ is the relative velocity in the normal direction and $\boldsymbol{v}_{\mathrm{t}}$ is the relative velocity in the tangential direction, c_{dp} is the damping coefficient. The determined values of $\boldsymbol{F}_{\mathrm{d,n}}$ and $\boldsymbol{F}_{\mathrm{d,t}}$ are used to determine a total force on the bonds as given in Equation (1.3) and (1.4).

$$\boldsymbol{F}_{\mathrm{t,n}} = \boldsymbol{F}_{\mathrm{b,n}} - \boldsymbol{F}_{\mathrm{d,n}} \tag{1.3}$$

$$\boldsymbol{F}_{\mathrm{t,t}} = \boldsymbol{F}_{\mathrm{b,t}} - \boldsymbol{F}_{\mathrm{d,t}} \tag{1.4}$$

$\boldsymbol{F}_{\mathrm{t,n}}$ is the force in the bond normal direction after damping has been included, $\boldsymbol{F}_{\mathrm{b,n}}$ is the determined bond force in the normal direction before damping and $\boldsymbol{F}_{\mathrm{d,n}}$ is the damping force in the normal direction. Similarly, $\boldsymbol{F}_{\mathrm{t,n}}$ is the force in the bond tangential direction after damping has been included, $\boldsymbol{F}_{\mathrm{b,n}}$ is the determined bond force in the tangential direction before damping and $\boldsymbol{F}_{\mathrm{d,n}}$ is the damping force in the tangential direction.

Figure 1.12 shows how even high values of the drape coefficient only have a very limited influence on the final static drape of the rag. Therefore, a

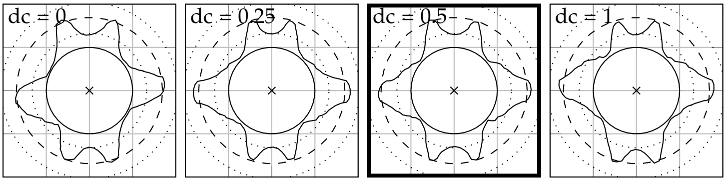

Fig. 1.12: Piece of textile draping over cylinder. The particles forming the piece of textile have a radius of 1.5 mm. The damping coefficient is varied from 0 to 1, without any significant change in the final shape of the draping textile.

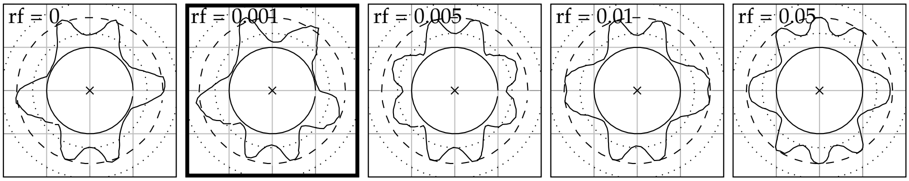

Fig. 1.13: Piece of textile draping over cylinder. The particles forming the piece of textile have a radius of 1.5 mm. The rotation friction coefficient is varied from 0 to 0.05, which changes the final shape of the draping textile significantly.

damping coefficient on the bonds of 0.5 have been used in all further simulations.

The rotational friction is implemented as presented in Equation (1.5) and (1.6).

$$\boldsymbol{M}_1 = |-\boldsymbol{F}_{\mathrm{t,n}}| \cdot r_{\mathrm{p,1}} \cdot c_{\mathrm{r}} \tag{1.5}$$

$$\boldsymbol{M}_2 = |-\boldsymbol{F}_{\mathrm{t,n}}| \cdot r_{\mathrm{p,2}} \cdot c_{\mathrm{r}} \tag{1.6}$$

Here, c_{r} is the rotation friction coefficient, $F_{\mathrm{t,n}}$ is the total force in the normal direction.

Figure 1.13 illustrates how rotation friction influences the final static drape of a simulated rag. It is seen in the figure that even small values of the rotation friction coefficient significantly influences the result. A rotational friction of 0.001 is used in all further simulations.

Appendix 1. Time Step and Particle Size Independence Analyses

Part III

Papers

Paper A

Characterisation of Textile Shape and Position Upstream of a Wastewater Pump under Different Part Load Conditions

Anna Lyhne Jensen, Henrik Sørensen, Lasse Rosendahl and
Paul Uwe Thamsen

The paper has been published in *Urban Water Journal*, 2017,
https://doi.org/10.1080/1573062X.2017.1414274

Characterisation of Textile Shape and Position Upstream of a Wastewater Pump under Different Part Load Conditions

Anna Lyhne Jensen[a], Henrik Sørensen[a], Lasse Rosendahl[a], Paul Uwe Thamsen[b]

[a] *Aalborg University, Department of Energy Technology, Pontoppidanstræde 111, DK-9220 Aalborg, Denmark*
[b] *Technical University of Berlin, Department of Fluid System Dynamics, Straße des 17. Juni 135, D-10623 Berlin, Germany*

Abstract

Accumulations of sanitary textile materials often lead to clogging of pumps in the wastewater system. Simulation of clogging phenomena may help to identify means of reducing the risk of clogging. In order to provide realistic initial conditions for clogging simulations, this study characterises textiles in artificial wastewater in the suction pipe to a dry-installed pump at nine different operating points. The textiles are recorded approximately 3.5 pipe diameters from the pump inlet and approximately three pipe diameters from the suction pipe bend at pipe Reynolds numbers in the range 300,000–900,000. Parameters of position, orientation, elongation and projected two-dimensional (2D) area are extracted using image analysis. The resulting parameters from the different operating points are compared using analysis of variance. The results show that the position, orientation and elongation do not change significantly with the operating point, while the projected 2D area decreases with an increased flow.

Keywords: wastewater; pumps; image processing

A.1 Introduction

Extensive sewer networks of channels, pressure pipes and pumping stations, transporting wastewater from e.g. sinks, washing machines and toilets to wastewater treatment plants, are crucial for modern metropolises. However, the reliable operation of the sewer system is challenged by a high content of sanitary refuse, commonly entering the sewer system through toilets. Due to the lack of significant degradation of these solids, they tend to accumulate, causing risk of blockages in drainage and clogging in wastewater pumps.

Therefore, a very important parameter in the development of new wastewater pump designs is their ability to handle these objects without clogging. The resistance to clogging is currently tested experimentally. However, the industry is moving towards simulation driven development, which requires the ability to simulate clogging phenomena. One of the first steps to accomplish this complex simulation is to establish how to represent the sanitary refuse based on the composition of wastewater and to determine valid initial conditions for the sanitary objects. The composition of solids in wastewater has been investigated by various authors during the last several decades, using questionnaires about refuse habits and analysing samples of wastewater (Friedler et al., 1996; Niessen and Chansky, 1970). Recently, Spence et al. (2016) presented the daily variations of different sanitary items in three different catchment areas and found that the most common sanitary item in the wastewater in the investigated areas was wet wipes. Mitchell et al. (2017) also investigated the content of wastewater based on samples and found that textiles constituted around 33% of the samples. These studies indicate that wet wipes constitute a significant amount of the solids content in wastewater.

The motion of textile material, like wet wipes, has been studied in partially filled pipe networks in order to understand the impact of decreasing the flush volume of toilets. Littlewood and Butler (2003) investigated the movement mechanisms and behaviour of gross solids in small pipes with intermittent flow, as the solids are transported by toilet flushing. They identified three mechanisms of movement, the solid moving down the pipe only during a flush, the solid sliding down the pipe with water building up behind the solid, and a combination of the two. Similarly, McDougall and Wakelin (2007) and Walski et al. (2011) investigated transport of large deformable solids and also identified three movement mechanisms. Common for the investigations is the focus on the velocity of the solids compared to the velocity of the fluid as well as on the solid transport distance. These properties, along with knowledge of the amount of flushed material, are important in the development of models of the pollutant storage rates and models of solid transport in sewers. Unlike the mentioned studies, the present work analyses the sanitary material directly upstream of a wastewater pump.

Wastewater pumps are either submersible or dry-installed. The water inflow depends on the type of pump installation since the wastewater enters a dry-installed pump through a suction pipe, while it enters submersible pumps directly from the pump sump. The present work characterises a standard piece of non-woven textile in the suction pipe upstream of a dry-installed pump through parameters as textile area m_{00}, Y position of the centroid, the orientation θ and an elongation ratio ϵ. Furthermore, the influence of the pump operating point on these parameters is investigated, since the type of clogging in the pump has proven to depend on the operating point (Thamsen, 2009). This analysis has an aim to determinate appropriate initial

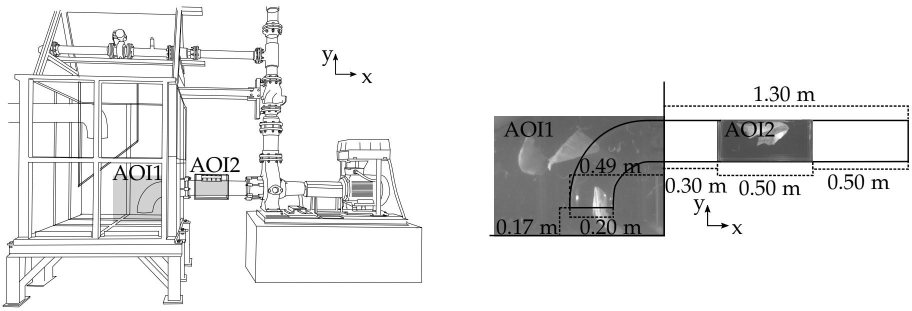

Fig. A.1: a) Sketch of the scaled pumping station with a dry installed pump. The grey areas mark the two areas of interest, AOI1 and AOI2, b) Simplified sketch of the suction pipe. AOI1 and AOI2 are the two areas of interest. L and R mark the left and the right part of the suction pipe

conditions for textiles in clogging simulations.

A.2 Experimental Approach

A scaled pumping station (1:3) with a dry-installed pump is located in the Department of Fluid System Dynamics in TU Berlin. The test rig is sketched in Figure A.1(a) and includes a pump sump and a suction pipe in acrylic glass, which enables recording of the textile in these areas. Two areas of interest are marked with grey in Figure A.1(a) and illustrated in more detail in Figure A.1(b). The first area of interest (AOI1) is in the pump sump at the inlet to the suction pipe. The second area of interest (AOI2) is covering 0.5 m of the horizontal part of the suction pipe 0.5 m upstream of the inlet to the pump. A box of acrylic glass of size 0.50 m × 0.36 m × 0.32 m was fixed around the circular suction pipe at AOI2. The box is filled with water to decrease the distortion of light through the circular surface of the pipe. Using the box, the distortion of light is negligible. The water in the system is pumped from the pump sump to a smaller tank from where it flows back into the pump sump. A plate is placed in the pump sump as sketched in Figure A.1(a), to decrease the amount of air-bubbles appearing in the images. Two cameras recording AOI1 and AOI2 were synchronized and images taken at the same time were given the same name. This means that the connection between the motion of the pieces of textile in the suction sump and inside the suction pipe can be analysed. The cameras used for recording AOI1 and AOI2 were Basler acA1300–30um (1.3 MP) and Basler acA1920–155um (2.3 MP), respectively. AOI1 covers 850 mm × 635 mm and was recorded with a framerate of 30 fps. AOI2 covers 520 mm × 225 mm and was recorded with a frame rate of 150 fps.

	800 RPM	985 RPM	1200 RPM
Q_f (m^3/h)	170	256	341
v_f (m/s)	1.50	2.26	3.01
v_t (m/s)	1.53	2.25	2.87
Q_f (m^3/h)	210	315	420
v_f (m/s)	1.86	2.79	3.71
v_t (m/s)	1.87	2.79	3.52
Q_f (m^3/h)	256	384	512
v_f (m/s)	2.26	3.40	4.53
v_t (m/s)	2.27	3.40	4.28

Table A.1: Volume flow, Qf flow velocity, vf, and textile velocity, vt. The velocity of the textile is based on image analysis of images from AOI2 Operating point 50% of BEP 75% of BEP 100% of BEP

The tests were done at three different impeller speeds and at the best efficiency point (100% BEP), part load (75% BEP), and heavy part load (50% BEP) for each impeller speed. This results in tests at the nine different operating points listed in Table A.1. Volume flows, Q_f, in the range of 170 to 512 m^3/h, led to Reynolds numbers in the order of 300,000 to 900,000 based on the inner diameter of the suction pipe. The velocity of the fluid v_f was in the range from 1.50 to 4.53 m/s based on volume flow and suction pipe cross-sectional area. The velocity of the textile, v_t, in the pipe was in the range 1.53 to 4.28 m/s. This range is found based on image analysis of the acquired images. It is seen that the velocities of the fluid and textile are very similar, which is expected due to very similar densities of the wet textile and the water.

Because of hygienic issues, and to create better optical access, artificial wastewater is commonly used in clogging tests. The artificial wastewater is created using clean water with an addition of solids commonly found in wastewater. Due to large variations in the solids content in wastewater, caused by different habits of flushing refuse from country to country and from catchment area to catchment area as well as the influence of e.g. the weather and the network operation, there is no clear general characterisation of the solids composition in wastewater. However, a definition of standard wastewater would ease the evaluation of the ability of wastewater pumps to handle solids in wastewater. Thamsen (2009) used Aro super dust cloths made for household cleaning, which are similar to the wet wipes found in wastewater, to create artificial wastewater and evaluate how the type of clogging depends on the pump operating point. The same type of dust cloths has since been used in several experimental investigations in TU Berlin as a part of a work to define a test standard for wastewater pumps (Pöhler et al., July 26-31 2015). In the present experiments the artificial wastewater is created us-

Property	Value
Structure	Non-woven
Size	220 mm × 300 mm
Thickness	0.77 mm
Fibre composition	90% polyester, 10% polypropylene
Mass per area (dry)	60 g/m2

Table A.2: Characteristics of the dust cloth used to create artificial wastewater

ing clean water and 20 of the mentioned dust cloths. These are commercially available and the properties are specified in Table A.2. The dust cloths have proven to recreate the different types of clogging caused by real wastewater (Thamsen, 2009). The dust cloths were left in water for 24 hours before each test to ensure they were fully soaked with water.

Using only 20 dust cloths in each test, allows the dust cloths to be observed one at the time and limits the changes in operating point due to accumulation of the dust cloths inside the pump. The tests are run until the visual appearance of the dust cloths becomes worn or until all dust cloths have accumulated inside the pump, meaning that no more dust cloths are being circulated back to the pump sump to be recorded again. The tests are repeated 5–8 times per operating point to achieve a satisfactory amount of data, resulting in an average of 236 dust cloths per operating point. In total 60 separate tests were made and a total of 2123 dust cloths were recorded as they passed through the suction pipe. The final data-set consisted of more than three million pictures with and without dust cloths.

A.3 Image Processing

The acquired images are processed using an in-house code in MATLAB developed for the purpose. The code identifies the pictures containing dust cloths and determines the parameters needed for the analysis. These parameters are sketched in Figure A.2 and are the textile area m_{00}, vertical position Y, elongation ratio ϵ, and orientation θ.

Figure A.3 shows three main steps of the image processing. Figure A.3(a) is an example of an original image from AOI2. Figure A.3(b) shows this image after the average background has been subtracted. Since the lighting in the test hall changed during the day, the average background was identified for each of the 60 tests. After background subtraction the grey scale image is converted to a binary image using a threshold value. An appropriate threshold value ensures that the pixels representing the dust cloth are converted to one and the value of the pixels representing the background is converted

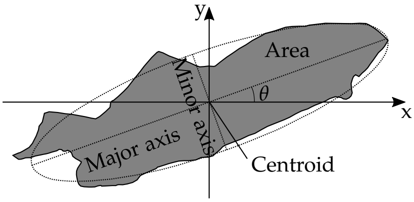

Fig. A.2: Sketch of the parameters analyses in the images. The ellipse has the same second order moment as the blob formed by the dust cloth

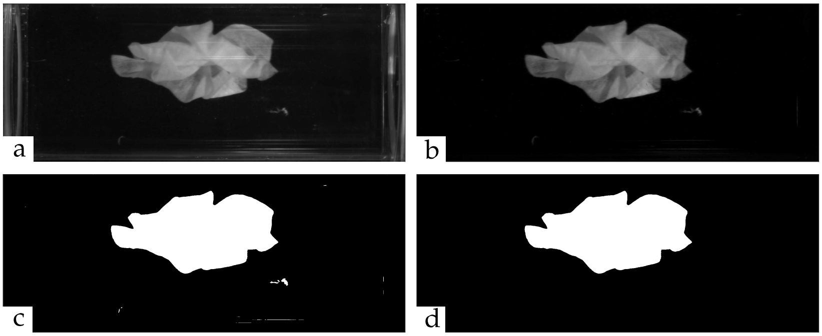

Fig. A.3: Overview of image processing steps. a) Original image, b) Background subtraction, c) Conversion to binary image using an intensity threshold value, d) Small objects removed using a size filter

to zero. The resulting binary image is presented in Figure A.3(c). As seen in Figure A.3(c), the image contains small areas with white pixels as well as the big blob, representing the dust cloth. The small areas can be small pieces of textiles, air bubbles or reflections on the surface of the pipe. These are removed with a size filter, deleting all objects with a size smaller than 20,000 pixels. The final image is presented in Figure A.3(d). The described steps apply to images from both AOI1 and AOI2.

Subsequently, the images containing dust cloths are identified and the moments of the remaining blobs, representing the dust cloths, can be determined based on Equation (A.1), where $a_{x,y}$ denotes the pixel brightness with a number of zero (black) or one (white) for binary images and x and y are pixel coordinates. For binary images the zeroth order moment is also the area of the blob.

$$m_{i,j} = \sum_x \sum_y x^i y^j a_{x,y} \tag{A.1}$$

Based on the first- and zeroth-order moments the coordinates of the centroid, X and Y can be determined using Equation (A.2).

$$X = \frac{m_{10}}{m_{00}} \qquad \text{and} \qquad Y = \frac{m_{01}}{m_{00}} \tag{A.2}$$

The shape of the dust cloths is described through an elongation ratio ϵ, which is defined as the ratio between the length of the major axis and the minor axis of the ellipse with the same second-order moment as the blob, as given in Equation (A.3), where l_{ma} is the major axis length and l_{mi} is the minor axis length.

$$\epsilon = \frac{l_{\mathrm{ma}}}{l_{\mathrm{mi}}} \tag{A.3}$$

The orientation of the dust cloths is found as the angle between the x-axis and the major axis of the ellipse with the same second-order moment as the dust cloth.

A.4 Results

The properties of area, elongation ratio, orientation and vertical position of the dust cloths in the suction pipe have been captured for all operating points. The analysis of variance (ANOVA) is used to test if the mean value of these properties changes with the operating point. The hypothesis H_0 that all the means, μ, are equal, given in Equation (A.4) is tested. The results are displayed in Table A.3.

$$H_0 : \mu_1 = \mu_2 = ... = \mu_{\mathrm{a}} \tag{A.4}$$

$$H_1 : \mu_{\mathrm{i}}\mu_{\mathrm{j}} \quad \text{for at least one pair} \tag{A.5}$$

The p-value is the probability for the same or more extreme results to occur if the hypothesis H_0 is true. Therefore, if $p < 0.05$ it is concluded that H_0 is false and that there is significant difference between the obtained mean values, meaning that the operating point influences the tested parameter.

As seen in Table A.3 the p-value reveals that the area of the dust cloths changes significantly with the operating point. The mean area as a function of the volume flow in the pipe is presented in Figure A.4 with 95% confidence intervals. It is seen in Figure A.4, that there is a decrease in the area with an increase of the flow. Oppositely, Table A.3 shows that the elongation ratio, orientation and vertical position do not change significantly with the operating point.

Figure A.5(a) shows the distribution of the centroid of the dust cloths over a vertical section of the suction pipe, where $Y = 0$ represents the centre of the pipe. It is seen that the dust cloths mainly move around 0.02 m below the centre of the pipe.

	800 RPM			985 RPM			1200 RPM			p
	50%BEP	75%BEP	100%BEP	50%BEP	75%BEP	100%BEP	50%BEP	75%BEP	100%BEP	
Area (m2)										
μ	0.0147	0.0126	0.0123	0.0134	0.0131	0.0111	0.0140	0.0119	0.0114	4.80e-10
σ	0.00398	0.00334	0.00336	0.00372	0.00347	0.00321	0.00422	0.00301	0.00418	
Elongation Ratio (-)										
μ	2.60	2.70	2.88	2.64	2.73	2.69	2.72	2.53	2.53	0.489
σ	1.12	1.15	1.17	1.16	1.15	1.29	1.18	1.08	1.06	
Orientation (deg)										
μ	5.92	6.19	4.57	4.75	5.97	8.71	8.14	6.92	8.26	0.752
σ	21.0	24.0	20.9	23.7	23.5	26.5	18.5	27.7	22.66	
Y Position (mm)										
μ	2.27	-0.002	8.68	-3.81	-2.08	-4.70	-2.06	-0.72	-2.36	0.0971
σ	32.2	34.3	34.5	33.8	32.4	35.4	31.0	32.3	34.5	

Table A.3: Comparison of the mean values from each operating point using ANOVA gives the p-values listed in the table. A *p*-value less than 0.05 indicates that the difference between the mean values is significant

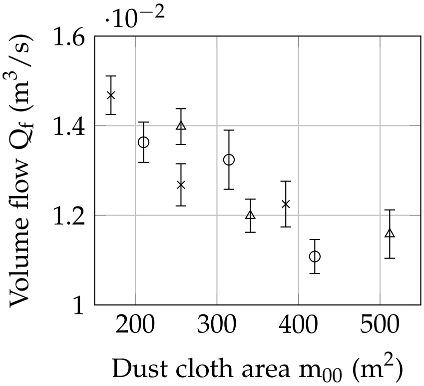

Fig. A.4: Area as function of flow velocity in the suction pipe. The bars show one standard deviation. × 800 RPM, ○ 985 RPM, △ 1200 RPM.

The dust cloth area m_{00}, orientation θ and elongation ratio ϵ, depend on the vertical position in the pipe. This is illustrated in Figure A.5(b–d). The mean area of the dust cloths as a function of the vertical position of the centroid of the dust cloths in the pipe is presented in Figure A.5(b) with 95% confidence intervals. It is seen that the area is nearly constant in the range from –0.05 m to 0.05 m, and that it decreases significantly outside this range.

Figure A.5(c) shows the mean elongation ratio ϵ as a function of the dust cloth position. It appears that the maximum ratio of around three, occurs in the centre of the pipe. The elongation ratio decreases to 1.5 at the outer part of the suction pipe.

The angle between the dust cloths and the X-axis (see θ in Figure A.2) as a function of the vertical position is presented in Figure A.5(d). There is a clear change in the angle with the vertical position. Above the centre of the pipe the dust cloths are very close to parallel to the flow, while there is an angle of around 12 degrees to the horizontal just below the centre of the pipe.

The contour plot presented in Figure A.6 is made by translating the centroid of all 2123 recorded dust cloths to a common position and noting the area they cover. The contour plot shows that the dust cloths cover a regularly shaped ellipse with a small angle to horizontal and an elongation ratio of approximately two.

A.4.1 Comparison between Dust Cloth Positions in AOI1 and Parameters in AOI2

Table 4 shows a comparison of the dust cloth parameters in AOI2, depending on where the dust cloths enter the suction pipe. The inlet to the suction pipe is divided into a left and a right half of the pipe, marked with L and R in Figure A.1(b). Table A.4 shows only minor differences between the dust cloth area and elongation ratio in AOI2. However, the Y position shows a tendency of the dust cloths entering in the left side of the inlet to the suction pipe to have a position above the centre of the pipe, while the dust cloths entering at the right side of the suction pipe show a tendency to be below the centre of the pipe. Furthermore, the angle to the X-axis is higher for dust cloths entering in the right side of the suction pipe. This observation corresponds to the results presented in Figure A.5(d), showing that the angle is higher for dust cloths below the centre of the pipe. Several additional parameters such as the textile size and properties, impeller type, and geometrical changes in the inlet pipe may affect the results and this could be investigated in detail in future studies using design of experiments to decide on which combinations of parameters should be tested. Furthermore, observation of the textile as it leaves the impeller to determine how the appearance of the textile changes as it is pumped is also an interesting perspective.

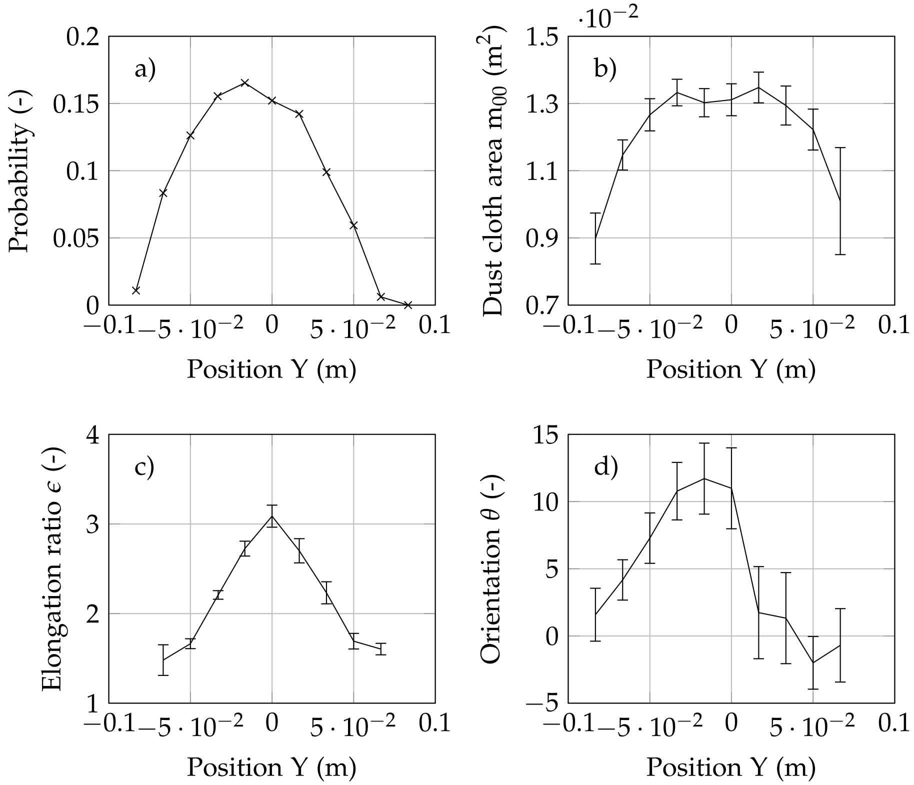

Fig. A.5: a) The distribution of dust cloths over a vertical section of the suction pipe. b) Mean dust cloth area as a function of the vertical position in the pipe with. c) Mean ratio of the major and minor axis. d) Mean orientation as function of the vertical position. The error bars mark the 95% confidence intervals. $Y = 0$ in the centre of the pipe

Property	Position AOI1	Value
Area (m^2)	Left	0.0130 ± 7.6e-4
	Right	0.0127 ±6.7e-4
Elongation ratio (-)	Left	2.56 ±0.23
	Right	2.72 ±0.21
Orientation (degree)	Left	4.5 ±5.2
	Right	8.0 ±3.8
Y position (m)	Left	0.009 ±6.8
	Right	-0.008 ±5.7

Table A.4: Dependence between AOI1 and AOI2

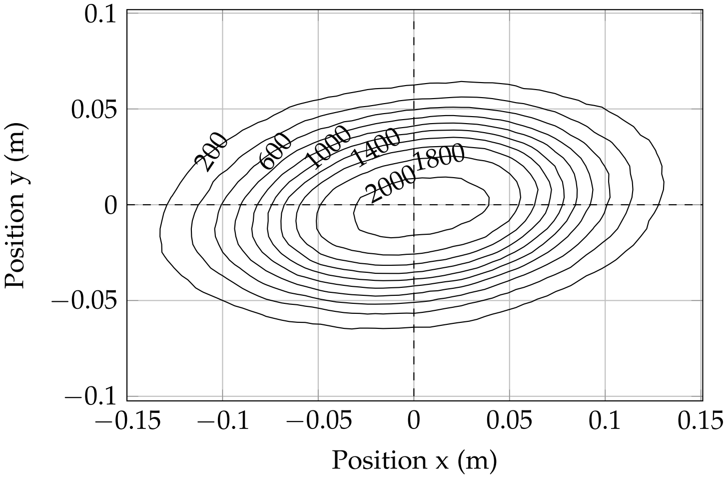

Fig. A.6: Contour plot of the extent of the dust cloths, when they are all placed with the centroid in a common position.

A.5 Conclusion

Based on images of 2123 dust cloths passing through the suction pipe to a dry-installed wastewater pump, the area, orientation, elongation ratio and vertical position of dust cloths upstream of the pump inlet have been analysed, and the dependency of these parameters on the operating point of the pump has been determined.

The most common dust cloth position is at 0.02 m below the centre of the suction pipe. At this position the values of area, elongation ratio and orientation are 0.013 m^2, 3.1 and 12 degrees, respectively. These parameters are slightly different than the mean value of each property and the variation of the properties along the span of a vertical section of the pipe, indicates that appropriate parameters should be found based on the desired vertical position of the simulated dust cloth rather than the overall mean values. The position of the dust cloths in AOI2 is connected to the position in AOI1 where the dust cloths enter the suction pipe. Dust cloths entering in the left part of the suction pipe tend to have a position above the centre of the pipe in AOI2, while dust cloths entering the right part of the suction pipe tend to have a position below the centre.

There is no significant change in the mean value of the orientation, elongation ratio and vertical position of the dust cloths between the operating points. The recorded area of the dust cloths in the suction pipe changes with the operating point and ranges from 0.011 to 0.015 m^2. The higher the flow rate, the smaller the area. The insignificant change of the position, orientation and elongation ratio shows that a very similar textile shape can be used as initial condition for simulations at different operating points, while care must be taken regarding the covered area and thereby the degree of crumbling. Notice that the images are taken from one direction, meaning that a two-dimensional (2D) representation of the dust cloths is obtained rather than the full three-dimensional (3D) shape.

The determined parameters of orientation, area and elongation ratio as function of the position in the pipe will be implemented as initial conditions for textile in future clogging simulations. The independence of operating point for three out of four tested parameters shows that different types of clogging occurring at different operating points is likely due to a change in the flow conditions inside the pump rather than upstream of the pump. Simulations of clogging effects, using the determined initial conditions, may help to understand these different types of clogging and work as a tool in the design process of wastewater pumps to ensure a high resistance to clogging.

A.6 Acknowledgements

Financial support from Grundfos Holding A/S and Nordic Water Network is gratefully acknowledged.

A.7 Disclosure Statement

No potential conflict of interest was reported by the authors.

References

Friedler, E., Brown, D. and Butler, D. A study of wc derived solids. *Water Science and Technology*, 33:17–24, 1996.

Littlewood, K. and Butler, D. Movement mechanisms of gross solids in intermittent flow. *Water Science and Technology*, 47:45–50, 2003.

McDougall, J. and Wakelin, R. The influence of flush volume and branch drain cross-section on deformable solid transport in attenuating flows. *Building Services Engineering Research and Technology*, 28:7–22, 2007.

Mitchell, R-L., Gunkel, M. Waschnewski, J. and Thamsen, P.U. Investigations into wastewater composition focusing on nonwoven wet wipes. *Technical Transactions*, 1:125–135, 2017.

Niessen, W. and Chansky, S. The nature of refuse. In *Proceedings of National Incinerator Conference, New York*, 1970.

Pöhler, M., Gerlach, S., Höchel, K., Mengdehl, T., and Thamsen, P.U. Linking efficiency to functional performance by a pump test standard for wastewater pumps. *ASME/JSME/KSME 2015 Joint Fluids Engineering Conference, Seoul, South Korea*, 1A: Symposia, Part 2, July 26-31 2015.

Spence, K., Digman, C., Balmforth, D., Houldsworth, J., Saul, A., and Meadowcroft, J. Gross solids from combined sewers in dry weather and storms, elucidating production, storage and social factors. *Urban Water Journal*, 12: 773–789, 2016.

Thamsen, P.U. Cutting clogging in wastewater. *World Pumps*, April:22–25, 2009.

Walski, T., Falco, J., McAloon, M., and Whitman, B. Transport of large solids in unsteady flows in sewers. *Urban Water Journal*, 8:179–187, 2011.

Paper B

Case Study on the Motion of Rags through the Housing of a Wastewater Pump in Part Load

Anna Lyhne Jensen, Henrik Sørensen, Lasse Rosendahl and
Flemming Lykholt-Ustrup

The paper is under review.

Case Study on the Motion of Rags through the Housing of a Wastewater Pump in Part Load

Anna Lyhne Jensen[a], Henrik Sørensen[a], Lasse Rosendahl[a], Flemming Lykholt-Ustrup[b]

[a] *Aalborg University, Department of Energy Technology, Pontoppidanstræde 111, DK-9220 Aalborg, Denmark*
[b] *GRUNDFOS Holding A/S, Wastewater Hydraulics, Poul Due Jensens Vej 7, DK-8850 Bjerringbro, Denmark*

Abstract

The motion of rags inside the volute of a submersible wastewater pump with a transparent housing is recorded with a fast digital camera and examined through image analysis. The pump is running in part load at 55%, 60%, 70%, 85% and 90% of the flow at the best efficiency point with an impeller speed of 1200 RPM. Three types of rag motion are observed; 1) rags getting stuck on the tongue; 2) rags re-circulating in the volute; and 3) rags exiting the pump as they reach the outlet. Rags exiting the pump are furthest from the impeller centre throughout the volute with an especially distinct difference occurring from around 100 degrees before the pump outlet. A decrease from an average of 111 rag re-circulations in the volute to less than one and a decreased tendency of the rags to stay on the tongue is observed as the operating point moves towards the best efficiency point, where rags easily pass through the tested pump geometry.

Keywords: Pump, wastewater, image analysis

B.1 Introduction

Accumulation of textile material inside the volute of wastewater pumps, also known as clogging, challenges the reliable operation of wastewater pumping systems. With population growth in urban areas (Koop and van Leeuwen, 2017), and an increasing use of personal hygiene wet wipes, the solids content of sanitary textile material in wastewater is only expected to increase. Spence et al. (2016) characterised the solids content in wastewater for three different catchment areas and identified wet wipes as the most common solid object after faeces and toilet tissue for each of these areas. Furthermore, objects such as tampons, panty liners, cotton buds, sanitary towels and sanitary towel shells were identified in the wastewater. Since these objects do not disintegrate in the wastewater, they tend to accumulate in the system and cause clogging. This leads to expensive breakdowns of wastewater pumps. After these breakdowns, the pumps often require manual cleaning to return to normal operation.

The ability of wastewater pumps to handle different solid objects without clogging is commonly investigated using artificial wastewater in test rigs. Artificial wastewater is clean water with addition of solids such as rags, ropes, plastic bags or similar, to represent the solids found in real wastewater. Generally, the test rigs do not allow optical access to the clogging incidents as they occur. Instead, the pump is disassembled after each run to identify if and where material has accumulated inside. Using this approach, Thamsen (2009) identified different types of clogging at different pump operating points. These include clogging in the impeller inlet, impeller channel, casing, shroud clearance, impeller gap, suction sump and pipe. Subsequently, Pöhler et al. (2015) presented a functional performance index to include the ability of wastewater pumps to handle materials such as wet wipes into the evaluation of wastewater pumps. A more detailed understanding of flow effects or typical motion of the sanitary material leading to clogging was not in the scope of these investigations.

Clogging typically occurs inside the pump housings. Therefore, visual access to the housing is required to observe clogging phenomena as they occur. Transparent pump housings have previously been used to examine pump cavitation (Coutier-Delgosha et al., 2003; Mousmoulis et al., 2017), and to investigate the interaction between coarse particles and the pump impeller by Tan et al. (2017). Recently, Gerlach et al. (2017) used a transparent pump housing to investigate the ability of different vortex impellers to handle textile materials. However, this study did not focus on the detailed motion of each piece of textile. In the present work, a transparent housing is constructed to replace the original housing on a commercial pump, and a fast digital camera is used to capture the motion of rags through the housing. Using image analysis it is investigated if there are differences in the motion of single pieces of textiles inside the housing at five different part load operating points. Additionally, the present work quantifies the risk of pieces of textile material staying inside the pump housing, increasing the risk of accumulations and thereby clogging. These observations are important to improve the understanding of clogging effects as they occur, and thereby to identify operating points or design features that reduce the risk of clogging.

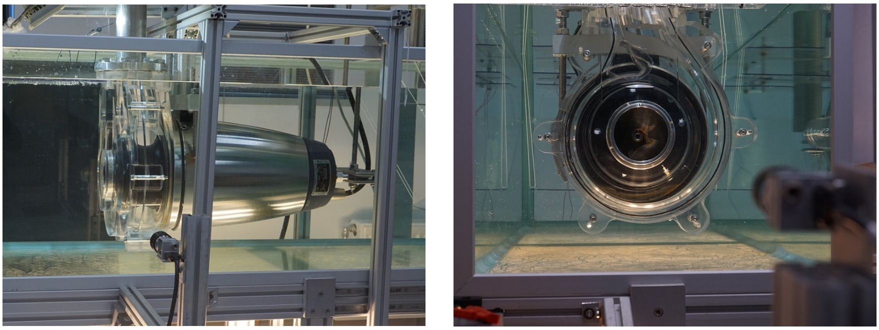

Fig. B.1: Pump with transparent housing placed horizontally in glass aquarium. Left: The pump seen from the side. Right: The inlet and housing of the pump.

B.2 Materials and Methods

The experimental setup consists of a commercial submersible wastewater pump with a single channel impeller. The original housing of the pump is replaced with a corresponding housing constructed in perspex to enable visual access into the housing. The pump has an inlet diameter of 100 mm and a free passage of 80 mm. It is placed horizontally in a glass aquarium of size 1.95 m × 0.56 m × 0.58 m. The aquarium ensures good visual access to the pump. The setup is presented in Figure B.1. Figure B.1 to the left shows the submersible pump with transparent housing seen from the side. The camera on the side of the pump is used to determine when a piece of textile enters the impeller. Figure B.1 to the right show the setup seen from the front with a clear view to the inlet and housing of the submersible pump. The camera placed here records the motion of the textile through the pump house for later analysis. The camera is placed on the axis of rotation of the impeller with an image plane normal to the rotational axis and a field of view of 0.21 m × 0.27 m (1044 pixel × 1344 pixel). The field of view includes the entire volute, the tongue and a part of the outlet. The camera captures grayscale images. Details on the camera and camera settings are given in Table B.1. Figure B.2 illustrates an example of the field of view with a definition of the angle around the volute. This will be used in the analysis. The impeller is rotating in the counter clockwise direction when seen from the camera.

Flow restrictors are used to control the flow and the experiments are done for 55%, 60%, 70%, 85% and 90% of the nominal flow in the best efficiency point. The pump is connected to a variable speed drive enabling control of the rotational speed of the impeller. Due to limitations because of the relatively small aquarium used as the pump sump, the pump is run at 1200 RPM, which is slightly lower than the nominal 1445 RPM.

Clogging tests are commonly accomplished using artificial wastewater,

Camera	Basler acA1920-155 µm
Lens	Cosmicar/Pentax TV lens 25 mm
Field of view	0.21 m × 0.27 m
Resolution	1044 pixel × 1344 pixel
Frame rate	100 fps
Exposure time	300 µs

Table B.1: Details on the camera and camera settings.

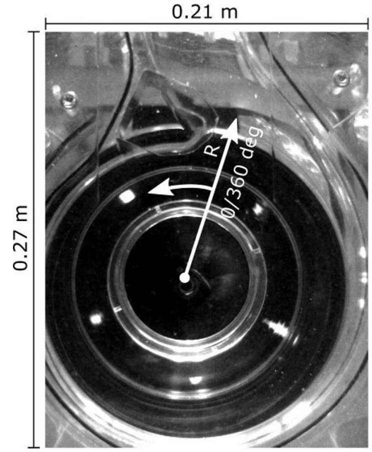

Fig. B.2: Example of the field of view and the definition of the angle around the volute starting with zero at the tongue increasing in the counter-clockwise direction.

which is clean water with addition of objects commonly found in real wastewater. The artificial wastewater used in the present work is created using dust cloths, which have commonly been used in clogging tests and which have proven to recreate all types of clogging (Thamsen 2009, Pöhler 2015, Gerlach 2017). The dust cloths are 220 mm × 300 mm (±10%) with a thickness of approximately 0.75 mm. They are made of polyester fibres (90%) around a mesh of polypropylene (10%). These dust cloths will be referred to as rags in the following. To be able to control the experiments and to characterise the rag motion using image analysis, only one rag at the time is added to the water in the aquarium and recorded as it moves through the pump. It is expected that if the rag stays in the volute for a longer time, there is a higher risk of rags accumulating in the pump. Furthermore, as the rags keep re-circulating in the housing or get stuck on the tongue, they become worn into smaller pieces or into fibres that risk getting stuck in the cavities. In some cases the rags stay in the volute for a long time. Each experiment was stopped if a piece of rag stayed in the same motion for 30 seconds or a total of more than one minute inside the pump. The experiment was repeated 50 times for each of the five tested operating points.

The acquired images are analysed in MATLAB. Figure B.3 shows the steps of the image processing. Firstly, background subtraction is used to decrease the influence of reflections and other disturbances from the background. Then the grey-scale images are converted to binary images using a threshold for pixel intensity. Finally, objects smaller than 5000 pixels are removed from the picture and the remaining blob in the binary image represents the rag. The centroid of this blob is identified to track and analyse the motion of the rags inside the pump. In total, close to 400,000 images were analysed. The identified centroids of the rags were grouped into angles of 20 degrees starting at the tongue as defined in Figure 2. When a rag reached the outlet it would either 1) get stuck on the tongue, 2) re-circulate in the housing or 3) exit the pump. All previously saved positions of the rag in the housing were classified after each circulation in the pump depending on what happened as the rag reached the outlet. This makes it possible to identify differences in the position of the rag during a re-circulation depending on what will happen as it reaches the outlet. Furthermore, the image analysis is used to compare the position of the rag inside the housing depending on the pump operating point. Finally, the number of occurrences of each of the three cases was identified in the analysis. Note that the pump impeller is the original impeller from a commercial pump. Consequently, it is not transparent and therefore the rags can not be identified and analysed until they move from the impeller into the transparent housing.

The following figures illustrate examples of the three mentioned cases that occur as a rag enters the pump geometry. Figure B.4 illustrates an example of a rag entering the pump and leaving the pump as it reaches the outlet.

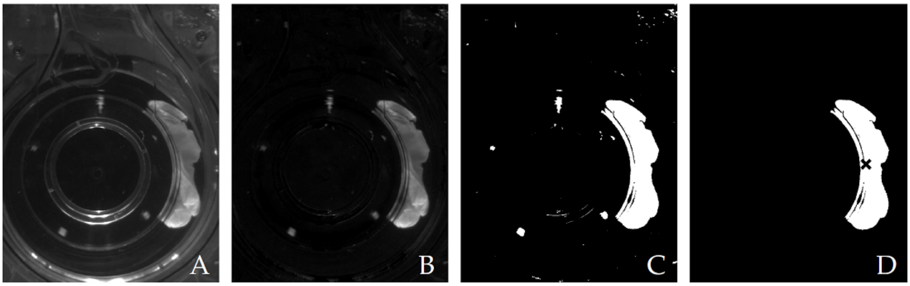

Fig. B.3: Example of image processing of images acquired during the experiment. A-B) Background subtraction, B-C) conversion to binary image using an intensity threshold and C-D) removal of small blobs using a size filter. The centroid of the blob in image D is marked with a cross ×.

Figure B.5 gives an example of a rag which is re-circulating in the housing. Figure B.6 illustrates a rag getting stuck on the tongue as it reaches the outlet.

B.3 Results and Discussion

Using image processing and image analysis as described, the motion of rags through the housing of a submersible wastewater pump was investigated and classified into the three cases exemplified in Figure B.4-B.6. Naturally, for each experiment with a single rag, the rag can only exit the pump once. However, re-circulation of the rag in the housing and the rag getting stuck on the tongue for a second or more can occur repeatedly during an experiment. Figure B.7 illustrates the mean number of occurrences of each of these cases per experiment as function of the operating point from 55% of the flow at the best efficiency point (Q_{BEP}) to 90% of Q_{BEP}. As seen in the figure, the occurrence of both rags re-circulating in the volute flow and the rags getting stuck on the tongue decrease significantly as the operating point approaches the best efficiency point. The mean number of circulations in the housing decreases from an average of around 111 circulations within the time the experiment was run at 55% of Q_{BEP} to 5 circulations at 60% of Q_{BEP} and to only 0.25 at 90% of Q_{BEP}. The risk of rags getting stuck on the tongue is much higher for 55% and 60% of the best efficiency point with an average of 0.82 cases/rag compared to 0.04 cases/rag at 90% of Q_{BEP}. Furthermore, as the flow increases the amount of rags exiting the pump within the time frame increases from less than half at 55% to all rags at 90% of Q_{BEP}.

In addition to the number of occurrences of each type of motion, the position of the rags throughout the volute have been analysed depending on the type of motion and the operating point. The results are presented

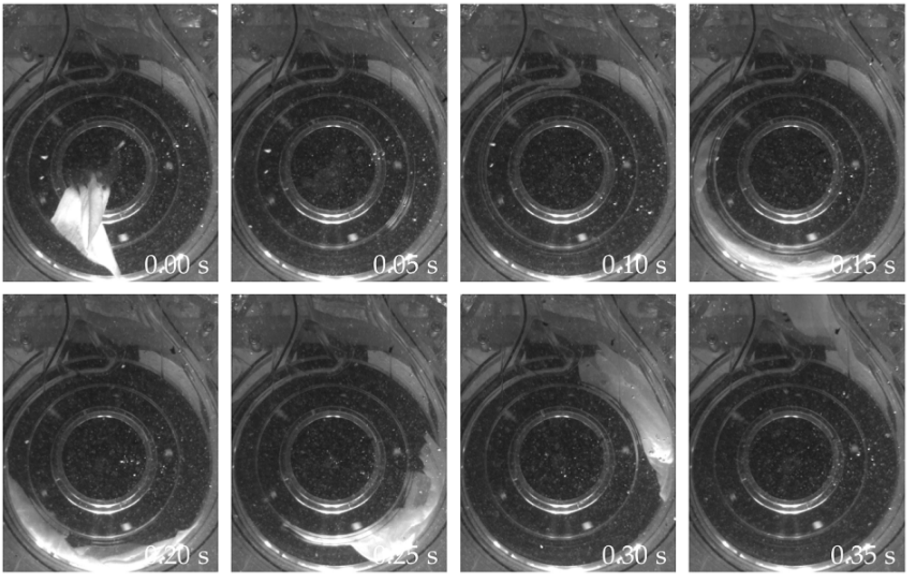

Fig. B.4: Example of a rag leaving the pump as it reaches the outlet.

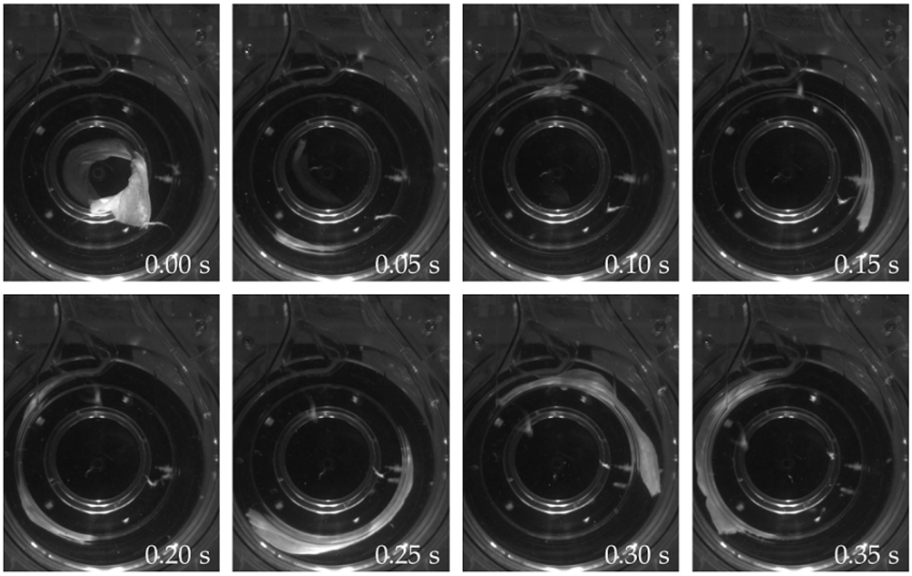

Fig. B.5: Example of rag re-circulating in the housing.

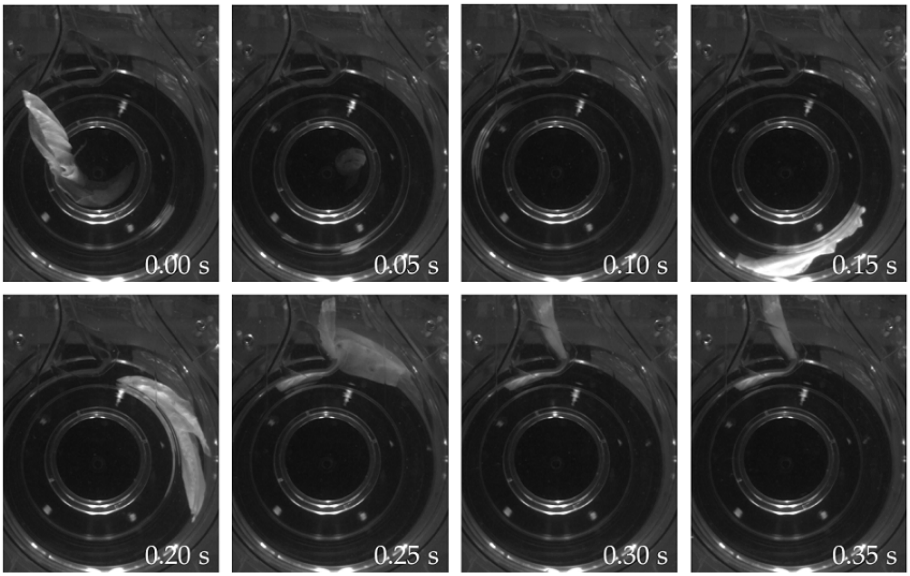

Fig. B.6: Example of rag getting stuck on the tongue.

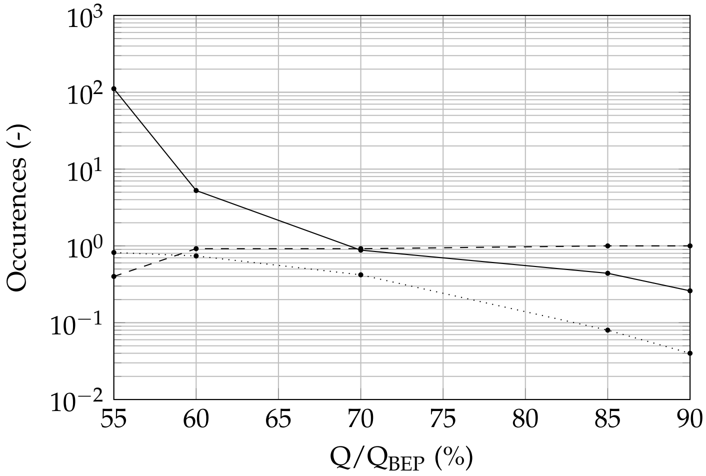

Fig. B.7: Mean occurrence per test of a single piece. · · · · textile getting stuck on the tongue, —— textile staying in the flow in the volute, – – – textile exiting the pump when reaching the outlet.

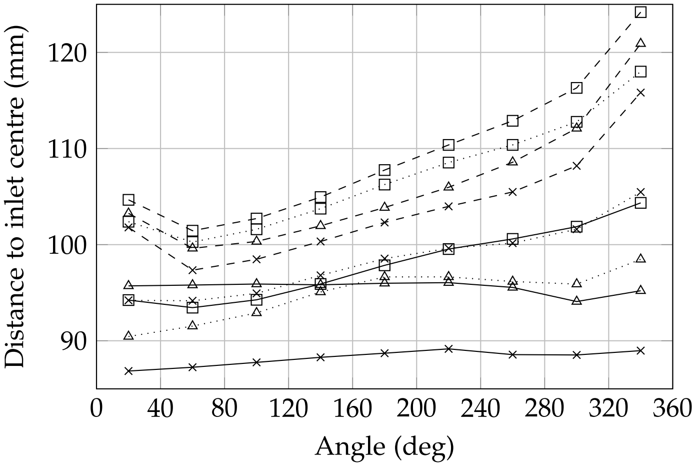

Fig. B.8: Distance to impeller centre, ···· textile getting stuck on the tongue, —— textile staying in the flow in the volute, — — — textile exiting the pump when reaching the outlet. □ 60% BEP, × 70% BEP, △ 90% BEP.

in Figure B.8 and B.9, showing the distance to the impeller centre and the gradient of motion away from the centre as function of the angular position of the rags in the volute. Both figures show results for the three identified cases of motion of rags for three out of the five tested operating points. These are 60%, 70% and 90% of the flow at the best efficiency point. It is seen in Figure B.8 that the rags exiting the pump as they reach the outlet are generally positioned furthest from the impeller centre throughout the volute. Additionally, Figure B.9 shows how the rags exiting the pump have a slightly faster motion away from the centre than the rags staying on the tongue or in the flow between 90 and 260 degrees. Around an angular position of 260 degrees, the gradient significantly increases and the rags exiting the pump move away from the centre with up to around 0.4 mm/degree. Interestingly, the rags exiting the pump move towards the centre of the impeller from 20 to 90 degrees. This may be due to the rags coming from the tongue, almost reaching the outlet, and moving back into the narrowest part of the volute.

The rags that get stuck on the tongue are closer to the impeller centre throughout the volute compared to the rags exiting the pump as seen in Figure B.8. Figure B.9 shows how the rags getting stuck on the tongue begin to move towards the outer part of the volute around 260 degrees. However, this movement is much less distinct than the movement of the rags exiting the pump and not enough for the rags to move out of the pump. The rags re-circulating in the volute are generally closest to the impeller inlet throughout the volute, and have the most constant distance to the impeller inlet as illustrated in Figure B.8 and B.9. The rags in the pump at heavy part load

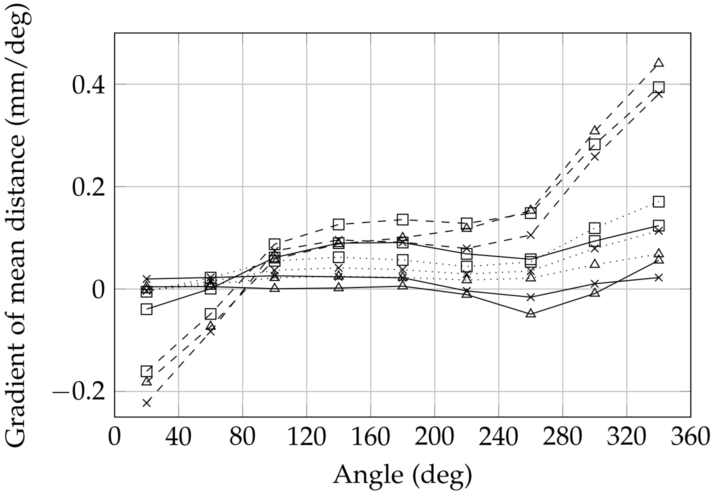

Fig. B.9: Gradient of the distance to impeller centre, · · · · textile getting stuck on the tongue, —— textile staying in the flow in the volute, − − − textile exiting the pump when reaching the outlet. □ 60% BEP, × 70% BEP, △ 90% BEP.

(60% of Q_{BEP}) have a location further from the centre than the rags in the volute when the pump is operating closer to the best efficiency point. This is unexpected, since Figure B.7 shows that the rags tend to re-circulate in the volute at (60% of Q_{BEP}). However, this may be due to an observed tendency of the rag area to decrease as the operating point gets closer to the best efficiency point, which could be due to the rags being less stretched around the impeller at lower flows, covering a larger part of the volute.

Looking at angular positions from 180 degrees to the outlet at 360 degrees for each operating point separately, the rags exiting the pump are positioned furthest from the impeller centre followed by the rags getting stuck on the tongue and the rags re-circulating in the volute are closest to the impeller centre. The tendency of rags to re-circulate in the volute or get stuck on the tongue at heavy part load is a result of an increase of the flow that re-enters the volute at the tongue instead of going to the outlet.

B.4 Conclusion

Rags exiting the pump are generally moving further from the impeller centre than other rags throughout the volute with an especially distinct difference occurring from around 100 degrees from the pump outlet. Rags getting stuck on the tongue also move outwards around 100 degrees from the pump outlet, but much less than the rags exiting the pump. The rags re-circulating in the volute flow move with the most constant distance to the impeller centre. For the tested pump geometry, the number of occurrences of the rags getting stuck on the tongue or re-circulating in the flow in the volute decreases significantly as operating point moves closer to the best efficiency point. Since the risk of accumulations inside the pump is very likely to increase with an increased residence time of each rag in the volute, it must be expected that a high number of re-circulations of rags in the volute and rags on the tongue at heavy part load indicates a higher risk of clogging when a pump is operating in part load condition. The results show that especially operating at 60% of Q_{BEP} or less leads to significant changes in the movement of rags in the pump and a higher risk of clogging.

B.5 Conflicts of Interest

The authors declare that there is no conflict of interest regarding the publication of this paper.

B.6 Funding Statement

This work was funded by Grundfos and the Department of Energy Technology at Aalborg University.

B.7 Acknowledgments

A major part of the experiments have been carried out by a group of students in the Thermal Energy and Process Engineering program in Aalborg University. The authors would like to thank E. Arberg, L. Blæsbjerg, M. Rubæk, E. Ravn, K. Vestdam, G. Olafsson and R. Dueholm for their contribution.

References

Coutier-Delgosha, O., Fortes-Patella, R., Reboud, J., Hofmann, M., and Stoffel, B. Experimental and numerical studies in a centrifugal pump with two-dimensional curved blades in cavitating condition. *Journal of Fluids Engineering*, 125:970–978, 2003.

Gerlach, A., Wulff, S., Perlitz, D., Lykholt-Ustrup, F., and Thamsen, P. The optimal vortex pump impeller - an experimental study on clogging behaviour. In *Proceedings of 12th European Conference on Turbomachinery Fluid dynamics and thermodynamics*, April 3-7 2017.

Koop, S. and van Leeuwen, C. The challenges of water, waste and climate change in cities. *Environment, Development and Sustainability*, 19:385–418, 2017.

Mousmoulis, G., Karlsen-Davies, N., Aggidis, G., Anagnostopoulos, J., and Papantonis, D. Experimental analysis of the onset and development of cavitation in centrifugal pump. *Journal of Physics: Conf. Series*, 813:1–5, 2017.

Pöhler, M., Gerlach, S., Höchel, K., Mengdehl, T., and Thamsen, P. Linking efficiency to functional performance by a pump test standard for wastewater pumps. In *ASME/JSME/KSME 2015 Joint Fluids Engineering Conference, Seoul, South Korea*, July 26-31 2015 2015.

Spence, K., Digman, C., Balmforth, D., Houldsworth, J., Saul, A., and Meadowcroft, J. Gross solids from combined sewers in dry weather and storms, elucidating production, storage and social factors. *Urban Water Journal*, 12: 773–789, 2016.

Tan, M., Lian, Y., Liu, H., Wu, X., and Ding, R. Visualizing test on the pass-through and collision characteristics of coarse particles in a double blade pump. *International Journal of Naval Architecture and Ocean Engineering*, pages 1–8, 2017.

Thamsen, P. Cutting clogging in wastewater. *World Pumps*, April:22–25, 2009.

Paper C

Experimental Investigation of the Motion and Shape of Flexible Objects near a Pump Inlet

Anna Lyhne Jensen, Raja Abou Ackl, Stefan Gerlach, Henrik Sørensen, Lasse Rosendahl and Paul Uwe Thamsen

The paper was presented in
20th Australasian Fluid Mechanics Conference, Perth, Australia, December 5-8, 2016, https://people.eng.unimelb.edu.au/imarusic/proceedings/20/597%20Paper.pdf

Experimental Investigation of the Motion and Shape of Flexible Objects near a Pump Inlet

Anna Lyhne Jensen[a], Raja Abou Ackl[b], Stefan Gerlach[b], Henrik Sørensen[a],
Lasse Rosendahl[a], Paul Uwe Thamsen[b]

[a] *Aalborg University, Department of Energy Technology, Pontoppidanstræde 111, DK-9220 Aalborg, Denmark*
[b] *Technical University of Berlin, Department of Fluid System Dynamics, Straße des 17. Juni 135, D-10623 Berlin, Germany*

Abstract

Previous investigations of clogging effects in waste water pumps have focused on the impact of pumping contaminated water on the pump performance, as well as the influence of the operating point on the location of clogged material in the pump and in the pumping system. The present work aims to characterise the dynamics of flexible material entering a rotating impeller. Experiments are carried out in a wet pit located in the Department of Fluid System Dynamics in TU Berlin. The wet pit is modified with an acrylic plate placed at the bottom of the pit, enabling visual access to the suction side of the pump. Clean water containing synthetic dusters for housekeeping of size 21 cm × 30 cm are used as artificial waste water with a high degree of contamination. A high speed camera is used to capture the duster motion to identify characteristic movements of the dusters for operating points of 60%, 100% and 120% of the Best Efficiency Point (BEP). Three characteristic movements of the dusters as they enter the pump were found. Furthermore, a very clear correspondence between decrease in pump performance and the amount of visible dusters collected at the leading edge of the impeller was found for 100% and 120% of the BEP. For 60% of the BEP clogging occurred at the tongue and no correlation between visible dusters in the pump inlet and pump performance was observed.

C.1 Introduction

Waste water is transported from cities and industrial areas through a pumping system of channels, pressure pipelines and waste water pumping stations. The reliability of this system is essential, since breakdowns are both costly and can result in overflow and pollution. A major challenge in ensuring the reliability of the system is the increase of the content of flexible material with high tensile strength in the waste water. Especially the increasing market of baby-, cosmetic- and toilet wet wipes has led to an increased amount of these objects in the waste water, causing clogging in the waste water pumps. Mitchell et al. (2016) analysed samples of waste water collected from two catchment areas in Berlin to determine the composition of material in waste water and the size of the objects causing clogging. The material was divided into plastics, textiles, papers and wood and leaves. The composition changed significantly from sample to sample, but textiles represented on average 33% of the physical constituents. Focusing on the textile, the wet wipes represented the largest part. In this work Mitchell et al. (2016) also analysed clogging material and found that textile material represented more than 90% of the material found in a clogged pump. Furthermore, it was found by analysing the size of the substances that material with an area around 210 cm^2 corresponding to the size of wet wipes dominated. These results emphasise the severity of the challenges flexible textile materials cause in the waste water pumping system and motivates the present work to investigate the movement of these materials as they enter the pump to improve the understanding of clogging phenomena.

Due to the difficulty of visually accessing pumps in real wastewater pumping stations, and due to obvious hygienic problems involved with working with real waste water, artificial waste water has been used in several experimental studies (Pöhler et al., 2015; Thamsen, 2009). These studies use synthetic non-woven dusters of 21 cm × 30 cm of polyester and polypropylene to create artificial waste water, since these dusters have proved to have good mechanical properties to recreate clogging scenarios from real pumping stations. The properties of these dusters were investigated and compared to wet wipes by Katscher (2016). The tested properties were mass, material, tensile force and tensile strength as well as length, width and thickness. It was found that the dusters were slightly larger than the average wet wipe with a higher tensile strength and less elongation under tensile force. Despite these slight differences the dusters used in previous experimental studies are also used in the present work.

When a pump is clogged with flexible material the performance significantly decreases and ultimately clogging can lead to a complete stop, which requires manual cleaning for the pump to return to normal operation. Korving and Ottenhoff (2008) investigated failure of waste water pumps using statistical methods showing that pump failures are influenced by several phenomena including the composition of the waste water, discontinuous operation, the succession of dry and wet periods, cleaning frequency, pump design and location and wet well design. Focus on the entire system, is also a topic in the work by Höchel et al. (2013), who similarly investigated the influence of the weather, the pump and the pit design on failure events, and found a high variation in the number of failure events per pumping station, a high weather influence and an impact of the inflow direction to the sump. These results underlines the importance of the system around the pump to avoid clogging. Apart from the system design, also the operation of the system influences the occurrence of clogging. Introduction of a control system to handle the pumping stations of Berlin led to an increase in clogging events, which initiated work to understand the correspondence between pump operating point and clogging. Using the presented dusters in a scaled pumping station with a dry installed pump, Thamsen (2009) and Thamsen et al. (2009) presented results showing different clogging types depending on the operating point of the pump. Operating points of 40%, 60%, 80%, 100% and 120% of the best efficiency point (BEP) were investigated. The type of clogging changes from being dominated by clogging at the suction sump at 40% of the BEP onto the impeller gap and impeller channel between 60% and 80% of the BEP, changing to domination of clogging in the casing and shroud clearance at 100% and 120% of the BEP. Other identified clogging scenarios include clogging at the impeller inlet and suction pipe.

The results by Thamsen (2009) and Thamsen et al. (2009) show different characteristics of clogging occurring in waste water pumps depending on the operating point. To improve the understanding of what leads to these different types of clogging, the present work investigates if the difference can be identified at different operating points in the movement and shape of the material before entering the pump. Contrary to the work by Thamsen (2009), this work is carried out in a wet pit pumping station where the pump is placed inside the waste water as opposed to a pumping station with a dry installed pump. The result will provide data for determining initial conditions and validation during development of simulation of clogging effects which is the long term aim of the on-going work.

C.2 Method

A wet pit has been modified with a bottom made of acrylic glass, enabling visual access to the suction side of the pump as illustrated in figure C.1. The wet pit is placed on a stand, and a camera is placed under the pit. The wet pit is equipped with two pumps, with one pump being tested in the present work. This is a submersible pump with a single vane impeller for application in highly contaminated waste water. The volume flow, the rotational speed of the impeller as well as the current and power consumption is logged during experiments. The pump is run at one of three tested operating points and the pump inlet is recorded with a Basler acA1920-155um fast digital camera as the duster moves into the pump. The Field of View (FOV) of 150 mm × 150 mm is covering the pump inlet, which is recorded with a frame rate of 160 fps and an exposure time of 1000 μs to capture the motion of the dusters

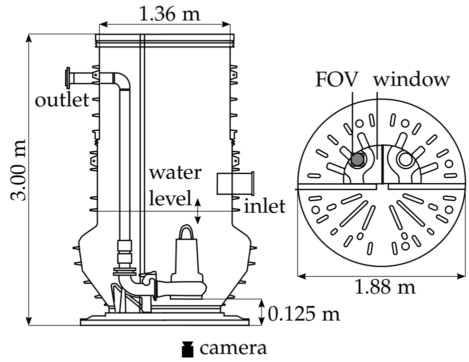

Fig. C.1: Sketch of the modified wet pit.

as they enter the impeller. Each picture has a resolution of 1216 × 1216 pixel corresponding to 0.12 mm/pixel. The impeller rotates with approximately 1400 rpm resulting in a movement of roughly 8 deg during the exposure time and a movement of around 50 deg by the impeller between the images.

To create artificial waste water with high contamination, 175 of the described synthetic dusters are added to the water in the wet pit. The water is pumped in a closed system so the 175 dusters remain in the system. The wet pit is run for up to 45 minutes, until the power consumption reaches 130% of the nominal value due to clogging, or until no further clogging occurs as the dusters get torn apart as they repeatedly pass through the pump. The movement of the dusters is recorded at operating points of 60%, 100% and 120% of the BEP, corresponding to volume flows of 60 m^3/h, 100 m^3/h and 120 m^3/h respectively. The images are analysed and characteristic movements of the dusters are identified. Furthermore, the types of clogging occurring at the different operating points are identified.

C.3 Results

The results are divided into a discussion of the correspondence between visible dusters in the pump impeller and pump performance as the pump restores normal operation due to self-cleaning, and characterisation of different types of movements as the dusters enter the pump impeller at different pump operating points.

C.3.1 Self-cleaning

For the operating points 100%, and 120% of BEP, there is a very good correspondence between the amount of visible dusters in the pump impeller, the increase in the logged power consumption and the decrease in volume flow.

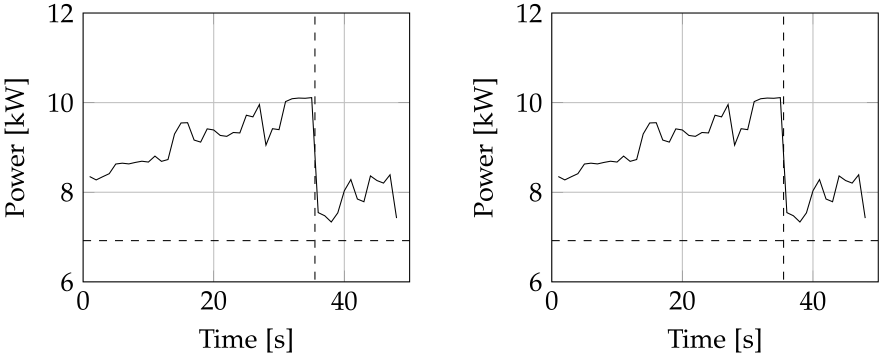

Fig. C.2: Development of power consumption (top) and volume flow (bottom) during 50 seconds of operation at the BEP.

Figure C.2 shows the development of power consumption and the volume flow during 50 seconds of pump operation as dusters begin to clog inside the pump. Until around the 35th second the dusters are collected in the pump impeller rather than passing through the pump, and the power consumption increases while the volume flow decreases as the dusters accumulate at the impeller inlet. The horizontal dashed lines in figure C.2 represent the nominal power consumption and volume flow respectively. As the power consumption reaches a high value, at one point the visible dusters disappear from the impeller and the power consumption returns to the original state within a rotation of the pump impeller. This point is marked with the vertical dashed line. At the same point there is a significant increase in volume flow towards the original 100 m^3/h. Image sequence 1 in figure C.3 shows how the dusters at the impeller inlet disappear within a rotation of the impeller at the point corresponding to the vertical line in figure C.2. It is not known if dusters at different places in the pump affects the clogging too, however the moment the dusters in the impeller disappear, the pump returns to normal operation. Several very similar self-cleaning points where continuously observed during pump operation, and the dusters clogged in the impeller did not lead to pump failure.

C.3.2 Duster Motion at the Impeller Inlet

The movement of the dusters at the impeller depends on the operating point, likely due to differences in the flow behavior. In figure C.3, image sequences 2-5 illustrate four different occurrences of a single duster entering the counter-clockwisely rotating pump impeller. These four sequences illustrate in total three representative examples of the duster movement and the movement of the majority of the observed single dusters entering the impeller can be

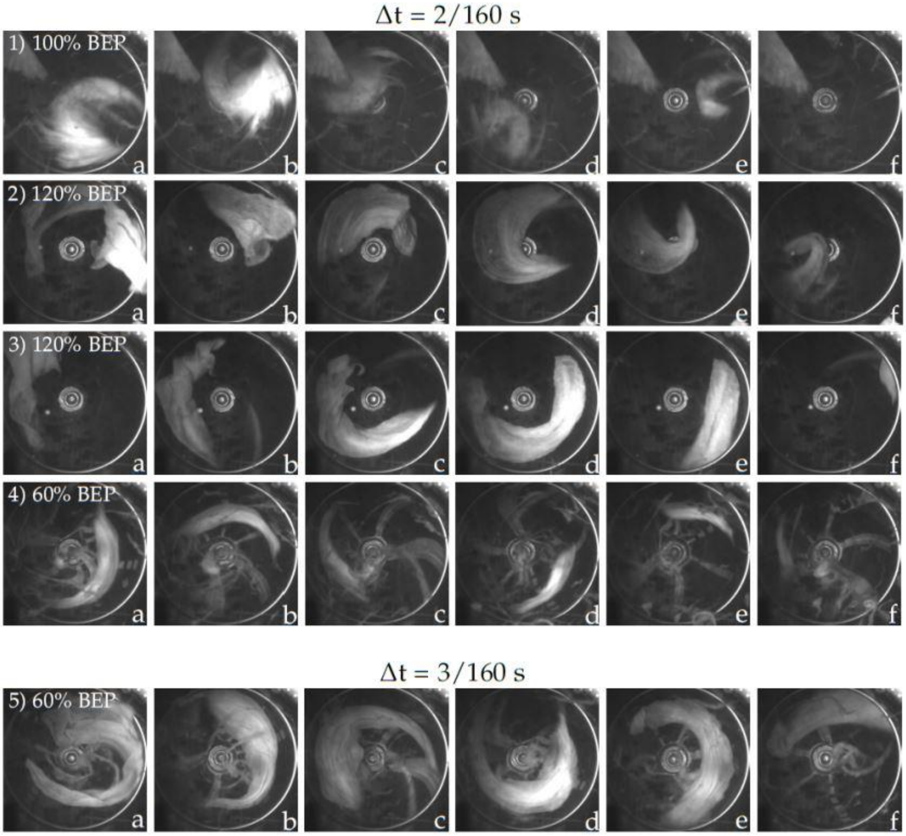

Fig. C.3: Movement of clusters at the impeller inlet at 1) 100% of BEP, 2-3) 120% of BEP, 4-5) 60% of BEP. In image sequence 1-4 2/160 s passes between the images, while 3/160 s passes between the images in image sequence 5.

categorized into one of the three.

Image sequence 2 and 3 are taken at 120% of BEP with a time step of 2/160 s between the images. In image sequence 2 the duster enters the impeller and gets stuck at the edge of the impeller inlet, the duster is pulled along with the impeller as it rotates, forming a U shape as the part of the duster at the impeller inlet edge moves faster than the part of the duster outside the impeller. In images 2e-2f it is seen how the impeller reaches the last part of the duster and the duster finally passes through the pump. As the duster stays at the impeller inlet, more dusters can accumulate at the pump impeller and the pump will start clogging. However, as illustrated in image sequence 1, the pump has a self-cleaning effect, and at one point the collected dusters will disappear. Comparing image sequence 2 to image sequence 1, which shows dusters at the inlet of the impeller when the pump is severely affected by clogging, the behavior of the dusters are similar and the dusters in the clogged pump also disappears as the part of the dusters outside the impeller is reached by the impeller. Image sequence 3 shows a different case from 120% of the BEP. In this sequence the front part of the duster gets stuck to the impeller inlet, but slides off again and the duster passes through the impeller with the rear part first. At the operating points, 100% and 120% of BEP no clogged dusters were found inside the pump after ending the test.

Image sequences 4 and 5 show dusters at the impeller inlet at an operating point of 60% of BEP which is a heavy part load condition. At this operation point no correspondence between the pump performance and the amount of dusters visible at the impeller inlet was observed. Yet, the pump performance gradually decreased with increased power consumption and a decreased volume flow, while dusters where not visibly clogged at the impeller inlet. In image sequence 4, the duster enters the pump impeller and gets stuck at the inlet edge where it slowly slides into the pump. This was not observed for operating points closer to the BEP. Image sequence 5 shows a case very similar to image sequence 3, where the front part of the duster is caught by the edge of the impeller inlet (image 5b) and the duster slides off the impeller inlet again. In image 5f the duster is no longer attached to the inlet edge of the impeller and the duster is sucked into the impeller. The phenomenon in image sequence 2 where the duster forms a U shape was rarely observed at 60% of the BEP. As this type of movement of the duster often resulted in accumulation of dusters at the pump impeller, this may contribute to the fact that the duster rarely accumulates at the impeller when operating at 60% of the BEP.

Fig. C.4: Clogging in the cavity after operating the pump at a part load of 60% of the BEP.

C.4 Conclusions

For the pump operating points 100% and 120% of the BEP, a clear correspondence between visible dusters collected at the impeller inlet and the pump performance was observed. As the amount of dusters increases the power consumption increases and the volume flow decreases. At one point the dusters escapes the impeller inlet and at the same time the pump returns to normal operation. It is not clear if dusters at different places in the pump affects the clogging too. However, no dusters where found inside the pump after testing these operating points.

Operating at 120% of the BEP two main types of duster movements into the pump were observed. Either the front of the duster gets stuck at the impeller inlet but slides off again and the duster moves into the pump with the rear part first. Or the duster gets stuck at the impeller inlet where it stays until the impeller inlet catches up with the part of the duster outside the impeller. This type of movement means that the duster stays at the inlet of the impeller for a long time. If more dusters enter the pump in the same way and stays at the inlet of the impeller the pump begins to clog. Operating at 60% of the BEP two main types of duster movement was observed. Similar to operating at 120% of the BEP the front part of the duster could get stuck around the impeller inlet edge but slide off again and the duster would be sucked in from the opposite side. Alternatively, the duster would get stuck at the impeller inlet edge and slowly slide into the pump.

Two types of clogging were identified. Clogging at the tongue when operating in part load and clogging at the impeller inlet at operating points closer to the BEP. The movement of the dusters before entering the pump has not previously been analysed to understand clogging effects. This work will contribute to validation of simulation of clogging phenomena which is the long term aim of the present work.

C.5 Acknowledgments

Financial support from Grundfos and Nordic Water Network is gratefully acknowledged.

References

Höchel, K., Thamsen, P., and Rauwald, H. Analysing sewage handling problems. *World Pumps*, 2013.

Katscher, B. Textilen im abwasser - bestandsanalyse und erstellung eines lastenheftes für die zugfestigheitsprüfung im feuchten zustand von feuchttüchern. Technical report, Hochschule für Technik und Wirtschaft Berlin, Fachbereich Gestaltung und Kultur, Studiengang Bekleidungstechnik/Konfektion, 2016.

Korving, H. and Ottenhoff, E. Analysis of the causes of pump failure and differences of failure characteristics. *Water Science & Technology*, 57(8):1271–1276, 2008.

Mitchell, R.-L., Gunkel, M., Thamsen, P. U., and Waschnewski, J. Investigations into wastewater composition focusing on nonwoven wet wipes. *Water Convention, Singapore International Water Week*, July 2016.

Pöhler, M., Gerlach, S., Höchel, K., Mengdehl, T., and Thamsen, P. Linking efficiency to functional performance by a pump test standard for wastewater pumps. In *ASME/JSME/KSME 2015 Joint Fluids Engineering Conference, Seoul, South Korea*, July 26-31 2015 2015.

Thamsen, P. Cutting clogging in wastewater. *World Pumps*, April:22–25, 2009.

Thamsen, P., Tornow, M., Oesterle, M., and Rüdinger, K. Ensure reliable wastewater pumping research and experience in the context of lisa. *Singapore International Water Week*, 2009.

Paper D

Towards Simulation of Clogging Effects in Wastewater Pumps: Modelling of Fluid Forces on a Fiber of Bonded Particles using a Coupled CFD-DEM Approach

Anna Lyhne Jensen, Henrik Sørensen and Lasse Rosendahl

The paper was presented in
International Symposium on Transport Phenomena and Dynamics of Rotating Machinery, Honolulu, Hawaii, April 10-15, 2016

Towards Simulation of Clogging Effects in Wastewater Pumps: Modelling of Fluid Forces on a Fiber of Bonded Particles using a Coupled CFD-DEM Approach

Anna Lyhne Jensen, Henrik Sørensen, Lasse Rosendahl

Aalborg University, Department of Energy Technology, Pontoppidanstræde 111, DK-9220 Aalborg, Denmark

---

D.1 Abstract

Clogging in wastewater pumps is often caused by textile and other fibrous materials in the wastewater. As a step towards developing a methodology using the CFD-DEM approach for simulation of clogging effects, a fiber model consisting of a string of bonded DEM particles is developed in the software EDEM and coupled (two-way momentum exchange) to the CFD software ANSYS Fluent. The number of particle segments forming the fiber as well as the properties of fiber density and fiber stiffness are changed to identify the influnce of these properties on the fiber motion in shear flow. A change of density from 500 kg/m^3 *to 5000 kg/m*^{3} *strongly affects the motion of the fiber, while a change of the stiffness of the bonds between the spherical particles from 1e*^{7} *N/m*^{3} *to 1e*^{9} *N/m*^{3} *has less influence on the fiber motion. The results of using 20 and 50 fiber segments respectively are similar in the first period of simulation, but the deviation between the two cases increase with time. The difference may be caused by the difference in fiber aspect ratio in the two cases. The influence of fiber properties on fiber motion has been analysed quantitatively and compared to fiber orbit types presented in literature (Forgacs and Mason, 1959; Lindström and Uesaka, 2007). The results show that fiber motion similar to the motion presented in literature is obtained using a coupling between EDEM and ANSYS Fluent.*

D.2 Introduction

Clogging in wastewater pumps, due to objects such as textiles and plastic in wastewater, causes severe problems in wastewater pumping systems. Therefore, resilience to clogging is a key requirement in the design of wastewater pumps. The design process of wastewater pumps is commonly based on empirical knowledge and expensive and time consuming experiments on prototypes. Thus, a method for simulating clogging effects will significantly facilitate the design process.

Computational Fluid Dynamics (CFD) is widely used in the design process of pumps. However, simulation of clogging effects entails simulation of the objects in the wastewater causing clogging, such as plastic bags or textile. This fact significantly complicates the simulation, and therefore simulation of clogging effects in wastewater pumps has not previously been done. Different applicable approaches for simulation of the interaction between fluid and flexible materials exist. These include the Immersed Boundary Method (Peskin, 2002), the Arbitrary Lagrangian-Eulerian method (Sathe and Tezduyar, 2008), Smoothed Particle Hydrodynamics coupled with the Finite Element Method (Attaway et al., 1994) and coupled CFD-DEM, which has been discussed by Jensen et al. (2015). Advantages of using the CFD-DEM approach are that self-collision of the textile can be handled by the DEM soft-sphere collision model. Furthermore, it is advantageous that dynamic meshing is not required, since the DEM particles are not resolved by the CFD mesh. In the present study, a flexible fiber in shear flow is modeled using the DEM software EDEM from DEM Solutions in a two-way coupling to the CFD software ANSYS Fluent including fibre self-interactions. This model is the first step towards developing a CFD-DEM framework for simulation of flexible pieces of textile and the interaction of the textile with fluid applicable for simulation of clogging effects.

D.2.1 Bonded Discrete Elements

DEM was introduced by Cundall and Strack (1979) for the simulation of solid flows with mechanical transport. The method computes the motion of a large number of particles of finite size using Newtons 2. law of motion as given in Eq. (D.1) and (D.2)

$$m_\mathrm{i}\vec{a}_\mathrm{i} = \vec{F}_\mathrm{i,n} + \vec{F}_\mathrm{i,t} + \vec{F}_\mathrm{i,b}\,, \tag{D.1}$$

$$I_\mathrm{i}\vec{\alpha}_\mathrm{i} = \vec{r}_\mathrm{i,c} \times \vec{F}_\mathrm{i,t}\,, \tag{D.2}$$

where m_i is the mass and a_i is the acceleration of the i^th particle. $F_\mathrm{i,n}$ and $F_\mathrm{i,t}$ are the normal and tangential particle-particle contact forces and $F_\mathrm{i,b}$ is additional forces as gravity and fluid force. In Eq. D.2, I_i and $\vec{\alpha}_\mathrm{i}$ are the moment of inertia and the angular acceleration of the i^{th} particle respectively, and $r_\mathrm{i,c}$ is a vector from the center of the particle to the point where the force $F_\mathrm{i,t}$ acts.

When modeling a fiber as a chain of bonded spherical DEM particles, a second model for particle-particle interaction of the bonded particles must be introduced. Since the fiber is not completely flexible, normal and shear stiffness of the fiber are introduced in the model of the bonds between the particles. Thus, bonded particles resist normal and tangential displacements.

Furthermore, the bond breaks if a specified normal or tangential limit for stress is exceeded. Existing bond models in DEM have primarily been developed for simulation of rock and concrete. This also applies to the build in bond model in the software EDEM, "Hertz-Mindllin with bonding", which is a modification of the bond model for rock proposed by Potyondy and Cundall (2004). Guo et al. (2013) used DEM to model flexible fibers. The bond model used by Guo et al. (2013) was also based on the bond model proposed by Potyondy and Cundall (2004) and the results showed good correspondence between theory and model. Further validation of the bond model in EDEM for the use for flexible fibers is necessary, but out of scope of this paper.

Fig. D.1 illustrates a bond between two particles of a fiber. A bond is formed if the contact radii r_c of two particles overlap. The radius r is the particle radius and is used for force calculation between particles.

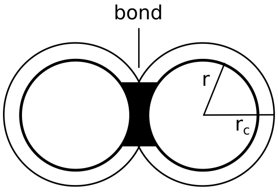

Fig. D.1: The particle radius, r, and the contact radius r_c is defined when modeling bonded particles. Bonds are formed if there is particle contact within the radius r_c. Bond properties include normal and shear stiffness of the bond and critical shear and normal stress break criteria.

D.2.2 Flexible Fibers in Shear Flow

The DEM fiber model will be coupled to a CFD simulation of shear flow as sketched in Fig. D.2.

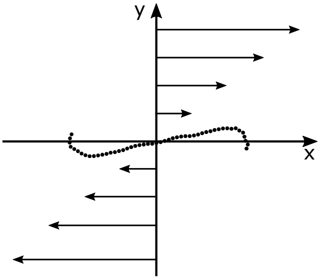

Fig. D.2: Flexible fiber orbiting in shear flow.

Previous work on fibers in shear flow includes Forgacs and Mason (1959), who investigated the motion of flexible wood-pulp fibers in shear suspensions experimentally. More recently, the motion has been modeled by Yamamoto and Matsuoka (1993) and Schmid et al. (2000) by dividing the fiber into spherical and cylindrical bonded segments respectively, and modelling the hydrodynamic force on these segments. Lindström and Uesaka (2007) also modeled fibers as chains of cylindrical fiber segments. In this model the flow was modeled by 3D incompressible Navier-Stokes equations using a two-way coupling between the fiber and the fluid. The model took into account both viscous and dynamic drag forces. An important conclusion of the work was that fiber motion cannot be described without taking two-way coupling into account. Based on this, a two-way coupling between the fluid and the fiber is implemented in the present work.

Different orbit types depending on the flexibility of the fiber was characterized by Forgacs and Mason (1959). These are rigid orbits, springy orbits, snake orbits and coiled orbits. These orbit types are sketched in Figure D.3. The stiffness of the fiber increases from the coiled orbit type down to the rigid orbit type. Notice from the figure that rigid, springy and snake orbits are periodic. The present simulation of fibers in shear flow in EDEM and ANSYS Fluent is validated by qualitatively comparing the results to the different orbit regimes by Forgacs and Mason (1959) and Lindström and Uesaka (2007).

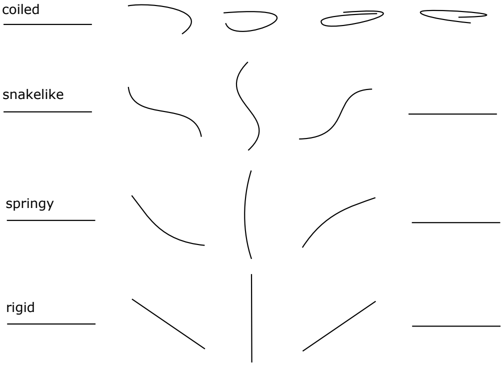

Fig. D.3: Sketch of four different orbit types of fibres in shear flow: rigid, springy, snakelike and coiled (Forgacs and Mason, 1959; Lindström and Uesaka, 2007).

The diameter of fibers in pulp and paper industry is in the order of 10^{-5}m. The aim of this work is to simulate one yarn of a floor cloth which has a diameter in the order of 10^{-3}m. Therefore the size scale differs significantly, but it is expected that the yarn will orbit in a way similar to that of the fibers. The fiber stiffness, density and the number of particles forming the fiber are changed, and the influence of these changes on the fiber motion is investigated to assess the applicability of the present bond model and coupling in EDEM and ANSYS Fluent, to simulation of flexible fibers or textiles in fluid flow.

D.3 Methods

Navier-Stokes equations for an incompressible fluid with particles are given in Eq. (D.3) and Eq. (D.4) (Kloss et al., 2012)

$$\frac{\partial \alpha_\mathrm{f}}{\partial t} + \nabla \cdot (\alpha_\mathrm{f} \vec{u}_\mathrm{f}) = 0\,, \tag{D.3}$$

$$\frac{\partial \left(\alpha_\mathrm{f} \vec{u}_\mathrm{f}\right)}{\partial t} + \nabla \cdot (\alpha_\mathrm{f} \vec{u}_\mathrm{f} \vec{u}_\mathrm{f}) = -\alpha_\mathrm{f} \nabla \frac{p}{\rho_\mathrm{f}} - \frac{\vec{R}_\mathrm{pf}}{\rho_\mathrm{f}} + \nabla \cdot \tau\,, \tag{D.4}$$

where α_f, $\vec{u}_\mathrm{f}$ and ρ_f is the is the fluid volume fraction, fluid velocity and fluid density respectively. $\tau = v_\mathrm{f} \nabla \vec{u}_\mathrm{f}$ is the fluid phase stress tensor and $\vec{R}_\mathrm{pf}$ is the fluid-particle momentum exchange. Figure D.4 illustrates the calculation steps in a coupled CFD-DEM simulation. The simulation starts in the CFD solver, which calls the DEM solver. In the CFD solver the containing cell of each particle is identified and the particle volume fraction in each cell is determined. Based on the volume fraction, the fluid force in each cell can be determined. In the present work, this corresponds to the drag force. Finally, the CFD solver determines the particle-fluid momentum exchange and the fluid velocity before the fluid force is transferred to the DEM solver. The CFD time step is larger than the DEM time step and thus the DEM calculations are repeated until the time which corresponds to a CFD time step have been completed. Then the velocity, position and radius of all particles are transferred to the CFD solver.

D.3.1 Domain and Boundary Conditions

The domain and boundary conditions used in CFD are presented in Fig. D.5. Periodic boundary conditions are used in the right and left part of the domain and symmetry is used on the front and back of the domain. The moving walls in the upper and lower part of the domain create a shear flow as sketched in Fig. D.2. The velocity profile is linear and is given by Eq. D.5

$$v_\mathrm{x} = a \cdot y\,, \tag{D.5}$$

where v_x is the velocity in the $x-$direction and y is the position on the $y-$axis. A constant value of $a = 2.5$ is used in all the described simulations, and the role of shear rate will not be investigated. Furthermore, gravity is not included in the simulation.

The domain is meshed with hexahedral cells of equal size. The ratio between the particle volume and cell volume is approximately 1/15.

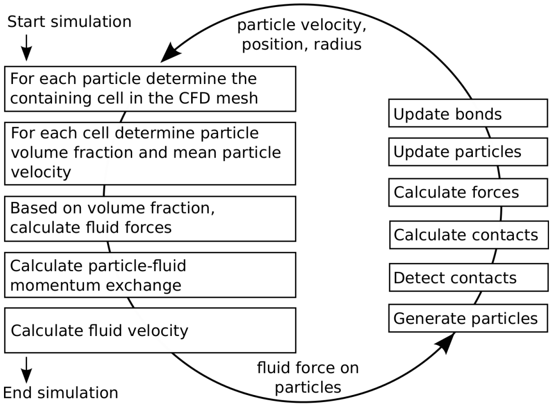

Fig. D.4: Block diagram of calculation process in a coupled CFD-DEM simulation. The blocks to the left represent the CFD solver and the blocks to the right represent the DEM solver.

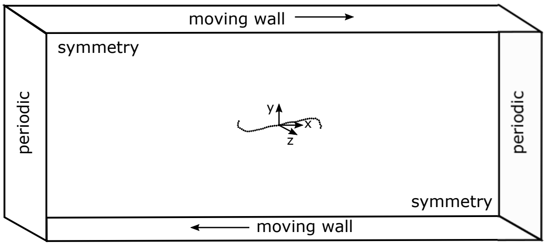

Fig. D.5: CFD domain. The upper and lower boundaries are moving walls with no slip. This creates a shear flow in the domain. The right and left part of the domain has periodic boundary conditions. The fiber of DEM particles orbits in the center of the domain.

D.3.2 Fiber Model

The model of the mechanics of fibers include particle-particle interaction through bonds or collision, and drag force on the fiber. Morphological properties of the fiber such as length and diameter as well as the fiber stiffness and density are expected to have a major influence on resulting fiber orbit types. These parameters are varied and the influence on the fiber motion is evaluated. The diameter of the spherical particle segments forming the fiber is 2.5 mm, to resemble the size of the yarns of a woven floor cloth. The contact radius is set to be 20 % larger than the particle radius. Furthermore, the number of particle segments forming the fiber is 20 or 50, resulting in aspect ratios of 20 and 50 respectively. Fiber aspect ratios between 50 and 780 were investigated by Forgacs and Mason (1959), Schmid et al. (2000) and Salinas and Pittman (1981).

D.3.3 Drag Model

Using the CFD-DEM approach, the bonded particles are not resolved by the CFD mesh. Therefore a drag law must be ascribed to the particles. The coupling framework for EDEM and Fluent includes a freestream drag formulation as well as formulations of drag developed by Ergun (1952) and Wen and Yu (1966) and di Felice (1994) for fluid particle interaction in packed and fluidized beds. No drag formulation for the modeling of bonded particles is available. In the freestream drag formulation, the drag coefficient depends on the Reynolds number. The Reynolds number is based on the particle diameter, d_p, and is calculated as given in Eq. D.6.

$$Re = \frac{\rho_\mathrm{f} \cdot v_\mathrm{rel} \cdot d_\mathrm{p}}{\mu_\mathrm{f}} \tag{D.6}$$

Where v_rel is the relative fluid velocity, and ρ_f and μ_f are the fluid density and viscosity respectively. The drag coefficient is calculated based on the classical formulation of drag on a sphere, using Eq. D.7.

$$c_\mathrm{d} = \begin{cases} 24/Re, & \text{if } Re \leq 0.5; \\ 24 \cdot \left(1 + 0.15 \cdot Re^{0.687}\right)/Re, & \text{if } 0.5 < Re \leq 1000; \\ 0.44, & \text{otherwise.} \end{cases} \tag{D.7}$$

Using the drag coefficients determined for each particle by Eq. D.7, the drag force on each particle of the fiber can be calculated by Eq. D.8

$$F_\mathrm{d} = 0.5 \cdot c_\mathrm{d} \cdot \rho_\mathrm{f} \cdot A \cdot v_\mathrm{rel}\,, \tag{D.8}$$

where A is the particle area. The viscosity of the water is 0.001003 kg/m·s and the density is 998.2 kg/m^3. The drag force on the particles is used to determine the particle-fluid momentum exchange.

D.4 Results and Discussion

13 different fibers were simulated by varying the fiber density, bond shear and normal stiffness and number of fiber segments. The initial orientation of the fiber is vertical, perpendicular to the flow direction. The results are presented in Fig. D.6 for a fiber formed by 50 segments and in Fig. D.7 for a fiber formed by 20 segments. The figures show the initial state of the fiber and 10 following states. The time interval between the fibers in each case is 1 s. The properties of the fiber in each of the cases shown in Fig. D.6 are listed

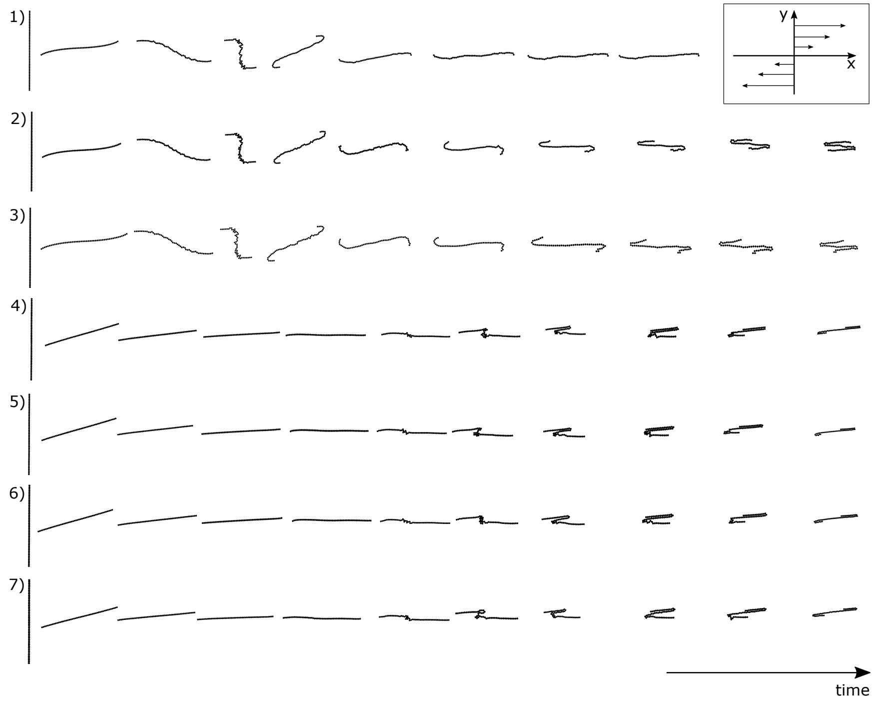

Fig. D.6: Development of the fiber shape with time in the different cases. The time interval between each image in a case is 1 s.

in Tab. D.1. Note that since the fiber consists of spherical particles, the aspect ratio of the fiber is equal to the number of particle segments.

The movement of the fibers in case 1-3 is very similar, especially for the first 4 s. Common for the three fibers is the density of 5000 kg/m^3, which gives a density ratio between the fibers and the fluid close to 5. The difference between the three cases is the fiber stiffness. The fiber in the first case is the most flexible. This is evident from the results where the shear flow causes the fiber to continue the rotation in an orbit which resembles a cross between the snakelike motion and the coiled motion sketched in Fig. D.3. The least flexible fiber (case 1), stops rotating in the area of low fluid velocity in the center of the domain.

A standard floor cloth has a dry density of around 150 kg/m^3. When submersed in water the cloth will absorb water and the wet density of the cloth will be higher than the dry density. In case 4-6 it is assumed that the wet density of the cloth is around 500 kg/m^3, and in the 7$^{\text{th}}$ case the fiber and the fluid is assumed to have the same density. The results of case 4-7 are very similar, indicating that the difference in density from 500 kg/m^3 to 1000 kg/m^3 has a limited influence on the results. However, comparing to cases

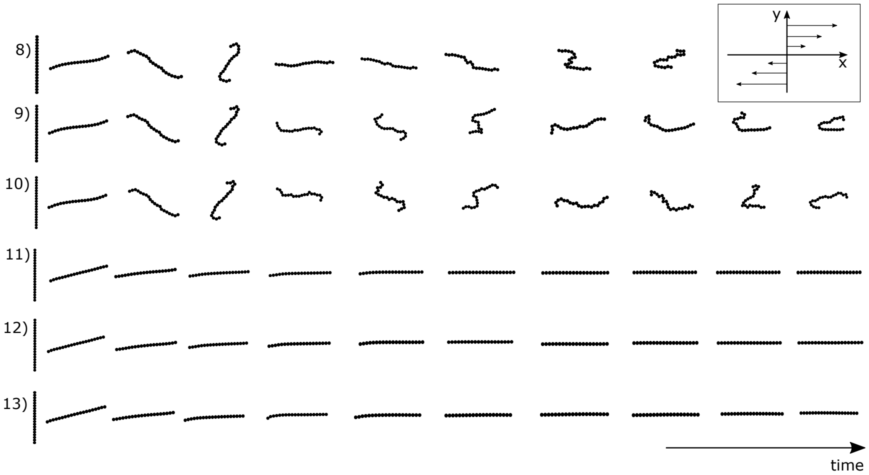

Fig. D.7: Development of the fiber shape with time in the different cases. The time interval between each image in a case is 1 s.

1-3, with a fiber density of 5000 kg/m^3 and same range of fiber stiffness, the difference due to change in density is obvious, as the motion of the fibers in case 4-7 resembles the orbit of a rigid fiber until the fiber is parallel to the flow direction. After this, the fiber motion is similar to a coiled orbit with self entanglement. Case 4-6 differ in the fiber stiffness from $1e^7$ to $1e^9$. But this change in fiber stiffness is not evident from the results.

The motion of the fibers formed by 20 fiber segments, illustrated in Fig. D.7, is very similar to the fiber formed of 50 segments for the first 5 s. Both for a fiber density of 500 and 5000 kg/m^3. This indicates that the number of segments forming the fiber is of small importance in this case. However, there are significant differences between fibers of 20 and 50 segments after 5 s of the simulation. This may be caused by a significant change in fiber aspect ratio, when reducing the number of fiber segments. The diameter of the fiber is kept constant at 2.5 mm in all simulations and consequently the aspect ratio of the fiber changes when the number of spherical segments forming the fiber is reduced from 50 to 20. A more direct comparison of the influence of fiber density and stiffness is presented in Fig. D.8 and D.9.

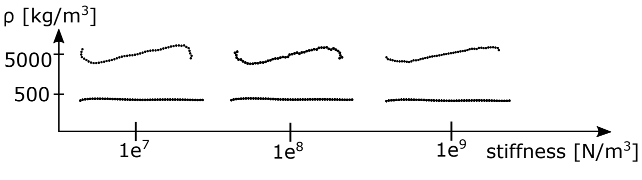

Fig. D.8: Comparison of fibers formed by 50 segments after 4 s.

Table D.1: Properties of the simulated fibers.

Fiber Simulation Cases					
Case	Density [kg/m^3]	Stiffness [N/m^3]	Segments [-]	Diameter [m]	Length [m]
1	5000	$1e^9$	50	0.0025	0.125
2	5000	$1e^8$	50	0.0025	0.125
3	5000	$1e^7$	50	0.0025	0.125
4	500	$1e^9$	50	0.0025	0.125
5	500	$1e^8$	50	0.0025	0.125
6	500	$1e^7$	50	0.0025	0.125
7	1000	$1e^9$	50	0.0025	0.125
8	5000	$1e^9$	20	0.0025	0.050
9	5000	$1e^8$	20	0.0025	0.050
10	5000	$1e^7$	20	0.0025	0.050
11	500	$1e^9$	20	0.0025	0.050
12	500	$1e^8$	20	0.0025	0.050
13	500	$1e^7$	20	0.0025	0.050

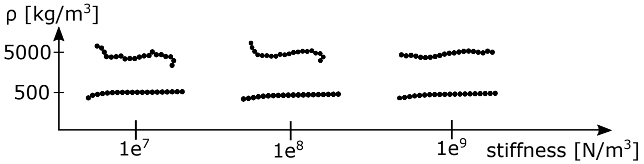

Fig. D.9: Comparison of fibers formed by 20 segments after 4 s.

The figures illustrate the shape of the fiber after 4 s of the simulation. It is seen from both Fig. D.8 and D.9 that the fiber stiffness slightly changes the motion of the fiber. Furthermore, a significant difference is evident with a change of fiber density from 500 to 5000 kg/m^3.

D.5 Conclusion

The software EDEM for DEM and the software ANSYS Fluent for CFD were used to simulate fibers in shear flow with a two-way coupling between fiber and fluid, to identify the importance of the fiber properties on the motion of the fiber in this flow condition.

A change in fiber density from 500 to 5000 kg/m^3 leads to a significant change in the fiber motion in shear flow. With a fiber density of 5000 kg/m^3 the motion of the fiber resembles the springy or snakelike orbit type reported in literature. In the case of a fiber density of 500 kg/m^3 the motion is more similar to rigid orbiting. However, in the case of 50 particle segments, this motion changes to coiled orbiting.

Changing the stiffness of the bonds between the particles from 1e^7 N/m^3 to 1e^9 N/m^3 only has a very limited influence on the results. A change in the number of particles forming the bond, from 50 to 20 gives similar results in the first half of the simulated time, but the difference between the results may be caused by the change in fiber aspect ratio.

This study has presented a qualitative comparison of fiber motion of fibers with different properties as well as comparison to fiber orbit types presented in literature. In order to determine if the built-in bond model and coupling in EDEM and ANSYS Fluent is applicable for clogging simulations, careful experimental validation of the motion of fibers with specific properties is needed. Furthermore, settling experiments or similar must be conducted for a model of a piece of textile. However, the presented results of fiber motion in shear flow, are similar to results presented in literature. This is promising for the future application of coupled CFD-DEM to model fiber motion and later simulation of clogging effects in wastewater pumps.

D.6 Future Work

The presented simulation of fibers in shear flow is the first step towards developing a framework for simulation of clogging effects in wastewater pumps. In order to accomplish this, experimental validation of both the coupling between CFD and DEM and the bond model in DEM for this application must be conducted. Based on the results of the validation, development and implementation of a new formulation of drag and DEM bonds may be necessary.

D.7 Acknowledgments

This work is funded by Grundfos in cooperation with the Department of Energy Technology in Aalborg University.

References

Attaway, S., Heinstein, M., and Swegle, J. Coupling of smooth particle hydrodynamics with the finite element method. *Nuclear Engineering and Design*, 150(2-3):199–205, 1994.

Cundall and Strack. A discrete numerical model for granular assemblies. *Geotechnique*, 29:47–65, 1979.

Ergun, S. Fluid flow through packed columns. *Chemical Engineering Progress*, 48:89–94, 1952.

di Felice, R. The voidage function for fluid-particle interaction systems. *International Journal of Multiphase Flow*, 20:153–159, 1994.

Forgacs, O. and Mason, S. Particle motions in sheared suspensions. *Journal of Colloid Science*, 14:473–491, 1959.

Guo, Y., Wassgren, C., Hancock, B., Ketterhagen, W., and Curtis, J. Validation and time step determination of discrete element modelling of flexible fibers. *Powder Technology*, 249(2013):386–395, 2013.

Jensen, A., Sørensen, H., Rosendahl, L., and Lykholt-Ustrup, F. Towards simulation of clogging effects in wastewater pumps: A review of the state-of-the-art in cloth modelling and challenges in the simulation of clogging effects. *ASME-JSME-KSME 2015 Joint Fluids Engineering Conference*, pages 2543–2549, 2015.

Kloss, C., Goniva, C., Hager, A., Amberger, S., and Pirker, S. Models, algorithms and validation for opensource dem and cfd-dem. *Progress in Computational Fluid Dynamics*, 12:140–152, 2012.

Lindström, S. and Uesaka, T. Simulation of the motion of flexible fibers in viscous fluid flow. *Physics of Fluids*, 19(11):113307, 2007.

Peskin, C. The immersed boundary method. *Acta Numerica*, 11:479–517, 2002.

Potyondy, D. and Cundall, P. A bonded particle model for rock. *Int. J. Rock Mech. Min. Sci.*, 41:1329–1369, 2004.

Salinas, A. and Pittman, J. Bending and breaking of fibers in sheared suspensions. *Polymer Engineering and Science*, 21:23–31, 1981.

Sathe, S. and Tezduyar, T. Modelling of fluid-structure interactions with the space-time finite elements: Contact problems. *Computational Mechanics*, 43 (1):51–60, 2008.

Schmid, C., Switzer, L., and Klingenberg, D. Simulations of fiber flocculation: Effects of fiber properties and interfiber friction. *Journal of Rheology*, 44(4): 781–809, 2000.

Wen, C. and Yu, Y. Mechanics of fluidization. *Chemical engineering progress symposium*, 62:100–111, 1966.

Yamamoto, S. and Matsuoka, T. A method for dynamic simulation of rigid and flexible fibers in a flow field. *The Journal of Chemical Physics*, 98(1): 644–650, 1993.

Paper E

Towards Simulation of Clogging Effects in Wastewater Pumps: A Review of the State-of-the-Art in Cloth Modelling and Challenges in the Simulation of Clogging Effects

Anna Lyhne Jensen, Lasse Rosendahl, Henrik Sørensen and
Flemming Lykholt-Ustrup

The paper has been published in the
ASME-JSME-KSME Joint Fluids Engineering Conference 2015, vol. 1: Symposia,
pp. 2543–2549, Seoul, South Korea, July 26-31, 2015,
https://doi.org/10.1115/AJKFluids2015-33214

Towards Simulation of Clogging Effects in Wastewater Pumps: A Review of the State-of-the-Art in Cloth Modelling and Challenges in the Simulation of Clogging Effects

Anna Lyhne Jensen[a], Lasse Rosendahl[a], Henrik Sørensen[a], Flemming Lykholt-Ustrup[b]

[a] *Aalborg University, Department of Energy Technology, Pontoppidanstræde 111, DK-9220 Aalborg, Denmark*
[b] *GRUNDFOS Holding A/S, Wastewater Hydraulics, Poul Due Jensens Vej 7, DK-8850 Bjerringbro, Denmark*

Abstract

Simulation of clogging effects caused by cloths in wastewater pumps enables a faster and cheaper design process of wastewater pumps, which potentially leads to a reduction in the occurrence of clogging. Four potential methods for cloth simulation are reviewed and the challenges of each method are identified and compared. These methods are the Arbitrary Lagrangian-Eulerian (ALE) method, Immersed Boundary (IB) method, Smoothed Particle Hydrodynamics (SPH) coupled with the Finite Element method (FEM), and Computational Fluid Dynamics (CFD) coupled with the Discrete Element method (DEM). Each method has advantages and disadvantages, and each of them may prove to be applicable for the application. The CFD-DEM approach is chosen for future work.

E.1 Introduction

In the past, when energy was cheap and accessible, the efficiency of pumps was of minor importance. Today, with diminishing reserves of fossil fuels and pollution dominating the political and public debate, a major effort is applied to improve pump efficiency. With increasing computer power, and the development of computational methods for calculations on flow in complex geometries, design and optimisation of pumps have become widely based on simulations.

However, for wastewater pumps a high efficiency is insignificant if the pump is prone to clogging. Clogging is caused by fibrous material in the wastewater and causes reduced flow through the pump, increased power consumption, and ultimately a complete stop. A very high cost of system maintenance and downtime underlines the importance of minimising the occurrence of this failure. This can be achieved by identifying features in the design stage, which make wastewater pumps more resilient to clogging.

So far, reliable simulation of clogging effects has not been possible and therefore new designs of wastewater pumps have to be tested experimentally on a prototype. Since clogging is often caused by cloth or fabric in the wastewater entering the pump, floor-cloths are currently used in clogging tests on new pump designs. Therefore, in order to simulate this test, a reliable, physical cloth model and fluid-cloth coupling must be developed.

E.1.1 Challenges in Cloth Simulation

A cloth entering a pump may be exposed to large deformations, extensive self-collision, and twisting. Therefore, model stability and collision handling is of major importance and additinaly a physically consitent cloth model at these conditions must be ensured.

Furthermore, even though a two-way coupling between fluid and cloth complicates numerical modelling significantly, it must be included to ensure physically accurate simulations. Thereby, the problem becomes a complicated fluid structure interaction problem were large deformations of the structure occurs.

The following points summarises the challenges in the development of a cloth simulation to determine if new designs of wastewater pumps are resilient to clogging.

- Collision detection and handling
- Stability
- Fluid-cloth interaction

E.2 Simulation Approaches

Various approaches, which are potentially applicable for the present work, have been used in other fields such as cloth simulation in computer graphics (Breen et al., 1994; Bridson et al., 2002) and modelling of fibres for the paper and pulp industry (Andric, 2012). Depending on the choice of method, different challenges will occur. This paper describes and compares state-of-the-art and applications of four groups of methods:

- Arbitrary Eulerian-Lagrangian (ALE) method
- Immersed Boundary (IB) method
- SPH-FEM coupling

- CFD-DEM coupling

Each of the methods is presented along with examples of applications in literature and a discussion of the main challenges arising with the method.

E.2.1 Arbitrary Lagrangian-Eulerian Method

The Arbitrary Lagrangian-Eulerian (ALE) method is widely used in fluid-structure interaction problems. In this method a moving mesh of finite elements resolves the fluid domain with a continuum such as a cloth, and the mesh adapts to deformations of the continuum.

Combining the Lagrangian and Eulerian methods the mesh nodes on the deforming continuum can be moved with the continuum in a Lagrangian way, be fixed in an Eulerian way or be moved in an arbitrary way which enables the mesh to maintain a high quality as the continuum deforms. A rough skectch of the method is presented in Fig. 1, illustrating the motion of the Eulerian mesh nodes and the Lagrangian points in time. Note that the mesh nodes are moved arbitrarily between the material points.

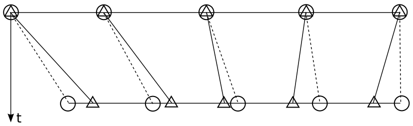

Fig. E.1: Sketch of the ALE method. Mesh points can be moved arbitrarily to maintain a high mesh quality. △ material point, ◯ mesh node, - - - - - mesh motion, —— particle motion Donea et al. (2004).

Since the deformable body is resolved by a moving mesh, difficulties are encountered when the body twists or collides. This causes the mesh to become highly distorted leading to inaccurate solutions or to failure. Remeshing is very computationally expensive, but it is commonly used when the quality of the mesh is getting low. However, remeshing can not solve the problems arising when large cloth deformations will lead to self collision. In spite of this, Sathe and Tezduyar (2008) succesfully used a moving-mesh technique to model a cloth piece falling over a rigid rod using a contact algorithm to maintain a small distance between the colliding structures to prevent collision.

An advantage of using the ALE method is the strong coupling between the immersed body and the fluid since the body is fully resolved by the Eulerian mesh. However, handling of collision, buckling and twisting is troublesome and thus this method is not considered appropriate for the modelling of a cloth in a pipe or pump system.

E.2.2 Immersed Boundary Method

The classic immersed boundary method for the simulation of fluid-structure interaction was developed by Peskin (1972) for simulating the interaction between blood and heart valves. The method is applicable for flow with elastic boundaries and enables handling of complex and deformable geometries without need for dynamic remeshing. It uses a fixed cartesian mesh to resolve the fluid flow and Lagrangian markers interconnected by an elastic law to resolve the interface between fluid and solid. The immersed boundary does not cause mesh deformation as it moves or deforms. This is sketched for a deformable fibre and a cartesian Eulerian mesh in Fig. E.2.

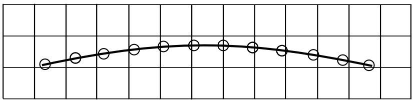

Fig. E.2: Fibre modelled as immersed boundary with lagrangian markers ○.

In the IB method the motion of the fluid phase is governed by the Navier-Stokes equations, given in Eq. (E.1) and (E.2).

$$\rho\left(\frac{\partial\vec{u}}{\partial t}+\vec{u}\cdot\nabla\vec{u}\right)+\nabla p=\mu\Delta\vec{u}+\vec{f} \tag{E.1}$$

$$\nabla\cdot\vec{u}=0 \tag{E.2}$$

Where ρ is the fluid density, $\vec{u}$ is velocity, p is the pressure, μ is the dynamic viscosity, and $\vec{f}$ is a force term.

Furthermore, the location of the immersed object in Fig. E.2 is tracked with massless Lagrangian points marked on the interface. The interaction equations between immersed boundary and fluid are given by Eq. (E.3)-(E.5) (Peskin, 2002).

$$\rho\left(\vec{x},t\right)=\int M\left(q,r,s,t\right)\delta\left(\vec{x}-\vec{X}\left(q,r,s,t\right)\right)\mathrm{d}q\mathrm{d}r\mathrm{d}s \tag{E.3}$$

$$\vec{f}\left(\vec{x},t\right)=\int\vec{F}\left(q,r,s,t\right)\delta\left(\vec{x}-\vec{X}\left(q,r,s,t\right)\right)\mathrm{d}q\mathrm{d}r\mathrm{d}s \tag{E.4}$$

$$\frac{\partial\vec{X}}{\partial t}\left(q,r,s,t\right)=\int\vec{u}\left(q,r,s,t\right)\delta\left(\vec{x}-\vec{X}\left(q,r,s,t\right)\right)\mathrm{d}\vec{x} \tag{E.5}$$

Where δ is the Dirac delta function, ρ is the Eulerian density, M is the Lagrangian mass density of the material, f is the Eulerian density of the elastic force, F is a Lagrangian variable of the elastic force density, $\vec{x}$ is Eulerian points and $\vec{X}$ is Lagrangian points on the immersed boundary.

Since the introduction of the Immersed Boundary method it has been further developed into different variants specialised for several different applications, which have been reviewed by Mittal and Iaccarino (2005) and

Sotiropoulos and Yang (2014). Examples of applications of the immersed boundary method, which have similarities to the simulation of a cloth, includes Zhu and Peskin (2002) and Zhu and Peskin (2003) who simulated flapping filaments in flowing soap film, Stockie and Green (1998) who simulated the motion of flexible pulp fibres in a two dimensional shear flow, Kim and Peskin (2009) who modelled a parachute in three dimensions, and simulation of cloths in a washing machine by Akcabay (2007).

The aim of the work by Akcabay (2007) most closely resembles the aim of simulating a cloth in a pipe of pump system. The cloths were modelled as very deformable elastic impermeable thin membranes. The fluid was modelled as incompressible and viscous and the moving surfaces of the washing machine were modelled using a cartesian domain-mapping technique, so that remeshing is not needed.

The succesfull application of the immersed boundary method is promising for the possibility of handling the modelling challenges of collision detection and handling, stability during cloth buckling and twisting, fluid-cloth interaction and physically consistent cloth properties.

E.3 SPH-FEM Coupling

Smoothed Particle Hydrodynamics (SPH) is a meshless Lagrangian method first proposed by Lucy (1977) and Gingold and Monaghan (1977) independently to solve astrophysical problems. It has since been developed and applied to free surface flows among other things.

Using this method coupled with FEM, the fluid is modelled as smoothed particles while the cloth is modelled as an FEM surface. The steps of the coupled SPH-FEM method are presented in Fig. E.3. The left column respresents the computations in the SPH solver while the right column represents the computations in the FEM solver.

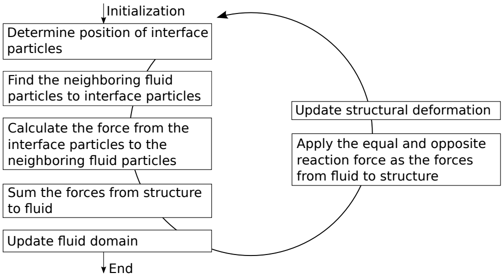

Fig. E.3: Coupling between SPH and FEM based on Yang et al. (2012).

For the computations in the fluid phase a smoothing kernel function W determines the width of the influencing area of a fluid particle and the function f is interpolated at a position x using the neighbouring fluid particles. The smoothing kernel function must among other things be normalised, monotonically decreasing, symmetric and must satisfy the Dirac delta function as the smoothing length goes to 0. More detail about smoothing kernel functions in SPH can be found in the work by Liu et al. (2003).

A summation interpolant containing the smoothing kernel function is given in Eq. (E.6). This is used to interpolate a function f at the point x.

$$f(x) = \sum_{\mathrm{j}} m_{\mathrm{j}} \frac{f_{\mathrm{j}}}{\rho_{\mathrm{j}}} W(|\vec{r}|, h) \tag{E.6}$$

Where f_{j} is the function value of particle j at the interpolation point x, h is the support radius, m_{j} is the mass of particle j, and ρ_{j} is the density particle j. $\vec{r}$ is the vector between the interpolation point and particle j.

The coupling between SPH and FEM was proposed by Attaway et al. (1994). The method has been used by Vuyst et al. (2005) and Yang et al. (2012) for fluid structure interaction problems for free surface flows.

E.4 CFD-DEM Coupling

In the field of computer graphics, Breen et al. (1994) and Eberhardt et al. (1996) among others have succesfully developed cloth models based on particle systems, where the connections between the particles are modelled as experimentally obtained energy functions. This particle system approach inspires to the use of the Discrete Element Method (DEM) to model the cloth as a set of interconnected particles.

DEM was introduced by Cundall and Strack (1979) for granular media. It computes the motion of a large number of particles of finite size using Newtons 2. law of motion as given in Eq. (E.7)-(E.8).

$$m_{\mathrm{i}}\vec{a}_{\mathrm{i}} = \vec{F}_{\mathrm{i,n}} + \vec{F}_{\mathrm{i,t}} + \vec{F}_{\mathrm{i,f}} + \vec{F}_{\mathrm{i,b}} \tag{E.7}$$

$$I_{\mathrm{i}}\vec{\alpha}_{\mathrm{i}} = \vec{r}_{\mathrm{i,c}} \times \vec{F}_{\mathrm{i,t}} + \vec{T}_{\mathrm{i,r}} \tag{E.8}$$

Where m_{i} and a_{i} are the mass and acceleration of the i^{th} particle. $F_{\mathrm{i,n}}$ and $F_{\mathrm{i,t}}$ are the normal and tangential particle-particle contact force respectively. $F_{\mathrm{i,f}}$ is the fluid force on the particle and $F_{\mathrm{i,b}}$ includes other forces, such as gravity. I_{i} is the moment of inertia and $\vec{\alpha}_{\mathrm{i}}$ is the angular acceleration of the i^{th} particle, $r_{\mathrm{i,c}}$ is a vector from the center of the particle to the point where $F_{\mathrm{i,t}}$ acts and $\vec{T}_{\mathrm{i,r}}$ is an additional torque which can be used to model non-sphericity.

The Discrete Element method accounts for particle-particle interaction. However, it does not include modelling of the fluid surrounding the particles. Therefore, DEM must be coupled with Computational Fluid Dynamics (CFD) to include the flow field around the cloth. Fig. E.4 illustrates a fibre modelled as a string of interconnected particles and the Eulerian mesh to resolve the fluid phase.

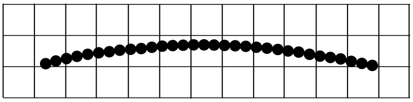

Fig. E.4: Fibre modelled as a collection of interconnected discrete particles in an eulerian mesh resolving the fluid.

The steps of a CFD-DEM coupling are sketched in Fig. E.5, where the left column represents the computations made in the CFD solver and the right column represents the computations made in the DEM solver. The

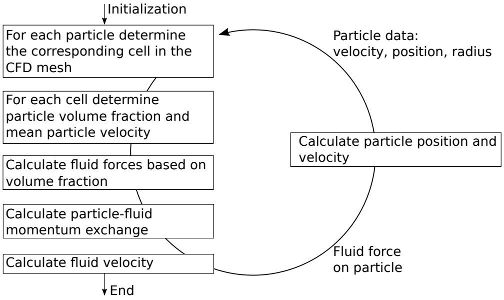

Fig. E.5: Coupling between CFD and DEM, based on Kloss et al. (2012).

Navier-Stokes equations for an incompressible fluid with immersed particles are given in Eq. (E.9) and Eq. (E.10) (Kloss et al., 2012).

$$\frac{\partial \alpha_{\mathrm{f}}}{\partial t} + \nabla \cdot (\alpha_{\mathrm{f}} \vec{u}_{\mathrm{f}}) = 0 \tag{E.9}$$

$$\frac{\partial \left(\alpha_{\mathrm{f}} \vec{u}_{\mathrm{f}}\right)}{\partial t} + \nabla \cdot (\alpha_{\mathrm{f}} \vec{u}_{\mathrm{f}} \vec{u}_{\mathrm{f}}) = -\alpha_{\mathrm{f}} \nabla \frac{p}{\rho_{\mathrm{f}}} - \vec{R}_{\mathrm{pf}} + \nabla \cdot \tau \tag{E.10}$$

Where α_{f}, $\vec{u}_{\mathrm{f}}$ and ρ_{f} is the is the fluid volume fraction, fluid velocity and fluid density respectively. $\tau = v_{\mathrm{f}} \nabla \vec{u}_{\mathrm{f}}$ is the fluid phase stress tensor and $\vec{R}_{\mathrm{pf}}$ is the fluid-particle momentum exchange. The momentum exchange is calculated in each cell from the drag forces on the particles in the cell.

Zhu et al. (2007) reviewed the applications of DEM and DEM coupled with CFD. Coupling between CFD and DEM is widely used in various industrial applications. Particularly in the modelling of fluidised beds as by Tsuji et al. (1993). As opposed to the spherical particles modelled in fluidised beds, a cloth is a non-spherical object with a complex mechanical behavior. This makes the coupling and modelling of the fluid forces on the cloth a major challenge. CFD-DEM coupling does not resolve fluid flow on sub particle level and therefore a drag law must be ascribed to the particles. In the modelling of fluidised beds with spherical particles, drag laws can be found in literature (Tsuji et al., 1993). For non-spherical and deformable bodies the prediction of drag force is very complex. This is due shape and orientation dependency of the drag coefficient. This have been investigated for a flexible fibre by several authors. Alben et al. (2002) experimentally investigated the shape of a flexible fibre immersed in flowing soap film at different velocities with the purpose of measuring the drag reduction caused by bending of the fibre. This case is similar to a cloth deforming as it moves in water. Yamamoto and Matsuoka (1993) modelled a fibre in a flow field as a string of interconnected rigid bodies and simulated the dynamic behavior of the fibre in a flow field with at low Reynolds numbers. Lindström and Uesaka (2007) further developed the fibre model and included particle intertia and hydrodynamic interaction between the fibres. Furthermore, they extended the range of Reynolds numbers and took a two-way coupling between fluid and cloth into account. These investigations of fluid-fibre interaction can form basis of a formulation of the drag force on a cloth which is basically a collection of several fibres forming a surface.

For a cloth modelled as a particle system, drag should ideally be modelled for each particle. Other forces occurring due to particle-fluid interaction include lift force, buoyancy force, added mass force, and history force.

E.5 Comparison

Four distinct methods which are potentially applicable for modelling of a cloth entering a wastewater pump have been reviewed. These modelling approaches differ in the meshing of the fluid phase, modelling of the cloth and the coupling between cloth and fluid.

Table 1 summarises the advantages and disadvantages of the mentioned methods. The table divides each method into three parts: cloth, fluid and coupling. The accuracy and calculation speed of the three parts, for the application of simulating clogging effects by cloth simulation, is estimated. Since none of the methods have previously been applied to model this phenomenon, it should be noted that the table is a rough estimation of the suitability of the methods for the present application, and that the estimations for each method may change if the discretisation changes or if specialised versions of each method are used.

The Arbitrary Eulerian-Lagrangian method requires generation of a mesh and regular updating of the mesh. This results in a very time consuming computation, but a fully resolved cloth gives a strong coupling between fluid and cloth. However, the mesh in the ALE method can be highly distorted at the boundary, causing inaccuracies or the need for expensive remeshing.

Table E.1: ADVANTAGES AND DISADVANTAGES OF THE MENTIONED METHODS. NOTE THAT DIFFERENCES IN DISCRETISATION OR USE OF SPECIALISED VERSIONS OF EACH METHOD MAY CHANGE THE TABLE. TABLE ENTRIES WHERE NO ESTIMATION HAS BEEN MADE ARE MARKED WITH -. [1] Sotiropoulos and Yang (2014), [2] House and Breen (2000)

		ALE	IB	SPH-FEM	CFD-DEM
Cloth	speed	-	-	low[2]	high[2]
	accuracy	-	-	high[2]	medium[2]
Fluid	speed	low	high[1]	high	high
	accuracy	high	medium	medium	high
Coupling	speed	-	-	-	-
	accuracy	high	medium	-	medium

Since a cloth can buckle, twist and self-collide, severe distortion of cells is expected. To handle collison additional algorithms must be implemented to keep the method stable. Therefore, it is not expected to be the most suitable method for the current application, even though this approach fully resolves the cloth and therefore is expected to be physically consistent.

The Immersed Boundary method does not require remeshing since the grid is not conforming to the fluid-structure interface. Furthermore, grid generation is fast since even complex geometries can be meshed with a cartesian mesh and the boundaries can be handled with interpolation. The structered grid enables the use of very efficient flow solvers (Sotiropoulos and Yang, 2014). Therefore, the calculation speed is estimated to be high in Tab. 1. However, this method is less accurate near the boundary of the immersed body than the ALE method because of interpolation errors, and the coupling is less strong than for the ALE method due to this interpolation. Akcabay (2007) showed that this method is able to handle collision and buckling and twisting.

To fully avoid using a mesh to resolve the fluid phase, the SPH-FEM method have been investigated. This method models the fluid phase as particles and the cloth as an FEM surface. The fact that there is no need for mesh generation and remeshing makes the method computationally inexpensive and therefore interesting for the application. However, the SPH method for simulation of pump flow is less common than the CFD approach and is estimated to be less accurate. House and Breen (2000) states that modelling of the cloth as an FEM surface results in a more accurate, however more time consuming simulation than the particle approach. Therefore the calculation speed for cloth compuations in the SPH-FEM method is estimated to be low, while the accuracy is estimated to be high.

The CFD-DEM method uses a mesh for resolving the fluid phase. However, like the IB method the mesh is not conforming to the fluid structure interface, and therefore the calculation speed for the fluid fase is estimated to be high. The coupling between fluid and cloth is handled by equations for the fluid forces and the accuracy of the coupling is therefore fully dependent of a reliable formulation of the fluid forces on each particle of the cloth. Collision is handled by DEM and the characteristics of the cloth is modelled by experimentally obtained energy functions.

Physical consistent cloth properties is a high priority to ensure that the cloth simulation will correctly predict clogging effects. Therefore, overall characterisation of cloth properties must be done to include this in the model. This can be achieved by the Kawabata evaluation system (KES) (Kawabata, 1980). The results of the characterisation can be implemented in all the mentioned methods.

E.6 Conclusion

Four potential methods of modelling a cloth entering a wastewater pump have been reviewed. The simulation make high demands to the stability of the cloth model, as it must be able to handle large deformations, extensive self-collision, and twisting. Additionally, fluid-cloth interaction must be included and the physical accuracy of the simulation is a high priority.

All of the reviewed methods are potentially applicable for the simulation, since they have been used in cases with requirements that resembles the requirements to a simulation of a cloth entering a pump. However, simulations and detailed validation must be conducted before a final conclusion of the applicability of the different methods can be made. The application of the Immersed Boundary method for simulation of cloths in a washing machine, indicates that this method is also appropriate to use for modelling of a cloth entering a pump. Furthermore, SPH-FEM is an interesting method for the application, since it is a meshless method. However, CFD is commonly used and well validated for the simulation of fluid in pumps, and therefore the CFD-DEM method is chosen for future work, where the final aim is to facilitate the design process of wastewater pumps with reliable simulations of clogging effects.

E.7 Acknowledgments

This work is funded by Grundfos in cooperation with the Department of Energy Technology in Aalborg University.

References

Akcabay, D. *Physics based washing machine simulations*. PhD thesis, The University of Michigan, 2007.

Alben, S., Shelley, M., and Zhang, J. Drag reduction through self-similar bending of a flexible body. *Nature*, 420(6915):479–481, 2002.

Andric, J. *Implementation of a flexible fiber model in a general purpose CFD code*. Licentiate thesis, Chalmers University of Technology, 2012.

Attaway, S., Heinstein, M., and Swegle, J. Coupling of smooth particle hydrodynamics with the finite element method. *Nuclear Engineering and Design*, 150(2-3):199–205, 1994.

Breen, D., House, D., and Wozny, M. A particle-based model for simulating the draping behavior of woven cloth. *Textile Research Journal*, 64(11):663–685, 1994.

Bridson, R., Fedkiw, R., and Anderson, J. Robust treatment of collisions, contact and friction for cloth animation. *ACM Transactions on Graphics - Proceedings of ACM SIGGRAPH 2002*, 21(3):594–603, 2002.

Cundall and Strack. A discrete numerical model for granular assemblies. *Geotechnique*, 29:47–65, 1979.

Donea, J., Huerta, A., Ponthot, J.-P., and Rodriguez-Ferran, A., editors. *Arbitrary Lagrangian-Eulerian Methods*. John Wiley & Sons, 2004. ISBN: 0-470-84699-2.

Eberhardt, B., Weber, A., and Strasser, W. A fast, flexible, particle-system model for cloth draping. *Computer Graphics in Textiles and Apparel*, 16(5): 52–59, 1996.

Gingold, R. and Monaghan, J. Smoothed particle hydrodynamics: theory and application to non-spherical stars. *Monthly Notices of the Royal Astronomical Society*, 181:375–389, 1977.

House, D. and Breen, D. *Cloth Modeling and Animation*. AK Peters, Ltd., 2000. ISBN: 9781439863947.

Kawabata, S. *Standardization and Analysis of Hand Evaluation*. The Textile Machinery Society of Japan, 2nd edition, 1980.

Kim, Y. and Peskin, C. 3-d parachute simulation by the immersed boundary method. *Computers & Fluids*, 38(6):1080–1090, 2009.

Kloss, C., Goniva, C., Hager, A., Amberger, S., and Pirker, S. Models, algorithms and validation for opensource dem and cfd-dem. *Progress in Computational Fluid Dynamics*, 12:140–152, 2012.

Lindström, S. and Uesaka, T. Simulation of the motion of flexible fibers in viscous fluid flow. *Physics of Fluids*, 19(11):113307, 2007.

Liu, M., Liu, G., and Lam, K. Constructing smoothing functions in smoothed particle hydrodynamics with applications. *Journal of Computational and Applied Mathematics*, 155(2):263–284, 2003.

Lucy, L. A numerical approach to the testing of the fission hypothesis. *Astronomical Journal*, 82:1013–1024, 1977.

Mittal, R. and Iaccarino, G. Immersed boundary methods. *Annual Review of Fluid Mechanics*, 37:239–261, 2005.

Peskin, C. *Flow Patterns around Heart Valves: A Digital Computer Method for Solving the Equations of Motion*. PhD thesis, Albert Einstein College of Medicine, 1972.

Peskin, C. The immersed boundary method. *Acta Numerica*, 11:479–517, 2002.

Sathe, S. and Tezduyar, T. Modelling of fluid-structure interactions with the space-time finite elements: Contact problems. *Computational Mechanics*, 43 (1):51–60, 2008.

Sotiropoulos, F. and Yang, X. Immersed boundary methods for simulating fluid-structure interaction. *Progress in Aerospace Sciences*, 65(6):1–21, 2014.

Stockie, J. and Green, S. Simulating the motion of flexible pulp fibres using the immersed boundary method. *Journal of Computational Physics*, 147:147–165, 1998.

Tsuji, Kawaguchi, and Tanaka. Discrete particle simulation of 2-dimensional fluidized bed. *Powder Technology*, 77:79–87, 1993.

Vuyst, T. D., Vignjevic, R., and Campbell, J. Coupling between meshless and finite element methods. *International Journal of Impact Engineering*, 31(8): 1054–1064, 2005.

Yamamoto, S. and Matsuoka, T. A method for dynamic simulation of rigid and flexible fibers in a flow field. *The Journal of Chemical Physics*, 98(1): 644–650, 1993.

Yang, Q., Jones, V., and McCue, L. Free surface flow interactions with deformable structures using an sph-fem model. *Ocean Engineering*, 55(1):136–147, 2012.

Zhu, H., Zhou, Z., Yang, R., and Yu, A. Discrete particle simulation of particulate systems: Theoretical developments. *Chemical Engineering Science*, 62: 3378–3396, 2007.

Zhu, L. and Peskin, C. Simulation of a flapping flexible filament in a flwing soap film by the immersed boundary method. *Journal of Computational Physics*, 179(2):452–468, 2002.

Zhu, L. and Peskin, C. Interaction of two flapping filaments in a flowing soap film. *Physics of Fluids*, 15(7):1954–1960, 2003.

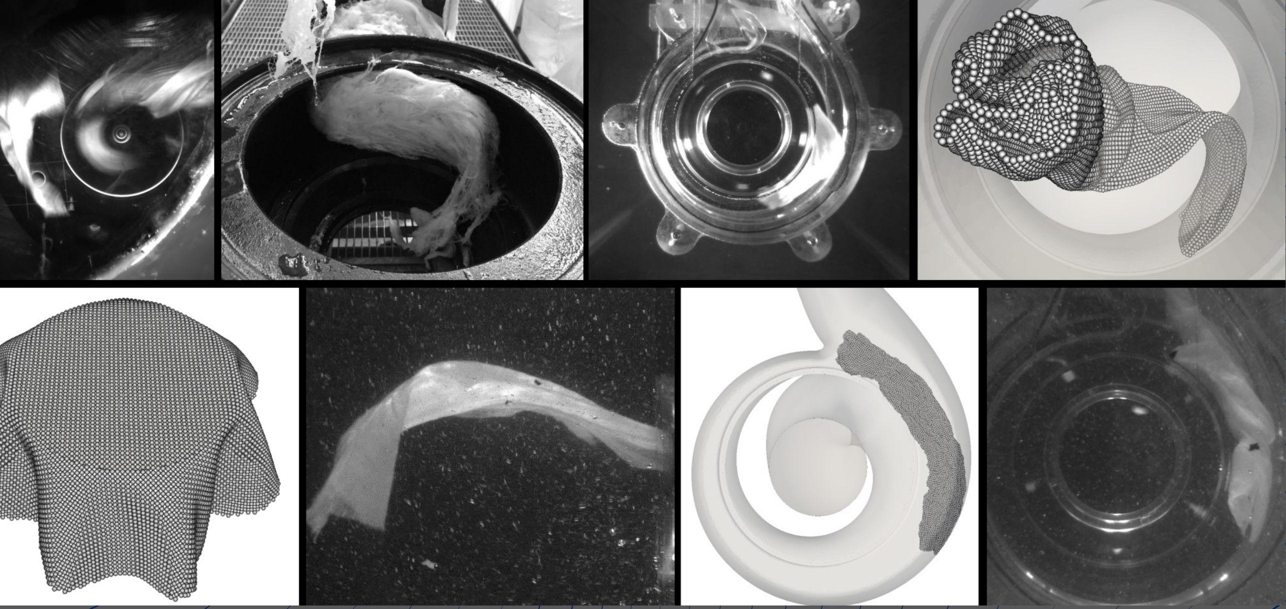

ISSN (online): 2446-1636
ISBN (online): 978-87-7210-211-5

AALBORG UNIVERSITY PRESS